Investigations of surface loads of the Earth - geometrical deformations and gravity changes

Undersøkelser av belastningsfenomener på jordens overflate - geometriske deformasjoner og endringer i tyngdefeltet

Philosophiae Doctor (PhD) Thesis

Kristian Breili

Department of mathematical sciences and technology
Norwegian University of Life Sciences

Ås 2009

Thesis number 2009:25
ISSN 1503-1667
ISBN 978-82-575-0892-0

Summary

This thesis addresses deformations and gravity changes due to surface loads like the ocean tides, hydrology and glaciers. These phenomena are discussed in light of height and gravity observations collected by GPS and gravimeters of the FG5 and LaCoste & Romberg types.

A *surface load* is here defined as a mass resting at the surface of the Earth. Body loading due to the Earth tides is consequently outside the scope of this thesis. The analysis is further restricted to address *elastic* processes only, i.e. loading effects in phase with the time history of the load. Viscoelastic processes like glacial isostatic adjustment are not discussed in depth.

A significant part of this thesis addresses ocean tide loading (OTL). The phenomenon is theoretically discussed and observational results are provided. A suite of global OTL models was compared to gravity and GPS time series at coastal stations in Norway. It was found that global models are in phase with the observations and only millimeter discrepancies exist between the magnitude of GPS observations and OTL models. When it comes to the magnitude of the gravity signals, best agreement was obtained by OTL corrections calculated from FES2004 and NAO99b. However, at several stations we observe periodic residuals of nearly 10 µgal amplitude. To reduce the weighted standard deviation of the gravity time series, an alternative method was developed for calculating OTL corrections. The method was based on locally observed ocean tides and a global OTL model for vertical displacement. Compared to global models, the alternative method reduced the RMS by up to 40 %.

The gravitational effect of hydrology was investigated in Trysil. Trysil is located inland Norway and our observations have revealed seasonal gravity changes of nearly 20 µgal. A hydrological model was developed from snow depth readings, well readings, and precipitation data. Compared to a three year long gravity time series, the model explained 64 % of the variation and reduced the amplitude of the seasonal signal strongly. More than 90 % of the gravity signal from the hydrology was formed by the snow cover within 200 m of the gravity laboratory.

The thesis also presents a high accuracy gravity network for Norway. The network includes 16 stations with gravity estimates accurate to 3-4 µgal. Compared to previously published values, this is an improvement of one order of magnitude. The gravity values will change by up to 1 µgal annually due to glacial isostatic adjustment.

Finally, attempts were made to use ground based relative gravity observations to measure the mass balance of a glacier. Preliminary results show that the method can resolve the mass balance within 10 % of the loss determined by conventional mass balance measurements. It still remains to fully validate the methodology in field.

Sammendrag

Denne avhandlingen tar for seg jordskorpedeformasjoner og endringer i jordens tyngdefelt som skyldes belastningsfenomener på jordens overflate. Belastninger kan oppstå som et resultat av for eksempel tidevann, snø, grunnvann og overflatevann etter et kraftig regnfall. Belastningsfenomenene er diskutert i lys av observasjoner samlet ved hjelp av GPS og gravimetre av FG5 og LaCoste & Romberg typen. Avhandlingen begrenser seg til belastninger som finner sted på jordens overflate og kun elastiske prosesser. Tidejordsfenomenet og viskoelastisk landhevning faller derfor utenfor avhandlingens tematiske avgrensning.

En vesentlig del av avhandlingen fokuserer på fenomenet ocean tide loading (OTL). For en samling stasjoner langs norskekysten er tidsserier av tyngde og GPS observasjoner sammenliknet med OTL signaler beregnet ut fra fritt tilgjengelige globale tidevannsmodeller. Tidsforløpet til modellene (fasen) er i godt samsvar med observasjonene. Det samme gjelder størrelsen til modellerte vertikale deformasjoner. Derimot underestimerer modellene OTL signalene i tyngdeobservasjonene på flere stasjoner. Resultatet er periodiske residualer med oppmot 10 µgal amplitude. Alt i alt fungerer modellene FES2004 og NAO99b best langs norskekysten. Likevel etterlyses bedre globale OTL modeller for tyngde i dette området.

En alternativ metode for å beregne endringer i tyngdekraften som skyldes OTL har blitt utviklet. Metoden kombinerer lokalt observert tidevann med en global OTL modell for vertikale deformasjoner. Sammenliknet med de beste globale OTL modellene, gir denne tilnærmingen opptil 40 % lavere RMS.

Hydrologisk innvirkning på tyngdemålinger ble undersøkt i Trysil. I Trysil observerer vi at tyngdekraften varierer med nesten 20 µgal gjennom et år. Dette skyldes i hovedsak varierende hydrologi. En hydrologisk modell basert på observerte snødybder, grunnvannstand og nedbørsmålinger ble utviklet. Modellen forklarer 64 % av tyngdemålingenes variasjon. Det største bidraget kommer fra snødekket innenfor 200 m fra tyngdeobservatoriet. Alene utgjør denne komponenten 90 %.

Avhandlingen presenterer også et førsteordens nettverk av tyngdestasjoner i Norge. Nettverket består av 16 stasjoner med tyngdeverdier av nøyaktighet 3 til 4 µgal. Dette er en størrelsesorden bedre enn tidligere publiserte verdier for området. Det forventes at tyngdeverdiene vil endre seg med oppimot 1 µgal årlig på grunn av landhevning.

Til sist diskuteres forsøk på å måle isbreers massebalanse ved hjelp av et bakkebasert relativgravimeter (LaCoste & Romberg). Det gjenstår fremdeles å teste metoden fullt ut i felt. Foreløpige resultater tyder likevel på at den utviklede metoden stemmer innenfor 10 % med tradisjonelle massebalansemålinger.

Acknowledgement

This thesis summarizes my work during four years as a PhD candidate at the Norwegian University of Life Sciences. For me, this has been four years of hard work and learning. Several days, I stopped believing that my thesis was ever finished. But today, it is. I can hardly believe it!

My thesis was not written alone. Hence, it is appropriate to address some words of thanks to some of my good helpers.

First of all, I am indebted to my supervisor Professor Bjørn Ragnvald Pettersen. From my first days as a PhD candidate, he has always supported my ideas and believed in my work. And maybe most important, he has given me the opportunity to do mistakes, and learn from them! During our many conversations, Bjørn Ragnvald has learned me how science is working, and he has also served me some hints about life in general. Thank you very much!

I am most grateful to my second supervisor Dr. Cecilie Rolstad. Cecilie is good at finding ways through problems and stay focused on the work to be done. Several times, she made me do one more try. Not bad, with a view to my skeptical nature.

My work relies on a large amount of data, especially observations from the absolute gravimeter FG5-226. Operation of this complex instrument was not possible without the guidance and support from Dr. Jon Glenn Gjevestad. He has always made sure that the instrument has been in mint condition and has always been ready to answer my strange questions when I have called from field late at night.

A special thank goes to Professor Emeritus Olav Mathisen. Olav welcomes every question and has the ability to raise the simplest but most suitable questions. With his enthusiasm and vital personality, he has been a real role model for me!

My friend and colleague Dagny I. Lysaker has been a most important supporter during this time. Together, we have discussed geodesy and been wailing about how ruthless life can be. However, I rather remember our discussions about Norwegian mountains. Due to Dagny, the days in office were worth living!

I would also like to thank the members of the evaluation committee of my thesis: Dr. Christian Gerlach (Norwegian University of Life Sciences/Bavarian Academy of Sciences), Dr. Norman Teferle (University of Nottingham) and Dr. Martin Vermeer (Helsinki University of Technology).

Finally, I conclude that I am most lucky because I have managed to finish this work without scaring my dearest Astrid away.

Oslo, 21 February 2010

Kristian Breili

Contents

Chapter 1

Introduction

The Earth system is dynamic. A number of geodynamical processes continuously deform the crust of the Earth and generate temporal variations in the gravity field. By combining precise observations into time series, signals from such processes are detectable by modern geodetic instruments. This thesis is based on observations and addresses dynamical processes like ocean tide loading (OTL), hydrological loading, glacial isostatic adjustment (GIA), and the mass balance of glaciers.

1.1 Background and motivation

Overview

Earth system studies are complex and involve several elements. This is illustrated by the keywords of Fig. 1.1.

Often, like in the present thesis, the analysis starts with observations. The observer should address how to achieve the best possible observations, which sources of errors generate noise in the observations, and which instruments are the most adequate to observe a particular geodynamical process. Typically, the observations are influenced by several effects simultaneously. For instance, a gravity observation is the combined sum of the gravitational force of the Earth, the force due to the centripetal acceleration of the rotating Earth, Earth tides, OTL, the attraction from the atmosphere, and so on. The more sensitive the instrument is, the more processes are significant for the observations. In this thesis, a large number of gravity and height observations are presented and analyzed. The observations are primarily collected by an absolute gravimeter of the FG5 type, a relative LaCoste & Romberg gravimeter, and GNSS (Global Navigation Satellite Systems) receivers.

The observational results constitute a valuable framework for determination and validation of models and corrections. In this study, three geophysical processes were modeled: (1) The gravitational signal of OTL was modeled by using local tide gauge observations; (2) Gravity changes due to hydrology were modeled from measurements of the ground water level, snow depth readings, and rainfall data; and (3) a mass change model was developed for calculating the mass balance of a mountain glacier from gravity and GNSS observations.

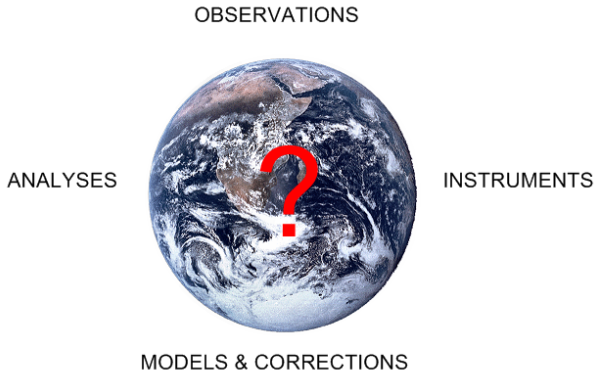

Figure 1.1: Knowledge of the Earth system is obtained by combining the elements represented by the key words *observations, instruments, models* & *corrections*, and *analyses*. (Earth photo: Courtesy NASA/JPL-Caltech)

Models and corrections are necessary to isolate particular signals in geodetic time series. For instance, gravity observations must be corrected for the effects of the Earth tides before the signal of OTL stands out. Similarly, GPS observations must be corrected for short periodic OTL signals to obtain time series free of spurious long periodic signals (Penna *et al.*, 2008). Efforts are made to build accurate global models which work at any location at any epoch. This applies to e.g. OTL models calculated from global ocean tide models. Still, often the most precise results are obtained by calculating site specific models. Later sections demonstrate this for hydrology and OTL.

After eliminating, or strongly reducing spurious signals, the isolated and characteristic signal of a geodynamical processes may be quantified by mathematical analyses. A widely used method to estimate parameters from a time series of observations is least squares adjustment. By making use of this method, the present thesis presents amplitudes and phases of OTL constituents in time series collected at Norwegian coastal stations. At first glance, such results appear as small and insignificant parts of the complex Earth system. But results like this put together may lead to significance. For instance, OTL models are vital for correcting gravity observations collected at coastal stations. In later steps, gravity observations can be used to calculate the rebound effect of GIA which must be known in order to estimate sea level changes.

And then back to start; observations. By applying improved models and increased knowledge of the Earth system, by building finer instruments, by refining

the procedures in field, and by refining the methods used to analyze data, it is possible to do more accurate observations and learn more about the Earth system. Hence, the keywords in Fig. 1.1 form the corner stones of observing the Earth system. They also form the background and motivation for the present thesis.

Objectives

This thesis focuses on the following five problems:

1. How are general surface loads of the Earth modeled?
2. Is it possible to improve OTL models for coastal gravity stations in Norway?
3. Which signals are typically found in time series of gravity and GNSS observations in Norway?
4. How are gravity changes due to varying hydrology modeled?
5. How can gravimeters be used to measure the mass balance of glaciers?

The work with these problems resulted in the six papers listed below. The papers are denoted paper A to F.

Paper A: Ocean tide loading at elevated coastal gravity stations

Paper B: The gravitational effect of ocean tide loading at high latitude coastal stations in Norway

Paper C: Short periodic GPS height variability at arctic coastal stations

Paper D: Absolute gravity values in Norway

Paper E: Effects of surface snow cover on gravimetric observations

Paper F: Ground-based gravimetry for measuring small spatial-scale mass changes on glaciers

Problem one is answered by **paper A**. In this paper, the deduction of a gravitational Green's function with a height factor was reviewed. It was aimed at providing an easy to read deduction. Based on the deduced equations, the influence of the height of the observation point on the OTL signal was discussed. In addition, the paper includes observational results demonstrating the effect of the height. Problem one is also discussed by Sect. 1.2.

The second question is addressed by both **paper B** and **paper D**. In **paper B**, gravity observations from stations along the Norwegian coast are compared to

global OTL models. This investigation is important because time series of absolute gravity observations at several Norwegian stations show periodic residuals when OTL corrections are applied. In **paper B**, it was searched for the best global OTL model for this area. In addition, an empirical OTL model based on local tide gauge observations was determined. This model was further refined in **paper D**. Section 1.3 summarizes the results and conclusions.

Problem three is addressed by all six papers. **Paper A** and **B** addresses gravity changes due to OTL along the Norwegian coast, while **paper C** follows-up by discussing the geometrical deformations. OTL is also addressed in **paper D** which provides a new first order gravity network for Norway. Gravity change rates due to GIA are discussed by **paper D**, hydrological signals are the main objective in **paper E**, and the mass loss signal in gravity observations on a mountain glacier is addressed by **paper F**. Section 1.3 to 1.6 give a summarized discussion of the signals detected in **paper A** to **F**.

The fourth problem is the subject of **paper E** presenting an empirical hydrological model for the gravity laboratory in Trysil. The need for a gravitational hydrological model in Trysil arose by analysis of a three year long gravity time series. The time series shows significant seasonal variation. The variation was not explained by varying ground water alone. Hence, the snow cover was pointed out as an important component of the hydrological model. The model and the results of **paper E** are summarized in Sect. 1.4.

Paper F and Sect. 1.6 are dedicated to the fifth problem discussing how the mass balance of a glacier can be observed by a ground based gravimeter. The motivation for this work was found in the varying results obtained by traditional mass balance measurements. Hence, there is a strong need for finding independent measuring techniques which can be used to validate other observations. Precise mass balance measurements are today most important in order to monitor climatological changes and to calculate the hydroelectric potential of glaciers.

Finally, Appendix A to D provide a supplementary discussion of gravimeters, gravity corrections, OTL calculations, and the estimation of OTL constituents by least squares adjustment.

Limitations and technical details

The studies are restricted to *elastic* processes, i.e. deformations and gravity changes in phase with the applied load. In elastic processes, the deformed Earth returns to its original shape with its original gravity field when the load is removed. Viscoelastic processes are not discussed in depth here. That means, the theory behind GIA is not discussed, but observations showing the effect of GIA are presented. The thesis is further restricted by addressing surface loads

only. Body loads like the Earth tides are not analyzed, but standard models have been applied to gravity and GNSS observations. Geographically, the study was restricted to Norway and Sweden.

A detailed discussion of gravimeters and gravity corrections are provided in Appendix A and B, respectively. GNSS positioning and processing methods are fully described in a large number of publications and textbooks, see e.g. Hoffmann-Wellenhof *et al.* (2001), Leick (2004), and Misra and Enge (2006). Hence, this thesis does not discuss technical details of GNSS positioning.

Some editorial changes have been made to the previously published or accepted papers. The changes involve the corrections of typing errors, adjustment of tables and figures to the format of the thesis, and renumbering of sections, figures, tables, and equations. No scientific contents, numerical results or conclusions are changed.

Chapter 2 to 7 are written independently of each other. Hence, the notation may change from one chapter to another, abbreviations may be explained several times, and the same equation may be written more than once. Beyond this, it is aimed at writing a thesis with an uniform layout.

1.2 Modeling surface loads

A surface load of the Earth is here defined as a mass resting at the surface of the Earth. The load may be almost anything, but it needs a certain mass to generate a detectable signal in geodetic measurements. This section describes a general method to calculate the effects of surface loads. The methodology was applied in **paper A** to calculate the gravitational effect of OTL along the Norwegian coast. In **paper E**, the methodology was used to calculate the gravitational effect of the snow cover on a three year long time series of absolute gravity measurements.

Geometrical deformations arise when the elastic crust of the Earth deforms under the weight of the load. The deformations are most prominent close to the load and attenuate with increasing distance from the load. The change in the gravity potential of the Earth (ΔV) is more complex and is usually decomposed into three components: (1) the Newtonian potential from the load (W); (2) the gravitational potential change due to the vertical displacement of the Earth's crust due to the load ($g\,U$); and (3) the gravitational potential of redistributed masses of the deformed Earth (Φ).

$$\Delta V = W - g\,U + \Phi \tag{1.1}$$

In Eq. (1.1), g is the acceleration of gravity and U is the vertical displacement of the observation point on the deformed Earth. The negative sign of the middle term reflects that an upward displacement results in a negative contribution to the

potential change in the observation point. The two last components of Eq. (1.1) are often called *elastic* components. They will be equal to zero for a rigid and inelastic earth model.

Love numbers

The effects of loads are often modeled by the Love numbers h_n, l_n, and the Shida number k_n (in the following all these numbers are called Love numbers). These numbers connect the potential of a unit load to the vertical and horizontal deformations, and the change in the Earth's potential resulting from the deformation of the Earth, respectively. Love numbers are calculated by integrating the equation of motion, the stress-strain relations, and the Poisson equation for a given Earth model (Farrell, 1972). Two widely used Earth models are e.g. the Preliminary Reference Earth Model (PREM) (Dziewonski and Anderson, 1981) and the Gutenberg-Bullen Earth model (Farrell, 1972). Following Farrell (1972), the Love numbers are defined by

$$\begin{bmatrix} U_n(r) \\ V_n(r) \\ \Phi_n(r) \end{bmatrix} = W_n(r) \begin{bmatrix} \frac{h_n(r)}{g} \\ \frac{l_n(r)}{g} \\ k_n(r) \end{bmatrix}. \tag{1.2}$$

Here W_n is the nth-degree coefficient of the potential of the unit mass, and U_n, V_n, Φ_n are harmonic coefficients for a spherical expansion of the vertical displacement, the horizontal displacement, and the potential of the Earth's distorted density field, respectively. There exist several families of Love numbers and Eq. (1.2) is a general definition. Depending on the phenomenon to be modeled, the appropriate Love numbers must be selected. For surface loads, *load* Love numbers are used. These numbers are also called *Load Deformation Coefficients* (Pagiatakis, 1990).

Green's functions

Mathematically, Green's functions are infinite sums of Love-numbers where Legendre polynomials or their derivatives form weights. They model the Earth's elastic response to the potential which surrounds a unit mass located at a spherical distance α from the observation point.

For an observation point on a spherical Earth, the Green's functions for gravity (G_a), and vertical (G_u) and horizontal (G_v) deformations are found in e.g. Farrell

(1972) and Jentzsch (1997)

$$G_a(\alpha) = \frac{g}{M} \sum_{n=0}^{\infty} \left[n + 2h'_n - (n+1)k'_n \right] P_n(\cos\alpha) \tag{1.3}$$

$$G_u(\alpha) = \frac{R}{M} \sum_{n=0}^{\infty} h'_n P_n(\cos\alpha) \tag{1.4}$$

$$G_v(\alpha) = \frac{R}{M} \sum_{n=1}^{\infty} l'_n \frac{\partial P_n(\cos\alpha)}{\partial\alpha} \tag{1.5}$$

In Eq. (1.3) to (1.5), α is the spherical distance between the load and the observation point, M is the mass of the Earth, g is gravity on the Earth's surface, $P_n(\cos\alpha)$ is the nth-degree Legendre polynomial, $\partial P_n(\cos\alpha)/\partial\alpha$ is the derivative of the nth-degree Legendre polynomial with respect to the spherical distance, and h'_n, l'_n and k'_n are nth-degree load Love numbers.

The infinite sums of load Love numbers in Eq. (1.3) to (1.5) must be truncated for practical calculations. For surface loads like the ocean tides, load Love numbers (designated with a prime) up to degree $n = 10000$ are used. Still, even truncating the sums at degree 10000 may result in significant errors at small spherical distances because the sums are ill-behaved. The appendix in **paper A** presents a more efficient computational scheme. This scheme uses analytical solutions of the asymptotic part of the Green's functions. Illustrative examples are provided in Fig. 1.2 where Eq. (1.6) is plotted as a function of maximum harmonic degree.

$$\sum_{n=0}^{N} n\, k'_n P_n(\cos\alpha) \tag{1.6}$$

In each panel, Eq. (1.6) is calculated by two schemes. The black dashed lines use Eq. (1.6) as it is written above. The red solid lines are computed by Eq. (2.31) in **paper A**. The black dashed lines show significant oscillations and converge slowly. Faster convergence is obtained by the red solid lines. The left and right panel show the convergence at $\alpha = 0.1°$ and $\alpha = 1°$, respectively. The sum converges faster for larger spherical distances.

Alternatively, the Green's functions are available through precomputed numerical values calculated by some realization of Eq. (1.3) to (1.5). Precomputed values are tabulated in e.g. Farrell (1972); Pagiatakis (1990); Jentzsch (1997) for a limited set of spherical distances. By interpolating these values, the effect of a load at an arbitrary spherical distance can be calculated.

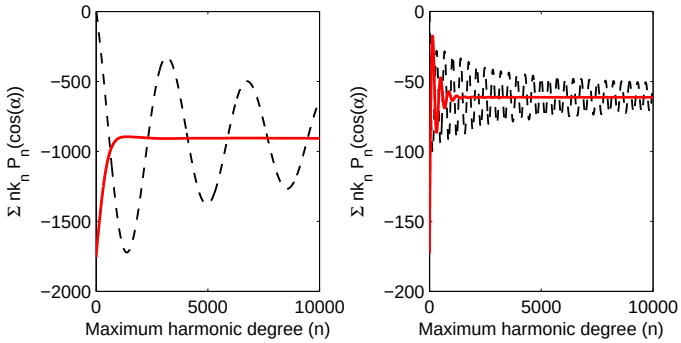

Figure 1.2: Sum of Legendre polynomials and load Love numbers as function of maximum harmonic degree. The spherical distance was set to 0.1° and 1° in the left and right panel, respectively. The black dashed lines represent Eq. (1.6) calculated by successively increasing the maximum harmonic degree up to $N = 10000$. The red solid lines were calculated by utilizing the computation scheme of Eq. (2.31) in **paper A**.

The effect of the true load

The Green's function models the Earth's response due to a unit load. The effect of the true load is found by scaling the Green's functions with a load model:

$$I(\varphi, \lambda, t) = \int G(\alpha)\, O(\varphi', \lambda', t)\, dS' \tag{1.7}$$

In Eq. (1.7) I is the load-effect at a point (φ, λ) at epoch t, $G(\alpha)$ is a proper Green's function, and O is the load model at a point φ', λ'. The integral is solved over the entire area covered by the load model.

A general load model depends on both position and time. It must provide the weight of the load at any position and at any epoch. Usually, the load model is defined on a grid and the weight of each cell can be calculated by scaling the load model by the area of the cell (dS). This transforms the integral in Eq. (1.7) into a sum over a finite number of cells (J).

$$I(\varphi, \lambda, t) = \sum_{j=1}^{J} G(\alpha_j)\, O(\varphi_j, \lambda_j, t)\, dS_j \tag{1.8}$$

The Green's function for gravity

For gravity it is common practice to publish values for only the two elastic components of Eq. (1.3). By a closed formula, the third effect due to the Newtonian

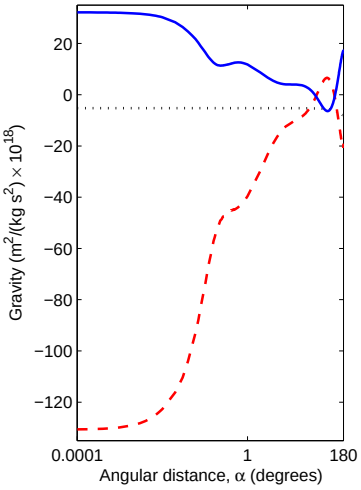

Figure 1.3: Decomposed Green's function for gravity for an observation point at the same height as the load. The black dotted line is the Newtonian attraction component, the red dashed line is the gravitational effect of the vertical displacement of the observation point, and the blue solid line is the gravitational effect of the redistribution of masses due to the deformations of the Earth. The Green's function was scaled proportionally to the distance between the observation point and the load point. The scaling coefficients were calculated by $10^{18}R \cdot \alpha$ where R is the radius of the Earth in meter and α is in radians. The Green's function was calculated from load Love numbers for the PREM Earth model tabulated in Jentzsch (1997).

attraction (G_a^N) is calculated (Farrell, 1972).

$$G_a^N(\alpha) = \frac{g}{M}\sum_{n=0}^{\infty} nP_n(\cos\alpha) = -\frac{g}{4\,M\sin(\alpha/2)} \tag{1.9}$$

The Green's function for gravity is graphically illustrated in Fig. 1.3 for an observation point at the same height as the load itself. It is seen that the Newtonian attraction component (black dotted line) for such an observation point is of minor importance. On the other hand, **paper A** shows that the attraction from the load increases significantly for an elevated observation point close to the load.

Equation (1.9) can be expanded by a height factor to include the effect of the height of the observation point above the load (Goad, 1980; Scherneck, 1991). The deduction of a Green's function with a height factor was addressed in detail by **paper A**. It was shown that the effect of an elevated observation point is significant for the Newtonian attraction component. Especially, this is true for

observation points close to the load. This is illustrated by the following example: Consider an observation point at a height 100 m above the load and at a spherical distance 0.01° from the load. At this height and distance, the Newtonian attraction is approximately 1000 times larger than at a corresponding observation point at sea level.

Table 2.3 in **paper A** shows the importance of the station height for OTL modeling. At Andøya, Bodø, Tromsø, and Ålesund, the Newtonian attraction component forms only 8 to 13 % of the total effect at sea level. At the true height of the station, the attraction component forms 23 to 58 % of the total effect.

For a given spherical distance to the load, the attraction component reaches its maximum when the horizontal distance to the load approximately equals the height above the load. The effect of the height decreases for increasing distances to the load. However, the effect decreases more slowly for a high observation point compared to a low lying observation point. For elevations up to 1000 m, the effect is negligible at distances larger than 1° to 5° (see Fig. 2.1 in **paper A**).

For most applications, the height effect is negligible for the *elastic* part of the Green's function. Hence, it is an adequate solution to interpolate between precomputed values for the elastic components, but calculate the Newtonian attraction individually for each observation point by taking the height into account.

Applications of Green's functions

The presented theory can be applied to calculate the effect of any surface load by inserting a proper load model into Eq. (1.7). Previous studies have used the described methodology to calculate the loading effect of e.g. the ocean tides (Jentzsch, 1997; Khan and Scherneck, 2003; Penna *et al.*, 2008), hydrology (Llubes *et al.*, 2004), atmospheric pressure variations (van Dam and Wahr, 1987; van Dam *et al.*, 1994; Boy *et al.*, 2002; Neumeyer *et al.*, 2004), changes in the Earth's cryosphere (Sato *et al.*, 2006b; Khan *et al.*, 2007), sea level change (Sato *et al.*, 2001), and non-tidal loading (Boy and Lyard, 2008). Still, it should be noticed that the presented methodology is most suitable for calculating the effect of loads of large spatial extension.

The Green's function methodology is well suited for calculating the effect of OTL. For OTL calculations, an ocean tide model works as load model in Eq. (1.7). In **paper A** the NAO99b ocean tide model was used to calculate the gravitational effect of OTL at four coastal stations (Andøya, Bodø, Tromsø, and Ålesund). The predicted OTL effect was compared to absolute gravity observations. Best fit to the observations was obtained by including a height factor. The fractional part of explained gravity residuals then increased by 4 % to 34 %. The largest effect was found at Andøya and Ålesund. At these two stations, the Newtonian attraction

component is strong due to the short distance to the open sea and large tidal basins.

In **paper E**, the Green's function was convolved with a snow model to calculate the gravitational effect of the snow within 200 km from the gravity laboratory in Trysil, Norway. In this study, a spherical Green's function was used, i.e. both the observation point and the load were assumed to be on a sphere. The elastic response of the Earth was calculated from a Green's function tabulated in Pagiatakis (1990) while the Newtonian attraction from the regional snow cover was calculated by Eq. (1.9).

Normally, Green's functions do not include any term modeling the *height of the load* with respect to the observation point. For some applications, this may be of vital importance for the Newtonian attraction component. In **paper E**, the load (snow) in the innermost zone around the gravimeter was located at different heights. The Newtonian attraction component for this zone was calculated separately by a refined method.

Green's functions are previously deduced by several authors, e.g. Farrell (1972); Goad (1980); Scherneck (1991). However, the derivations and descriptions often lack details necessary for an inexperienced reader to realize the formulas. **Paper A** aimed at providing an easy-to-understand description of how a Green's function may be determined. By this, **paper A** is a framework for calculating the gravitational Green's function from published load Love numbers.

1.3 Ocean tide loading signals in Norway

Time series of gravity and position estimates from the Norwegian coast were studied in **paper A, B, C**, and **D**. The results are summarized and discussed in this section.

The presented gravity time series were collected by an absolute gravimeter of the FG5 type. Absolute gravimeters suffer from wear due to the mechanical components of the instrument. As a consequence, gravity time series covering only two to three days will be presented in this section. Short time series like these are not optimum for OTL analysis. The OTL signal is composed by several diurnal, semi-diurnal and long periodic signals. A full analysis of all the main constituents requires time series covering at least 200 days, cf. Table D.1 in Appendix D. Gravity time series of this length can be collected by superconducting gravimeters (Hinderer *et al.*, 2007). Unfortunately, superconducting gravimeters are stationary instruments and no superconducting gravimeter is located along the Norwegian coast. The short time series of absolute gravity observations allow only the dominating M2 constituent to be evaluated. On the other hand, absolute gravimeters are mobile instruments which allow gravity and OTL to be observed

at several stations along the Norwegian coast.

Gravity changes due to OTL

The magnitude of the gravitational OTL signal is in general strongly correlated with the local ocean tides. Along the Norwegian coast, the ocean tides and OTL signal are strongest in the north. At high latitudes ($\geq 60°$), the gravitational M2 signal reaches an amplitude of up to 10 µgal at coastal stations (**paper A** and **B**). On the other hand, the effect of OTL is hardly detectable in Stavanger at 59° latitude (**paper D**). The modest OTL signals south of 60° arise due to an amphidrome (point where the ocean tides have zero amplitude) in the North Sea southwest of Egersund in Norway. In addition, the distance between the gravimeter and the sea, the height of the observatory above the sea, and the size of the local tidal basin are important for the magnitude of the observed OTL signal.

The gravitational effect of OTL originates from three sources: The direct Newtonian attraction from the ocean tides, the displacement of the observation point due to the load, and the redistribution of masses due to crustal deformations. The two first components dominate compared to the third component. In **paper A** and **B**, it was found that the displacement component exceeds the estimated attraction from the ocean tides, even at several coastal stations (Andøya, Bodø, Honningsvåg, and Tromsø). The result was a surprise since it contradicts Scherneck and Bos (2009), who argue that the direct gravitational attraction of the tidal water mass is more than likely dominating the loading when the station is less than 1 km from the coast. In this thesis it is found that also the elevation of the station must be considered when looking for the strongest component. This is graphically illustrated in Fig. 1.4.

When gravity time series from the Norwegian coast are corrected for Earth tides, polar motion, and atmospheric loading, a semidiurnal signal corresponding to the M2 constituent (semidiurnal tide caused by the Moon) of period 12.42 h dominates. In **paper B**, this dominating signal was used to validate a suite of six global OTL models (FES2004 (Lyard *et al.*, 2006), FES95.2 (Le Provost *et al.*, 1998), GOT002 (Ray, 1999), NAO99b (Matsumoto *et al.*, 2000), Schwiderski 1980 (Schwiderski, 1980), and TPXO.7.1 (Egbert and Erofeeva, 2002)) downloaded from the ocean loading service of H. -G. Scherneck and M. S. Bos at `http://www.oso.chalmers.se/~loading/`. It should be remarked that the names of the OTL models originate from the ocean tide model used to calculate the OTL model. The first letters of each name identify the family in which the models belong. The numbers identify the version. FES2004, GOT002, NAO99b, TPX0.7.1 and Schwiderski were all chosen because they represent the last version of each family.

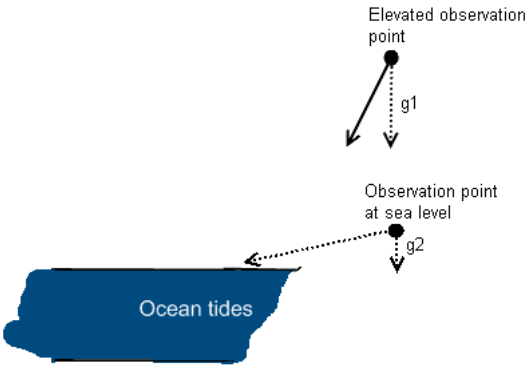

Figure 1.4: The vertical component of the gravitational force from the ocean tides depends on both the height of the observation point and the distance from the sea.

FES95.2 was included because it has improved tides in the Arctic (Scherneck and Bos, 2009).

Visual inspection of Fig. 3.3 in **paper B** indicates fair agreement between the phase of the gravity observations and the models at Tromsø, Andøya, and Bodø. At Honningsvåg, the gravity observations were delayed by approximately 10°. When it comes to the magnitude of the OTL signals, the global models underestimate the observed OTL signal at Andøya and Honningsvåg. This creates periodic residuals with an amplitude of several microgals. At Bodø and Tromsø, most global OTL models agree with the observations. All in all, the models FES2004 and NAO99b fit best to the gravity observations along the Norwegian coast.

Geometrical deformations due to OTL

Compared to the gravity changes, the geometrical deformations due to OTL along the Norwegian coast are less prominent with respect to the accuracy of present observations. Vertical deformations up to 4 cm peak to peak occur close to the coast. The horizontal deformations are smaller with a magnitude of less than one centimeter peak to peak (see Table 4.2 in **paper C**). Also the deformations due to OTL are strongest in the north of Norway. This is seen in Fig. 1.5. In this figure, the NAO99b ocean tide model was used to predict vertical deformations due to the M2 OTL constituent across Fennoscandia. The figure also shows the geographical location of some of the stations mentioned in the text.

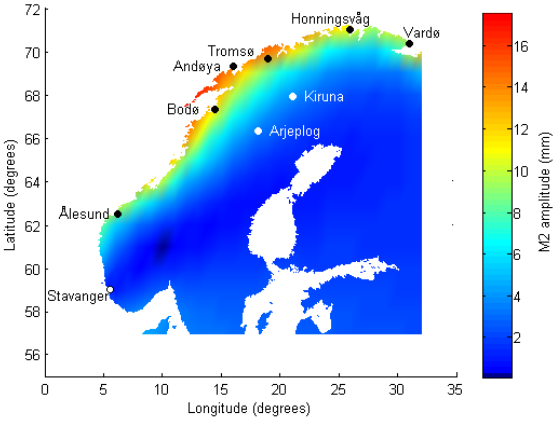

Figure 1.5: The NAO99b predicted amplitude of the vertical deformation due to the M2 OTL constituent in Fennoscandia.

In **paper C**, attempts were made to identify the main OTL constituents by relative carrier phase positioning of GPS observations. The principle was to process baselines between the inland reference station Kiruna, five coastal study stations (Andøya, Bodø, Honningsvåg, Tromsø, and Vardø), and one continental station (Arjeplog). Arjeplog was included in the analysis because this location was assumed to experience only modest height changes due to OTL. Hence, any strong diurnal and semidiurnal signal at this station is spurious and does not originate from OTL. Therefore, the GPS processing strategy was validated at Arjeplog.

First, signals originating from OTL and signals with an unknown origin were identified by periodogram analysis of the GPS height time series. Second, the amplitude and phase of the identified signals were estimated by least squares adjustment (the method is thoroughly described in Appendix D). The amplitude of the M2 OTL signal was estimated between 2 to 11 mm while the amplitude of the S2 OTL signal was approximately half of this. At all stations, the M2 and S2 OTL constituents were significant with respect to the Student t-test.

The origin of the signals was discussed by considering the phase properties, i.e. the estimated phases were compared to the same five global OTL models used in **paper B**, and also the models Andersen 2006 (AG06) (Andersen *et al.*, 2006), EOT08a (Savcenko and Bosch, 2008), CSR4.0 (Eanes and Shuler, 1999), and GOT4.7. It is important to be aware that this area lacks an independent and complete validation of global OTL models. However, the results from **paper**

B may be relevant for vertical displacement models too. **Paper B** argues that the displacement component is the most significant component of the gravitational OTL signal at several coastal stations. This indicates that the agreement between the phase of the gravity observations and the OTL models also implies fair agreement between the true vertical displacement signal and the OTL models. Unfortunately, the short length of the gravity time series in **paper B** (they cover an observing interval of 2 to 3 days) implies that for phase consideration, only the M2 OTL constituent was validated. The gravity time series provide no information on the other weaker constituents.

At Andøya, Arjeplog, Bodø, Tromsø, and Vardø, the 95 % confidence interval of the observed M2 and S2 phases included the average of the global models. With reference to the global models, the agreement indicates that the identified M2 and S2 signals are true OTL signals at these stations. At Honningsvåg the average of the models was outside the confidence intervals, i.e. the observed M2 and S2 signal were delayed by approximately 12° and 62°, respectively. The delay of the M2 signal was similar to the delay reported for gravity in **paper B**. This suggests that the identified M2 signal is a true OTL signal at Honningsvåg also. For the S2 signal, two different conclusions are possible. With reference to the global OTL models, the identified S2 signal must originate from a phenomenon different from OTL. Conversely, if we trust the observations, the phase of the global OTL models are wrongly predicted at Honningsvåg.

The inland station Arjeplog was included to validate the processing of the GPS observations. At this station, three significant peaks were pointed out in the periodogram. All these signals were weak. The strongest has an amplitude of 3.1 mm and a period corresponding to the K1 constituent and the repeat cycle of the GPS satellites (23.93 h). The existence of this signal proves the problem of estimating the K1 and K2 constituent from GPS observations. Several sources of errors have a pattern close to these periods. This could be e.g. errors in the tropospheric zenith delay estimates, errors in the tropospheric mapping function, and artifacts resulting from the semidiurnal orbital period of the GPS satellites. Because Arjeplog is an inland station, the observed K1 signal was likely to not originate from OTL. A possible origin is rather multipath or an effect due to the tropospheric zenith delay.

A strong K2 signal was also found at the coastal station Honningsvåg. OTL was not directly excluded as the origin of this signal because the station is located only 50 m from the sea. Again, the origin of an OTL signal may be proven or disproved by considering the phase and trusting global OTL models. In Honningsvåg, the phase of the strong K2 signal deviates by 51 to 76° from the model predictions. This indicates that the K2 signal is not an OTL signal. A possible

origin is multipath. This hypothesis was strengthened by the conical metallic roof at a small lighthouse located next to the GPS antenna (see Fig. 4.6 in **paper C**).

Significant spurious signals with frequencies not corresponding to OTL constituents were detected both at coastal stations and at Arjeplog. A 12.39 h signal was found at Andøya, Bodø, Arjeplog, and Vardø. Other signals were site specific, e.g. the 4.92 h signal of amplitude 5.7 mm at Andøya. The origin of these spurious signals was not confidently established.

From the analysis of Arjeplog and the coastal stations, it was concluded that GPS only to a modest extent introduces spurious signals which disturb the OTL analysis. This also indicates that the chosen reference station in Kiruna is good and does not systematically introduce any strong spurious signals. Still, the reference station in Kiruna is suspected to be the origin of the weaker spurious signals of period 12.39 h detected at some of the study stations. The 12.39 h signal was strongest at Andøya where it reached an amplitude of 4.7 mm.

OTL models from local tide gauge observations

The effects of OTL are normally predicted from global models calculated by the Green's function method presented in Sect. 1.2. To reduce the computational burden, preprocessed site specific coefficients for the main tidal constituents are often used. In Appendix C, it is discussed how site specific coefficients can be calculated from ocean tide models and a Green's function. In addition, Appendix C describes how these coefficients are used to calculate the effect of OTL.

Paper B recognized the need for improved OTL models at coastal gravity stations at high latitudes in Norway. Significant periodic signals were observed in gravity time series corrected by global OTL models. An alternative methodology for computing OTL corrections was suggested. It included only two of the three components (cf. Eq. (1.1)) generating gravity changes due to OTL. The Newtonian attraction from the ocean tides and the gravity change due to vertical displacement of the observation point were calculated, while the gravity change due to redistribution of masses as a result of the deformations was omitted.

The main argument for omitting the third component, was to avoid calculations of the Green's function and the processing of the global convolution sum of Eq. (1.8). By this, the complexity of the computations was reduced. Table 2.3 in **paper A** demonstrates that the third component is the less significant one. For the stations analyzed in **paper A**, it generates only 7 to 14 % of the total OTL signal. This corresponds to approximately one microgal for gravity changes of ten microgals.

In **paper B**, the Newtonian attraction from the local ocean tides was calculated by fitting circular sectors to the coastline. The tidal height of the sectors

was provided by a local tide gauge. A uniform tidal height was assumed, i.e. all sectors were assigned the same tidal height. The spatial extension of the model was restricted to include the ocean tides within 10 km from the gravity laboratory. **Paper B** argues that 99 % of the attraction from a disk of infinite extension (cf. a Bouguer plate) and tidal height 1.0 m is ensured by the water within 1 km from an observatory at a height 100 m above the disk. Hence, 10 km should be a sufficient extension for calculating the attraction from the local ocean tides.

The methodology was refined in **paper D** where the circular sectors were replaced by a grid. The vertical component of the Newtonian attraction vector from each cell in the grid was calculated by

$$\Delta g_N = G\frac{m_i \cdot h}{l_i^3}, \tag{1.10}$$

where G is Newton's gravitational constant, m_i is the mass of cell i, l_i is the distance between the observation point and the midpoint of the cell, and h is the height of the observation point.

A high resolution coastline from the Global Self-consistent, Hierarchical, High-resolution Shoreline Database (GSHHS) (Wessel and Smith, 1996) downloaded from `http://www.ngdc.noaa.gov/mgg/shorelines/gshhs.html` was used in both **paper B and D** to distinguish between land and sea. As an example, Fig. 1.6 shows a 250 m × 250 m grid surrounding the gravity laboratory at Ålesund. The resolution of 250 m × 250 m was chosen only for this figure. For the calculations,a resolution of 100 m × 100 m was used.

The gravitational effect of the vertical displacement was calculated in two steps. First, a global OTL model was used to predict the vertical displacement (Δh) of the observation point. The calculations followed Eq. (C.1) in Appendix C. Second, the gravitational effect (dg) was calculated by multiplying the vertical displacement with the normal free air gradient of gravity ($\partial g/\partial r$ = 0.3086 µgal mm^{-1}).

$$dg = \frac{\partial g}{\partial r} \cdot \Delta h \tag{1.11}$$

Although the model includes only two of the three OTL components, encouraging results were obtained. In **paper B** it was shown that the local model removes all periodic signals in the gravity time series. Compared to global models, also **paper D** reports closer fit to observations when the local models are used.

Figure 1.7 and 1.8 illustrates gravity time series from eight Norwegian coastal stations (Andøya, Bodø-Asylhaugen, Bodø-Bankgata, Hammerfest, Honningsvåg, Tromsø, Trondheim, and Ålesund). From these time series (and others), final absolute gravity values were calculated in **paper D**. The observations are here

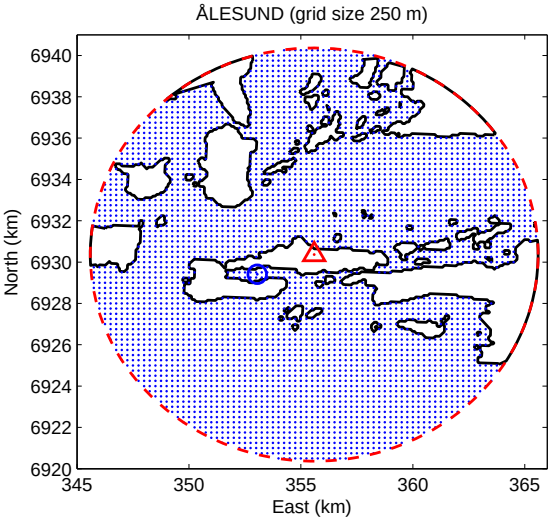

Figure 1.6: Map of the coastline at Ålesund, Norway. The red triangle and the blue circle indicate the location of the gravity laboratory and the tide gauge, respectively. The grid has a spatial resolution of 250 m × 250 m and covers a circular area with radius 10 km.

presented together with the global OTL model found to be best in **paper B**, and the local model. Additionally, the residuals between the gravity observations and the local and global model are shown. For all stations the local model fits the observations better than the global model. This is also evident in Table 1.1, listing the set scatter (weighted standard deviation) and the amplitude of the remaining M2 signal in the gravity time series corrected and not corrected for OTL. For all stations, the local model reduces the set scatter (except Bodø-Bankgata) and the amplitude most. Still, harmonic signals remain in the residuals of the local models at several stations.

It is striking that both the global and the local model at most stations underestimate the effect of OTL. For the local model, it is tempting to suspect this to be due to the OTL component omitted from the model. However, from Fig. 1.3 and Eq. (1.3) it is seen that the omitted component has an opposite effect compared to the two included components. Including the omitted component, will worsen the fit between observations and the local model.

Gravity residuals may also arise due to errors in the global model used to calculate the vertical displacement component. The amplitudes of the semidiurnal signal in the residual time series were estimated to 0.5 to 3.6 µgal (Table 1.1 column

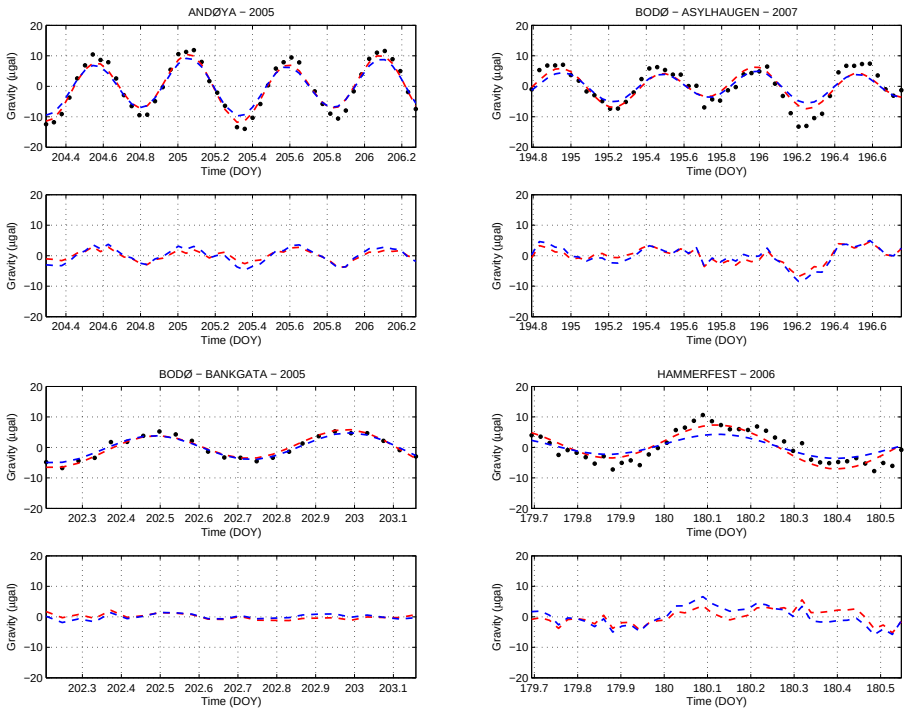

Figure 1.7: Gravity time series at Andøya, Bodø - Asylhaugen, Bodø - Bankgata, and Hammerfest. For each station, the upper panel shows the gravity observations (black filled circles) together with the local OTL model (red dashed line) and the best available global OTL model (blue dashed line). The lower panel shows the residuals between the gravity observations and the local model (red dashed line), and the global model (blue dashed line). The gravity observations were corrected for Earth tides, varying atmospheric pressure, and polar motion.

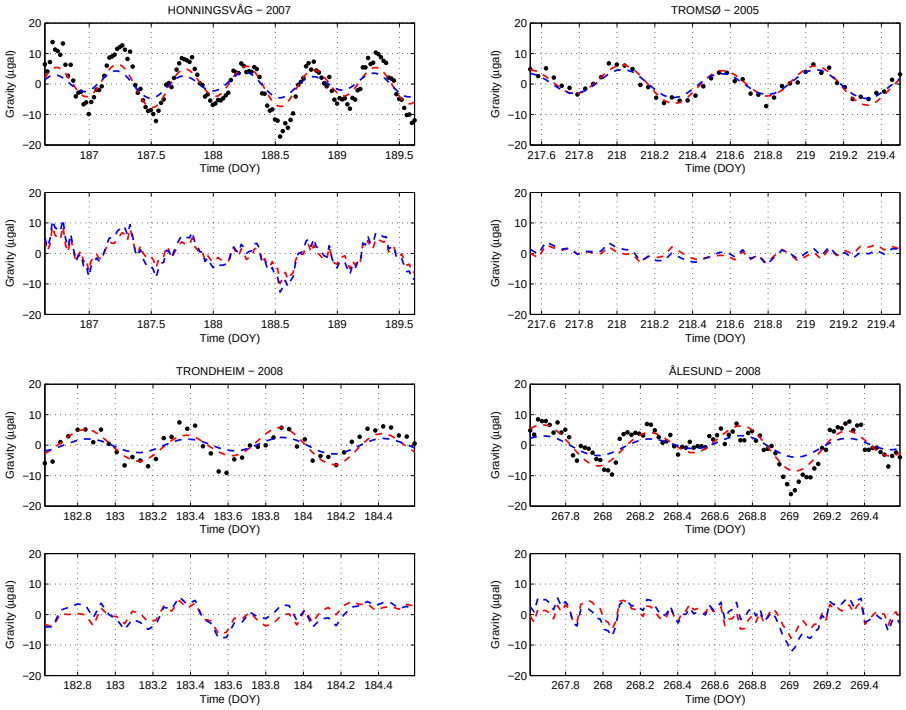

Figure 1.8: Similar to Fig. 1.7, but for the stations Honningsvåg, Tromsø, Trondheim, and Ålesund.

A_2). Divided by the free air gradient (cf. Eq. (1.11)), the gravitational semidiurnal signals correspond to geometrical vertical displacements of 2 to 12 mm. This is significantly larger than the millimeter magnitude discrepancies found between the model-predicted and the GPS observed M2 signal in **paper C**).

The most likely source of the misfit between gravity observations and the local model is errors in the coastline used to separate land from sea. This is especially relevant for the stations closest to the ocean. In Table 1.1 it is seen that the strongest semidiurnal signal is found in the residuals from Honningsvåg. This station is located only approximately 50 m from the sea. It is consequently most sensitive to both errors in the ocean tide model and in the coastline used to distinguish sea from land.

The methodology behind the local model is useful for coastal gravity observations which are strongly influenced by the Newtonian attraction from the local tides. This component is difficult to model accurately by a global model. Hence, a local model may be adequate. The main advantage of the local model is its ability to include local tide gauge observations. Local tide gauge observations are helpful because they represent the real ocean tides. This implies that the local OTL model may include effects the global models do not include, e.g. non-tidal ocean loading due to the weather and the seasonal climate cycle. The disadvantage is its dependency of a local tide gauge. The model may be refined by using an even finer coastline. Finally, the vertical displacements can be estimated from GPS observations instead of from a global OTL model (Yuan *et al.*, 2008). The result will be an OTL model for gravity independent of global ocean tide models.

1.4 The effects of hydrology on absolute gravity observations

Paper E addresses the effects of surface snow cover, ground water, and precipitation on absolute gravity observations. A three year long gravity time series from Trysil, Norway, was studied. The time series shows seasonal variations of nearly 20 µgal, i.e. high gravity values during the winter and low during the summer. The variation was related to the location of Trysil in an area experiencing strong winter conditions from November to May.

A hydrological model was developed in order to model the gravity variation in Trysil (see Fig. 6.3 to 6.7). The model consists of three components: (1) The Newtonian attraction from the snow cover within 200 m from the gravimeter is the most important component. During the winter season, the snow in Trysil may reach more than one meter and forms a significant gravitational signal. The effect reaches more than 10 µgal in the middle of the winter. (2) The regional snow model includes the attraction and the elastic response due to the snow

Table 1.1: Set scatters and semidiurnal (M2) amplitudes for gravity time series observed at eight Norwegian coastal stations. s_1 and A_1 are the set scatter and the amplitude of the gravity observations without any OTL corrections applied, s_2 and A_2 with the local OTL model applied, and s_3 and A_3 with the best available global OTL model applied. The set scatters and the amplitudes are in µgal. The last column specifies the global OTL model used to calculate column s_3 and A_3, and the vertical displacement component of the local model.

Station	**Year**	$\mathbf{s_1}$	$\mathbf{s_2}$	$\mathbf{s_3}$	$\mathbf{A_1}$	$\mathbf{A_2}$	$\mathbf{A_3}$	**Global model**
Andøya	2005	8.11	1.67	2.39	11.2	2.2	3.1	FES2004
Bodø Asylhaugen	2007	5.19	2.26	2.61	7.4	1.9	2.8	NAO99b
Bodø Bankgata	2005	3.76	0.85	0.85	4.9	0.5	0.7	NAO99b
Hammerfest	2006	5.23	2.55	3.21	6.7	1.4	3.3	NAO99b
Honningsvåg	2007	6.89	3.22	4.61	9.1	3.6	5.9	FES2004
Tromsø	2005	3.97	1.52	1.67	4.9	0.6	0.7	NAO99b
Trondheim	2008	4.47	2.59	3.19	5.8	1.2	3.6	NAO99b
Ålesund	2008	5.53	2.73	3.92	5.7	0.6	3.2	FES2004

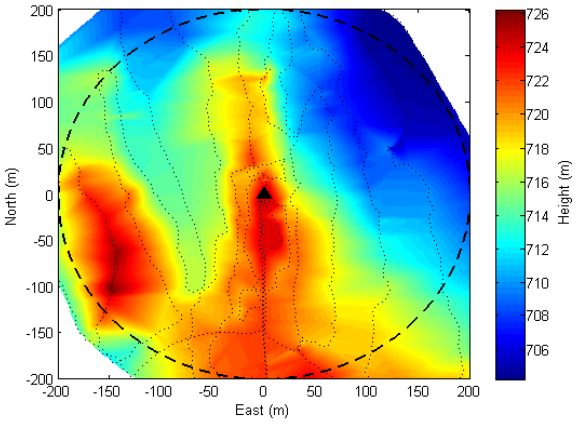

Figure 1.9: The digital terrain model (DTM) used to calculate the Newtonian attraction from the local snow cover within 200 m from the gravity laboratory in Trysil. The location of the gravity laboratory is indicated by the triangle, while the GNSS track used to generate the DTM is shown by the dotted line. The dashed line indicates the spatial extension of the local snow cover model.

between 200 m and 200 km from the observatory. The effect is about 10 % of the local effect. (3) Ground water and rainfall data forms the third component. Varying ground water level leads to gravity changes of 6 to 7 µgal while heavy rainfall generates gravity signals of more than 2 µgal. When rainfall data, snow depth readings, and well readings are combined into a hydrological model, strong correlation is found between the gravity time series and the model. The total model is graphically illustrated in Fig 6.7 of **paper E**.

It is important to remove or minimize the effect of hydrology in gravity time series when the data are used to study longer term processes such as gravity changes due to GIA (Lambert *et al.*, 2006). When all standard corrections are applied (see Appendix B), the seasonal gravity variation in Trysil is more than 10 times the annual rebound signal from GIA. Consequently, hydrology may easily mask GIA signals estimated from gravity time series. From Fig. 6.2 in **paper E**, it is seen that most of the gravity variation is seasonal. Hence, the hydrological effect is reduced by collecting gravity observations at the same time each year. On the other hand, Fig. 6.2 shows that the amplitude of the seasonal signal varies from one year to another. This means the effect of hydrology varies e.g. from one summer to another and should be eliminated by a hydrological model.

1.5 Gravity changes due to Glacial Isostatic Adjustment

In Fennoscandia (The Scandinavian Peninsula, The Kola Peninsula, Karelia, and Finland), Glacial Isostatic Adjustment (GIA) (also called postglacial rebound) generates linear trends in time series of position estimates, gravity, and sea level. GIA results from the ice sheet covering Fennoscandia in the Pleistocene Epoch ending about 10000 years ago. The ice sheet formed an enormous load deforming the lithosphere and the mantle of the Earth. When the ice sheet started to melt, the Earth started to recover from the deformations. The process is still ongoing.

The largest GIA effects exist in areas where the ice cap was at its thickest, i.e. in the Gulf of Bothnia. In this area, the ice cap may have been as thick as 2000 m (Lambeck *et al.*, 1998). The present day vertical rebound in the Gulf of Bothnia is approximately 10 mm yr^{-1}. The effect decreases away from the Gulf of Bothnia. At the coast of Norway the vertical deformations are from 0 to 4 mm yr^{-1}. The horizontal deformations due to GIA increases with the distance away from the uplift center and reaches 1-2 mm yr^{-1} at the coast of Norway (Milne *et al.*, 2001; Johansson *et al.*, 2002).

Geometrical deformations are associated with a change in the gravity field. Land uplift yields a negative gravity change because the distance between the surface of the Earth and the center of mass increases. The relation between gravity and vertical deformations due to GIA has been previously investigated

by several authors. In Wahr *et al.* (1995), the proportionality constant between gravity and vertical deformations was determined to -0.15 µgal mm^{-1} from a wide range of viscosity profiles of the Earth. Lambert *et al.* (2006) compared gravity and vertical rates observed by GPS at four Canadian sites and calculated a proportionality constant of -0.18 µgal mm^{-1}. In Scandinavia, proportionality constants between -0.17 and -0.22 µgal mm^{-1} are calculated from absolute gravity measurements and GPS observations at 13 stations (B. R. Pettersen, personal communication, 2009).

By multiplying land uplift rates by the proportionality constant, approximate gravity change rates due to GIA are obtained. This was done in **paper D**. For the 16 gravity stations across Norway, annual gravity changes between -0.2 and -1.0 µgal yr^{-1} were found. These approximate results were provided in **paper D** to transform the time tagged gravity values from one epoch to another.

Also **paper E** discusses gravity change due to GIA. The three year long gravity time series from Trysil shows a significant negative linear trend. Most likely, the trend originates from GIA. The trend was estimated to -1.90 $\pm$ 0.4 µgal yr^{-1} from three years of gravity observations.

At Hønefoss, Stavanger, Tromsø, Trysil, and Ås, time series covering 5 to 16 years exist. These time series are sufficiently long to derive *observed* annual gravity change rates due to GIA. The observations after 2000 were collected by the FG5-226 absolute gravimeter, while the observations in 1993 and 1995 were made by the National Oceanic and Atmospheric Administration and the Norwegian Mapping Authority. The original observations from 1993 and 1995 have not been available for reprocessing. Hence, the results as processed at the time were adopted from Roland (1998). The time series and the estimated long-term trends are graphically illustrated in Fig. 1.12. The numerical results are listed in Table 1.2.

The largest long-term annual gravity change rate was found at Trysil. This was expected, because it is known that Trysil is the gravity station in Norway experiencing the largest geometrical deformations due to GIA (Johansson *et al.*, 2002). The rate estimated from the long-term gravity time series compares well to the value presented in **paper D**. On the other hand, it is significantly smaller compared to the gravity change rate estimated in **paper E**. The difference indicates that the three year long time series used in **paper E** is too short for estimating the annual gravity change rate due to GIA, or that the slope changes with time, or that there was an unobserved break in the curve.

Also at Hønefoss, the estimated long-term annual gravity change rate is negative and compares well to the value presented in **paper D**. It should be remarked that omitting the observation from 1995 yields a positive trend of 2.24 $\pm$ 0.25

µgal yr^{-1}. Divided on the proportionality constant of -0.15 µgal mm^{-1}, this gravity change rate corresponds to a subsidence of approximately 15 mm yr^{-1}. The observed subsidence at the gravity laboratory contradicts the geometrical rebound at Hønefoss predicted to 4 to 5 mm yr^{-1} (Johansson *et al.*, 2002) due to GIA. It is possible that a local phenomenon plays havoc with the long term trend. Several new larger buildings are raised in the neighborhood of the gravity laboratory. This may lead to changes in the ground water level or a local subsidence due to compression of the ground in the area. When a longer gravity time series exists, the positive trend of the five latest gravity observation campaigns will be a subject for further investigation.

The time series of gravity observations at Tromsø indicates that this station is not stable. A significant shift occurs between the 2005 and 2008 campaigns. When the shift and the long term trend are included in the same linear model, the shift was estimated to -18.25 $\pm$ 4.97 µgal while the trend was estimated to 0.10 $\pm$ 0.34 µgal yr^{-1}. The slightly positive trend is not significantly different from zero. This indicates that the gravitational GIA effect is virtually absent in Tromsø. Compared to the trend presented in **paper D**, the long-term trend deviates by 0.6 µgal yr^{-1}.

Multiplied by the proportionality constant of -0.15 µmm^{-1}, the shift in the gravity time series corresponds to a height change of 122 mm. A vertical shift of this size is not found in the height time series from the TRO1 GPS station located next to the gravity laboratory (see Fig. 1.10). This indicates that the shift has not a geometrical origin, but is more likely due to a mass change.

The gravity shift corresponds to a spherical mass of radius 10 m and density 2670 kg m^{-3} located 65 m beneath the gravity laboratory (Turcotte and Schubert, 2002, Eq. 5-99). Masses of this size may have been removed during the reconstruction of the Langnestunnel located in the ground 50 to 80 m beneath the gravity laboratory (see Fig. 1.11). The reconstruction took place from May 2006 to October 2007, i.e. in the interval where the shift in the gravity time series was observed. The reconstruction involved widening of the tunnel from 8.0 to 9.5 m, and the height was enlarged from 3.5 to 4.6 m. In addition, new turnarounds were constructed (Wikipedia, 2009). We conclude that the shift in the gravity time series in Tromsø is likely related to the reconstruction of the Langnestunnel.

In Stavanger, the estimated trend indicates only modest gravity changes due to GIA. The trend is negative, but not significantly different from zero. The estimated trend from the gravity time series agrees with the trend calculated in **paper D**.

The observed trend at Ås was calculated in two separate steps. First, the effect of a reconstructed gravity laboratory was estimated by analyzing 37 gravity

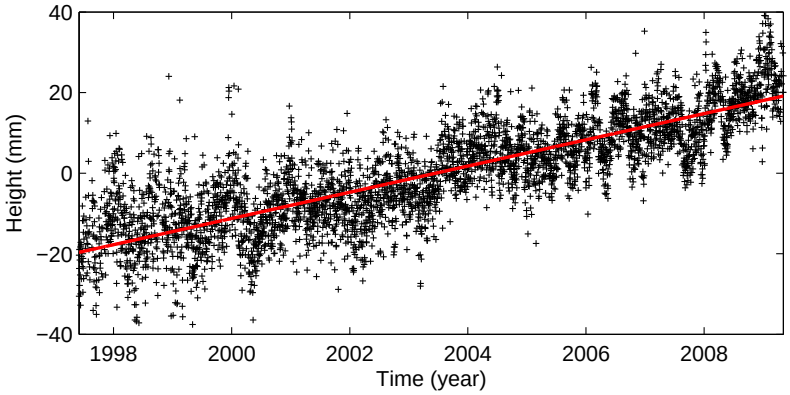

Figure 1.10: Height time series from the TRO1 GPS station located next to the gravity laboratory in Tromsø. The black markers represent daily solutions while the red line is the linear trend calculated by least squares adjustment. The trend was estimated to 3.25 mm yr^{-1}. The GPS data were provided by O. Kristiansen, 2009.

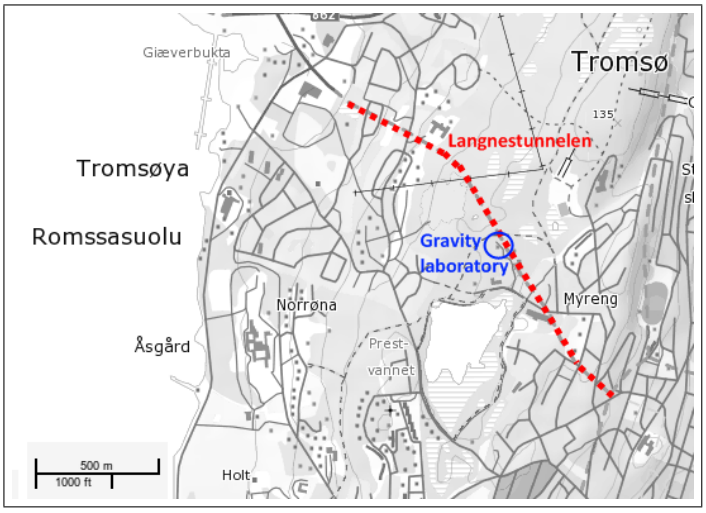

Figure 1.11: Map of the area surrounding the gravity laboratory in Tromsø. The red dashed line indicates the Langnestunnel and the blue circle indicates the gravity laboratory. The background map was downloaded from `http://kart.statkart.no/`.

campaigns covering an interval of five years. It was found that gravity shifted by -1.17 ± 0.32 µgal between January and September 2006 when the building was refurbished. In a second step, the long term trend was estimated from a subset of the gravity campaigns. From each year covered by the time series, one gravity campaign was selected. In order to reduce the effect of varying and not monitored local hydrology, only campaigns from late summer were selected. The gravity values collected prior to the rebuilding of the laboratory were corrected for the shift estimated in step one. Then, the long term trend was estimated to -0.95 ± 0.36 µgal yr^{-1}. The rate is higher than expected from GIA at Ås. Still, the rate presented in **paper D** is within one standard deviation from the observed rate.

The observed gravity change rates should be considered as preliminary results. The gravity observation program in Fennoscandia will continue in the future in order to build longer time series. From five to six years of annual measurements, secular gravity change estimates with a precision of about ±0.5 µgal yr^{-1} can be calculated (Steffen *et al.*, 2009). This precision estimate and the uncertainties listed in Table 1.2 assume a white noise model. Other noise models and the noise due to the setup of the instrument were discussed by van Camp *et al.* (2005). They found that the gravity change rate can be estimated with an uncertainty of 0.1 µgal yr^{-1} after 15 to 25 years of annual gravity measurements.

It is important to understand the ongoing GIA processes in Fennoscandia because a similar process takes place at Greenland. Due to the potential of adding around 7 m to global sea level (Pugh, 2004), the mass balance of the Greenland ice cap is regularly monitored with GPS, laser and satellite altimetry, and with satellite gravimetry. These observations must be corrected for the contribution from rebound signals in order to provide information of the glacial mass loss (Khan *et al.*, 2008).

1.6 The mass balance of a mountain glacier observed by a gravimeter

In **paper F**, ground-based gravimeters combined with GPS were discussed as a method to observe mass changes on mountain glaciers. The gravitational mass change signal on a glacier arises from accumulation and melting of snow and ice, and also ice dynamics transporting snow and ice from one area to another. In addition, the vertical gradient of the Earth's gravity field makes an influence when the surface of the glacier is lowered due to melting or ice dynamics. A gravitational mass change model was developed in **paper F**. This model shows that the last effect due to the gravity gradient of the Earth is the most dominant component when gravity change on a glacier surface is modeled.

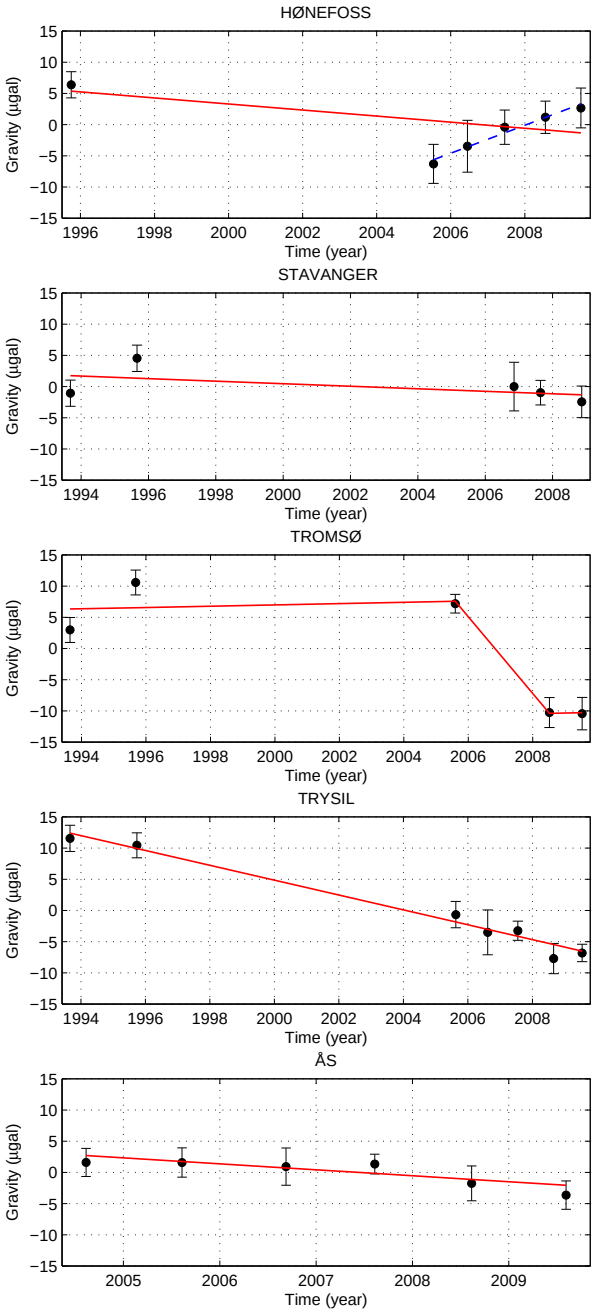

Figure 1.12: Long-term gravity changes at Hønefoss, Stavanger, Tromsø, Trysil, and Ås. The error bars indicate the set scatter of each observation campaign. Notice that the time series cover intervals of different length.

Table 1.2: Annual gravity change rates at Hønefoss, Stavanger, Tromsø, Trysil, and Ås. The observed rates are estimated from gravity time series covering 5 to 16 years. The predicted rates are adopted from **paper D**.

Station	**Interval**	**Observed rate**	**Predicted rate**
Hønefoss	1995 - 2009	-0.49 ± 0.29 µgal yr^{-1}	-0.7 µgal yr^{-1}
Stavanger	1993 - 2008	-0.20 ± 0.18 µgal yr^{-1}	-0.2 µgal yr^{-1}
Tromsø	1993 - 2009	0.10 ± 0.34 µgal yr^{-1}	-0.5 µgal yr^{-1}
Trysil	1993 - 2009	-1.19 ± 0.07 µgal yr^{-1}	-1.0 µgal yr^{-1}
Ås	2004 - 2009	-0.95 ± 0.36 µgal yr^{-1}	-0.6 µgal yr^{-1}

Experimental measurements with a LaCoste & Romberg relative gravimeter at Hardangerjøkulen were used to validate the model determined in **paper F**. By connecting the relative gravity measurements at the glacier to measurements at bedrock, absolute gravity change between two epochs was observed. Unfortunately, the observations from Hardangerjøkulen were contaminated by gross errors of unknown origin.

The fieldwork procedures were also tested at Midtre Lovénbreen at Svalbard in May 2008. The fieldwork involved relative gravity measurements between eight stations. Five of these stations were located on a glacier. Two sessions were accomplished. For each session, all points were observed twice in order to discover errors and detect blunders. The vertical gradient of gravity was measured at one of the observation points on the glacier. Analysis of the gravity measurements revealed that the gravity observations from Midtre Lovénbreen did not hold the accuracy necessary to determine mass changes on a glacier. This was due to instrumental problems.

The instrumental problems arise from a defect instrument exposed to shaking and vibrations during the transport between the observation sites. The result was unpredictable jumps in the measured gravity differences. Even though the gravity observations were useless for further analysis, the experiments at Midtre Lovénbreen resulted in practical experiences. It was demonstrated that it is possible to realize the fieldwork procedures presented in **paper F** and to operate a gravimeter on a glacier in an arctic environment.

It still remains to validate the presented theory by doing new measurements. The methodology is of relevance because traditional mass balance measurements are disturbed by significant errors (Rolstad *et al.*, 2009). Ground-based gravimetry provides an independent validation of the traditional measurements. The full potential of the methodology is employed by doing repeated measurements and

by improved instrumentation.

1.7 Conclusion and outlook

The most important results of this thesis are now summarized. Future work and subjects to follow-up are also presented.

Summary

The investigations have lead to the following conclusions:

- A complete equation for calculating the gravitational Green's function including a height factor was presented in **paper A**. The effect of the height factor was demonstrated.
- An alternative scheme for calculating the gravitational effect of OTL at coastal stations was developed in **paper B** and **D**. Compared to global models, improved fit to observations was obtained by the presented method.
- The need for improved global gravity OTL models along the Norwegian coast is recognized. The global OTL models underestimate the effect of OTL at several Norwegian coastal gravity stations (**paper B**, and **D**).
- OTL gravity corrections calculated from the NAO99b and FES2004 ocean tide models fit gravity observations along the Norwegian coast best. These two models are recommended in this area (**paper B**).
- The origin of the errors in the global gravity OTL models along the Norwegian coast is inaccurate coastlines rather than errors in the tidal models (**paper B**).
- For vertical displacements, only sub millimeter discrepancies were established between the GPS estimated and the model predicted M2 constituent. The global models FES95.2, NAO99b, and TPX0.7.1 fit best to the OTL constituents identified in the GPS height time series from the Norwegian coast (**paper C**).
- Comparisons of observations and global OTL models indicate that the phase of the predicted M2 constituent is advanced by approximately 10° in Honningsvåg with respect to the observations (**paper B** and **C**).
- A hydrological model accounting for 64 % of the gravity variation in a three year long time series of absolute gravity observations was developed. The model demonstrates that the gravitational effect of hydrology can be calculated by combining snow depth readings, well readings, snow density

measurements, and rainfall measurements. More than 90 % of the gravity signal from hydrological changes was generated by the local snow cover close to the gravimeter (**paper E**).

- Final absolute gravity values for 16 Norwegian stations were presented in **paper D**. This is the first national gravity network based on measurements from a modern absolute gravimeter. When it comes to the accuracy, it represents an improvement from 16-40 µgal (Morelli *et al.*, 1971) to 3-4 µgal, i.e. a factor of nearly 10. The gravity values serve as a framework for detailed gravity measurements, instrument calibration and validation, ground truth for gravity satellites, and reference for long-term monitoring of gravity changes in Norway.

- Gravity observations combined with height changes observed by GPS have the potential to resolve the mass balance of a mountain glacier within approximately 10 % of the loss determined by conventional mass balance measurements. The method presented in **paper F** provides independent control of traditional methods which are contaminated by systematic errors and significant uncertainty. The full potential of the presented methods requires gravity observations of accuracy better than 5 µgal. This is obtainable by modern relative gravimeters like the Scintrex CG5 or an A10 absolute gravimeter.

- Fieldwork at Midtre Lovénbreen at Svalbard demonstrated that it is possible to operate a relative gravimeter on a glacier in an arctic environment.

Suggestions to future work

- More gravity observations will be collected in Scandinavia in the future. From these observations, reliable estimates of the present day gravity change rates due to GIA can be calculated. These estimates will provide a new framework for constraining GIA models. The gravity rate field of Scandinavia observed by absolute gravimeters can be compared to gravity field rates calculated from GRACE monthly solutions.

- The collected gravity observations can be used as ground truth for validation and calibration of gravity satellites like GRACE and GOCE. Especially the time series from Trysil, covering an interval of three years, may be suitable for this purpose. By comparing this particular gravity series to GRACE data, the satellite's ability to capture regional seasonal gravity changes in Scandinavia can be investigated.

- Improved estimates of OTL displacements along the Norwegian coast may be calculated by refined and alternative GNSS methods. This involves the use of absolute receiver and antenna phase center models, improved tropospheric mapping functions recommended by the IERS (i.e. the Vienna Mapping Function 1 (Boehm *et al.*, 2006b) and the Global Mapping Function (Boehm *et al.*, 2006a)), and Precise Point Positioning (PPP) should be evaluated as an alternative to relative carrier phase positioning. Spatial filtering should be investigated as a method to remove common mode errors (Teferle *et al.*, 2009). This is especially important for PPP solutions. By processing longer time series of GNSS observations, it may be possible to detect weak OTL constituents still not validated. Also the horizontal deformations due to OTL should be considered.

- The methods of **paper F** should be tested in field with an improved instrument. The Scintrex CG5 allows gravity to be observed with a repeatability of 5 µgal (SCINTREX Limited). With this accuracy, the full potential of the methodology will be fulfilled. It should be emphasized that the fieldwork must be accomplished in a manner allowing the detection of gross errors and blunders.

- The positive trend of the five latest gravity campaigns at Hønefoss should be analyzed in depth. The location should be examined for environmental changes and changes due to human activities. This could be e.g. a change in the local ground water level, reconstruction of the building housing the laboratory, and new nearby constructions.

1.8 Publications from this PhD project

Peer reviewed journal publications

Lysaker, D. I., Breili, K., and Pettersen, B. R. (2008). The gravitational effect of ocean tide loading at high latitude coastal stations in Norway. Journal of Geodesy, vol. 82, pp 569 - 583.

Breili, K. and Rolstad, C. (2009). Ground-based gravimetry for measuring small spatial-scale mass changes on glaciers, Annals of Glaciology, vol. 50, pp 141 - 147.

Breili, K. and Pettersen, B. R. (2009). Effects of surface snow cover on gravimetric observations, Journal of Geodynamics, vol. 48, pp 16 - 22.

Breili, K. (2009). Ocean tide loading at elevated coastal gravity stations. Kart og Plan, vol. 69, pp 151 - 164.

Breili, K., Gjevestad, J. G., Lysaker, D. I., Omang, O. C. D., and Pettersen, B. R. (2009). Absolute gravity values in Norway, Accepted for publication in Norwegian Journal of Geography.

Conference poster presentations

Breili, K., Kjørsvik, N., and Pettersen, B. R. (2006). Time series analysis of GPS and absolute gravimetry in a land uplift area, Geophysical Research Abstracts, vol 8, EGU06-A-02566.

Breili, K., Lysaker, D. I., and Pettersen, B. R. (2007). Ocean tide loading models for coastal gravity observations, Geophysical Research Abstracts, vol 9, EGU2007-A-03656.

Breili, K., Kristiansen, O., and Pettersen, B. R. (2007). Seasonal gravity variation observed by an absolute gravimeter - preliminary results, Geophysical Research Abstracts, vol 9, EGU2007-A-03633.

Lysaker, D. I., Breili, K., Gjevestad, J. G., Omang, O. C., and Pettersen, B. R. (2007). Ocean tide loading along the Norwegian coast, Geophysical Research Abstracts, vol 9, EGU2007-A-03343.

Breili, K. and Rolstad, C. (2008). Ground-based gravimetry for measuring small spatial-scale mass changes on glaciers, Workshop on mass balance measurements and modelling 26 to 28 March 2008, Skei, Norway, 50A061.

Chapter 2

Paper A: Ocean tide loading at elevated coastal gravity stations

Abstract. High precision geodetic determinations have demonstrated the necessity of ocean tide loading corrections. These corrections are normally obtained by convolving a proper Green's function with an ocean tide model which predicts the tidal heights over all oceans on the Earth's surface. However, published Green's function formulas normally assume an observation point on a spherical Earth and are consequently not appropriate to predict corrections for an elevated observation point. In this paper, Green's function formulas outside a spherical Earth are deduced and used to predict the gravity changes due to ocean tide loading at elevated laboratories along the Norwegian coast. The predictions are compared to gravity observations obtained with the FG5-226 absolute gravimeter in order to illustrate the effect of the modified Green's function.

Published in Kart og Plan Vol. 69(3), 2009, pages 151-164

2.1 Introduction

The ocean tides induce time dependent loads on the Earth. The phenomenon is called ocean tide loading (OTL) and causes periodic variations in geodetic time series of position estimates, gravity, strain, and tilt. This paper reviews theoretical aspects of the subject and addresses in particular the effect of the height of coastal observation sites.

Generally, the effects of OTL are most prominent in coastal regions where the potential changes due to OTL may reach 10 % of the tidal potential. At the interior of continents, the effect is smaller, but still several percent of the tidal signal (Torge, 2001). The effects of OTL in geodetic time series have been demonstrated by several authors, e.g. Lysaker *et al.* (2008) and Vey *et al.* (2002). The first paper analyzed gravity time series from the Norwegian coast and found semidiurnal OTL-signals with amplitudes reaching 11 µgal. The latter authors observed geometric deformations due to OTL with GPS and reported vertical deformations of 10 cm peak to peak at Brest, France.

The effects of ocean tide loading are usually modeled by combining load Love numbers into Green's functions which are convolved with an ocean tide model over all oceans on the Earth's surface. Mathematically, Green's functions are infinite sums of Love-numbers where Legendre polynomials or their derivatives form weights. They model the Earth's elastic response to the potential which surrounds a unit mass located at a defined spherical distance from the observation point. The effect of the true load is found by scaling the Green's functions with the ocean tide model.

Green's functions for a spherical Earth are found in e.g. Farrell (1972) and Jentzsch (1997). Both authors sketch briefly how this function is put together, but they do not discuss the situation when the observation point is elevated above sea level. However, gravity stations are seldom situated at sea-level and proper OTL-modeling should take height into account, cf. Goad (1980); Scherneck (1991); Bos *et al.* (2002); Lysaker *et al.* (2008). In the following sections we address the Green's function for gravity and present a detailed review of the deduction of a Green's function formula with a height factor. We use the Green's function to predict the gravity effect of OTL and illustrate the importance of taking height into account when the observation point is close to the load, i.e. compare predictions with coastal gravity observations.

2.2 A Green's function for gravity outside a spherical Earth

The change in the gravity potential due to OTL can be decomposed into three components.

$$\Delta V = W - g\,U + \Phi \tag{2.1}$$

In Eq. (2.1), W is the gravitational potential induced by the ocean tides, $g\,U$ is the change due to vertical displacement of the observation point on the deformed Earth, and Φ is the change due to redistribution of masses of the deformed Earth. The negative sign of the middle term reflects that an upward displacement results in a negative contribution to the potential at the observation point.

The gravity change due to OTL can be modeled by a Green's function which captures all these three components. For an observation point on a spherical Earth, the Green's function for gravity is found in e.g. Farrell (1972) (page 782) and Jentzsch (1997) (page 152)

$$G(\alpha) = \frac{g}{M} \sum_{n=0}^{\infty} [n + 2h'_n - (n+1)k'_n]\, P_n(\cos\alpha), \tag{2.2}$$

where M is the mass of the Earth, h'_n, k'_n are load Love numbers, and $P_n(\cos\alpha)$ is the nth-degree Legendre polynomial.

The Green's function in Eq. (2.2) depends only on the spherical distance α and does not include any height term. A Green's function for gravity with a height factor is deduced here. Each component of the gravity OTL-effect is treated separately and finally combined into one formula for the total gravity effect.

The attraction from the ocean tides

The gravitational potential W surrounding a point mass dm is described by a scalar function

$$W = \frac{G \cdot dm}{d}, \tag{2.3}$$

where d is the distance between the point mass and the point of observation. The distance d can be expanded into spherical harmonics by the well known formula (see for instance Hofmann-Wellenhof and Moritz (2005), Eq. 1-104.)

$$\frac{1}{d} = \sum_{n=0}^{\infty} \frac{|\mathbf{r}'|^n}{|\mathbf{r}|^{n+1}} P_n(\cos\alpha), \tag{2.4}$$

where $\mathbf{r}$ and $\mathbf{r}'$ are Earth centered radius vectors to the point of observation and the mass, respectively. By letting $\mathbf{r}$ be the vector to the observation point, convergence of the sum in Eq. (2.4) is ensured for $|\mathbf{r}| \geq |\mathbf{r}'|$, i.e. an observation point located on or exterior to a sphere with radius $|\mathbf{r}'|$. Substitution of Eq. (2.4) into Eq. (2.3) expands the gravitational potential into spherical harmonics. We assume a unit load located on a sphere with radius R and write $dm = 1$, $|\mathbf{r}'| = R$ and $G = g\,R^2/M$.

$$W = \frac{g}{M} \sum_{n=0}^{\infty} \frac{R^{n+2}}{|\mathbf{r}|^{n+1}} P_n(\cos\alpha) \tag{2.5}$$

The change in gravitational acceleration is found by differentiating Eq. (2.5) along the radius $|\mathbf{r}|$ through the point of observation.

$$\frac{\partial W}{\partial r} = -\frac{g}{M}\sum_{n=0}^{\infty}(n+1)\left(\frac{R}{|\mathbf{r}|}\right)^{n+2} P_n(\cos\alpha) \tag{2.6}$$

The height of the observation point is defined by setting $|\mathbf{r}| = R + H$. Let also $f^n = (R/(R+H))^n$.

$$\frac{\partial W}{\partial r} = -\frac{g}{M}\cdot\left[\frac{R}{R+H}\right]^2\sum_{n=0}^{\infty}(n+1)\, f^n\, P_n(\cos\alpha) \tag{2.7}$$

When $H \ll R$ (e.g. $H = 1000$ m), we put safely $(R/(R+H))^2 = 1$.

$$\frac{\partial W}{\partial r} = -\frac{g}{M}\sum_{n=0}^{\infty}(n+1)\, f^n\, P_n(\cos\alpha) \tag{2.8}$$

On the sphere, the height factor f^n equals unity, and Eq. (2.8) and the first term in Eq. (2.2) converge to the same function even though the functions seem to be different. This is shown in Appendix 2 (of this chapter).

The influence on gravity of vertical displacement of the observation point

The vertical displacement causes the observation point to move through the Earth's gravitational field and the potential change is found by multiplying the deformation by the potential's vertical gradient, i.e. the gravitational force. Change in gravitational acceleration is found in a similar manner, i.e. the vertical displacement is multiplied by the vertical gradient of gravity.

$$\Delta g = \frac{\partial g}{\partial r}\cdot U \tag{2.9}$$

Here, $\partial g/\partial r$ is the gradient of gravity and U the displacement. Density anomalies in the ground close to the observation point are capable of making local vertical free-air gravity gradients deviate significantly from the standard free-air gradient. The standard gradient should be used here, because the density anomalies experience the same displacement as the observation point. A general formula for the standard free-air gradient is found by differentiating Newton's law of gravitation:

$$\frac{\partial g}{\partial r} = \frac{\partial}{\partial r}\left\{\frac{G\,M}{R^2}\right\} = -2\frac{g}{R} \tag{2.10}$$

The definition of the Love-numbers in Farrell (1972) connects the deformation's nth-degree coefficient to the load potential's nth-degree coefficient. The total

deformation is given by

$$\begin{aligned} U &= \sum_{n=0}^{\infty} U_n \, P_n(\cos\alpha) \\ &= \sum_{n=0}^{\infty} \frac{h'_n}{g} W_n(r) \, P_n(\cos\alpha) \end{aligned} \tag{2.11}$$

It is reasonable to assume that the displacement at an elevated observation point equals the displacement on the sphere and so $W_n = G/R$ is entered into Eq. (2.11).

$$U = \frac{R}{M} \sum_{n=0}^{\infty} h'_n \, P_n(\cos\alpha) \tag{2.12}$$

Substitution of Eq. (2.10) and Eq. (2.12) into Eq. (2.9) gives the gravity change due to vertical displacement of the observation point

$$\begin{aligned} \Delta g &= -2\frac{g}{R} \cdot \frac{R}{M} \sum_{n=0}^{\infty} h'_n \, P_n(\cos\alpha) \\ &= -\frac{g}{M} \sum_{n=0}^{\infty} 2h'_n \, P_n(\cos\alpha) \end{aligned} \tag{2.13}$$

The influence on the Earth's gravity field of crustal deformations

Following Farrell (1972), the nth-degree coefficient of the influence on the Earth's gravity potential of crustal deformations is expressed by

$$\Phi_n(r) = k'_n(r) W_n(r) \tag{2.14}$$

The total influence is found by adding up coefficients multiplied by Legendre polynomials:

$$\Phi = \sum_{n=0}^{\infty} \Phi_n(r) \, P_n(\cos\alpha) = \sum_{n=0}^{\infty} k'_n(r) \, W_n(r) \, P_n(\cos\alpha) \tag{2.15}$$

In Eq. (2.14) and (2.15), $W_n(r) = G \cdot R^n/|\mathbf{r}|^{n+1}$ is the nth-degree coefficient of the Legendre polynomials in Eq. (2.5) and $k'_n(r)$ are load Love numbers of degree n. Then, assuming load Love numbers independent of $\mathbf{r}$,

$$\Phi = G \sum_{n=0}^{\infty} k'_n \frac{R^n}{|\mathbf{r}|^{n+1}} \, P_n(\cos\alpha). \tag{2.16}$$

Differentiating along $\mathbf{r}$ and putting $G = g\,R^2/M$ yields:

$$\frac{\partial \Phi}{\partial r} = -\frac{g}{M} \sum_{n=0}^{\infty} (n+1) k'_n \left(\frac{R}{|\mathbf{r}|}\right)^{n+2} \, P_n(\cos\alpha) \tag{2.17}$$

Setting $|\mathbf{r}| = R + H$, and $(R/(R+H))^2 = 1$:

$$\frac{\partial \Phi}{\partial r} = -\frac{g}{M} \cdot \sum_{n=0}^{\infty} (n+1)\, k'_n\, f^n\, P_n(\cos\alpha) \tag{2.18}$$

The total Green's function

The total change in gravity acceleration due to OTL is found by combining Eq. (2.8), (2.13), and (2.18) into one Green's function

$$G(\alpha, H) = \frac{g}{M} \sum_{n=0}^{\infty} [-((n+1) + (n+1)k'_n)\, f^n + 2h'_n]\, P_n(\cos\alpha), \tag{2.19}$$

where $f^n = (R/(R+H))^n$. In the deduction of Eq. (2.19), H was the height of the observation point above the sphere. For practical applications, H represents the height above sea level. Compared to Eq. (2.2), two terms in Eq. (2.19) are multiplied by a height dependent factor f^n. Thus, the formula is also valid for elevated observation points. Note the sign convention used in Eq. (2.2) and Eq. (2.19). To obtain a positive gravity change in the downward direction (as recorded by a gravimeter), the sign must be reversed.

The Green's function in Eq. (2.19) involves summation of load Love numbers and Legendre polynomials up to infinite degrees. For practical calculations, truncation is necessary. Problems arise because the sum is not well behaved. The problem is solved by factoring out analytical expressions for the asymptotic terms. The remaining sums are well behaved and can be truncated at e.g. $n = 10000$. This more efficient computational scheme is deduced in Appendix 1 (of this chapter).

2.3 The effect of an elevated observation point

Green's functions for the attraction component are graphically illustrated in Fig. 2.1 (left). The figure shows the attraction from a unit point mass located at spherical distances between 0.001° and 180° from the observation point. Four cases are considered, i.e. observation points at 1000 m (green solid line), 100 m (red dashed line), 10 m (blue dash-dotted line), and at sea level (black dotted line). The functions are scaled by the attraction at an observation point at sea level. This implies that the scaled Green's function for attraction at sea level is always unity in the left panel of Fig. 2.1.

For elevated observation points, the height effect is considerable for observation points close to the load, e.g. the attraction from a unit load located at a spherical distance of 0.001° from an observation point at height 1000 m is ∼1000 times larger than a corresponding observation point at sea level. The height effect diminishes for increasing distances. For the examples in the present analysis, the

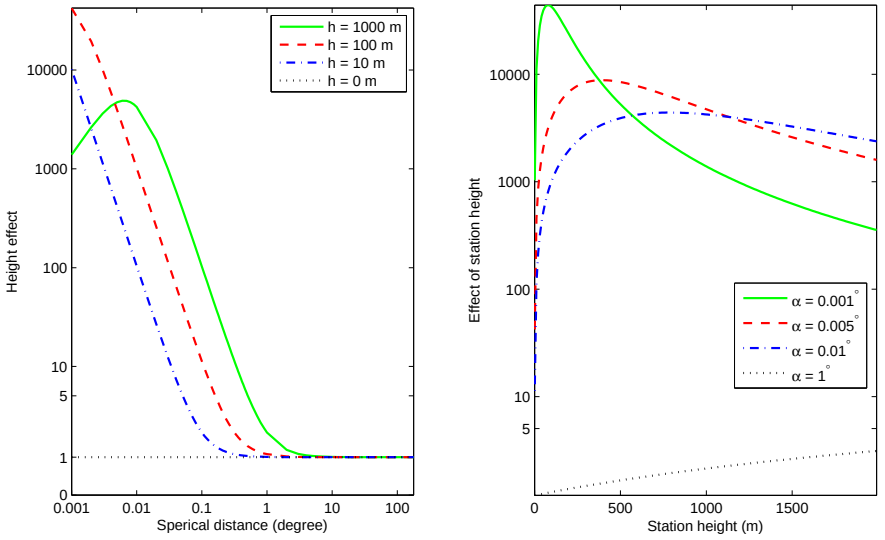

Figure 2.1: Left panel: The Green's function for attraction from the ocean tides. Four examples are considered, i.e. an observation point at $h = 1000$ m (green solid line), $h = 100$ m (red dashed line), $h = 10$ m (blue dash-dotted line), and at sea level (black dotted line). The Green's functions are scaled by the attraction at sea level. Right panel: The height effect as function of the height of the observation point. The unit load was located at four different spherical distances, i.e. at 0.001° (green solid line), 0.005° (red dashed line), 0.01° (blue dash-dotted line), and 1° (black dotted line).

effect is close to zero for spherical distances larger than 1° to 5°. The decay rate depends on the height of the observation point. In general, the height effect decays more slowly as height increases.

Figure 2.1 (right) shows that the height effect reaches a maximum when the distance to the load is approximately equal to the station height. For spherical distances of 0.001° (∼100 m), 0.005° (∼500 m), and 0.01° (∼1100 m), the largest effect is found for station heights of 80 m, 400 m, and 800 m, respectively. For larger distances to the load, the height effect grows steadily with increasing height.

Green's functions for the gravity change due to crustal deformations are graphically illustrated in the left panel of Fig. 2.2. The same four examples are considered and the functions are scaled by the corresponding effect at sea level. The pattern found in Fig. 2.2 is different from that of the attraction component. Firstly, the height effect has a smaller maximum than the attraction component.

Secondly, the load effect declines with increasing height, e.g. for an observation point at a height of 100 m and at spherical distance 0.001° from the load, the effect of this OTL component is ∼75 % of the effect at sea level. A slight increase of the load effect occurs for spherical distances between 0.1 and 0.5°. The increase is small, reaching only 5 % for the examples considered here. In the right panel of Fig. 2.2 the height effect is calculated for loads at four spherical distances and for observation points at heights between 0 and 2000 m. For the spherical distances 0.001° and 0.01°, the height effect grows with increasing height, i.e. the gravity change due to crustal deformations is reduced with increasing height. The opposite is found for a load located at a spherical distance of 0.1° from the observation point. At spherical distances of 1° or more, the load effect is independent of the height of the observation point.

For most applications, the height factor of the elastic part (vertical displacement and crustal deformations) of the Green's function is negligible. Nevertheless, the height factor for the attraction component is included in most software packages computing OTL corrections, e.g. the OTL service at `http://www.oso.chalmers.se/~loading/` (Scherneck and Bos (2009)), the SPOTL package (Agnew, 2005) and the g-software provided by Micro-g Solutions Inc.

2.4 Comparison with gravity observations

To analyze the actual effect of a height factor, the formulas in Appendix 1 (of this chapter) were used to calculate Green's functions which were convolved with an ocean tide model. Usually, the ocean is divided into a grid and the ocean tide model defines the tidal height for each grid point. This transforms the convolution integral into a sum over a finite number of ocean cells:

$$I(\varphi, \lambda, H, t) = \rho_w \sum_{i=1}^{N} G(\alpha_i, H)\, O(\varphi_i', \lambda_i', t)\, dS_i \tag{2.20}$$

In Eq. (2.20), I is the OTL-effect at a point (φ, λ, H) at epoch t, ρ_w is the density of sea-water, $G(\alpha_i, H)$ is the Green's function for a spherical distance α_i and an observation point at height H, O is the ocean tide model which gives the tidal height at a point φ', λ' at epoch t, and dS_i is the area of ocean cell i. Equation (2.20) is in accordance with Francis and Mazzega (1990).

The NAO99b ocean tide model (Matsumoto *et al.*, 2000) was downloaded from `http://www.miz.nao.ac.jp/staffs/nao99/index_EN.html` and the eleven tidal constituents M2, S2, N2, K2, K1, O1, P1, Q1, MM, Mf, and Ssa (see Chap. 4.3 in Lambeck (1988) for a brief description of the tidal constituents) were included in the calculations of the ocean tides. The NAO99b model is available on a 0.5°×0.5° grid. For OTL-modeling, refinement of the ocean tide model is quite important

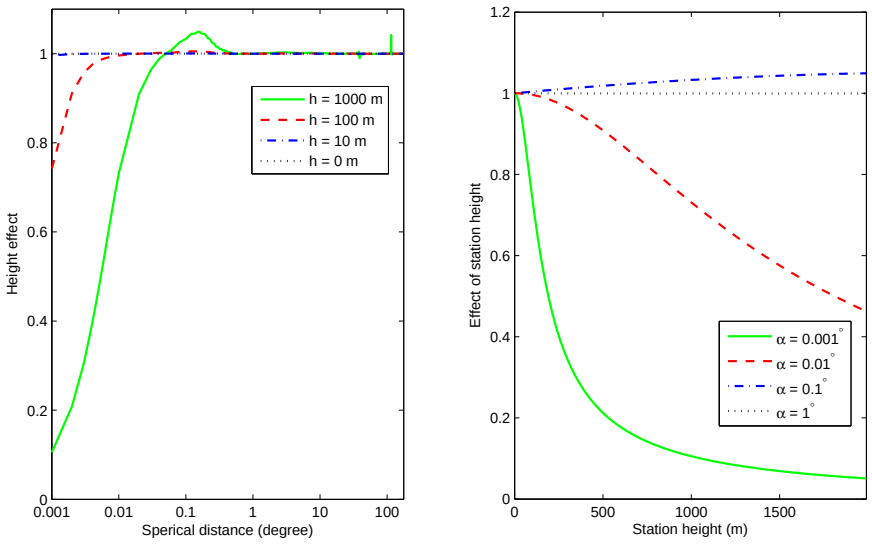

Figure 2.2: Left panel: The Green's function for the gravity change due to crustal deformations. Four examples are considered, i.e. an observation point at $h = 1000$ m (green solid line), $h = 100$ m (red dashed line), $h = 10$ m (blue dash-dotted line), and at sea level (black dotted line). The Green's functions are scaled by the load effect at sea level. The spike found close to a spherical distance of 100° is an artifact due to the scaling. Right panel: The height effect as function of the height of the observation point. The unit load was located at four different spherical distances, i.e. at 0.001° (green solid line), 0.01° (red dashed line), 0.1° (blue dash-dotted line), and 1° (black dotted line).

in coastal regions close to the observation point because a significant part of a coastal ocean cell is likely to cover land areas. In this analysis, the ocean tide model was refined onto a $0.05° \times 0.05°$ grid within 1° from the observation point and onto a $0.002° \times 0.002°$ grid within 0.1° from the observation point. A high resolution coastline from the Global Self-consistent, Hierarchical, High-resolution Shoreline Database (GSHHS) (Wessel and Smith, 1996) was downloaded from `http://www.ngdc.noaa.gov/mgg/shorelines/gshhs.html` and used to distinguish between land and sea. Green's functions were calculated by using load Love numbers for the Preliminary Reference Earth Model (PREM) (Dziewonski and Anderson, 1981) up to a maximum degree of 10000. These numbers were determined by spline interpolation of the tabulated values in Jentzsch (1997).

Modeled gravity changes due to OTL were compared to gravity observa-

Table 2.1: Coordinates and orthometric heights of the gravity stations.

Station	**Latitude**	**Longitude**	**Height**	**Distance to the sea**
Andøya	69.2780° N	16.0087° E	370 m	1.3 km
Bodø	67.2875° N	14.4340° E	68 m	2.0 km
Tromsø	69.6628° N	18.9397° E	102 m	1.1 km
Ålesund	62.4762° N	6.1985° E	140 m	0.2 km

tions collected at Andøya, Bodø, Tromsø, and Ålesund by the FG5-226 absolute gravimeter. In order to isolate the OTL-effect, the gravity observations were corrected for Earth tides, polar motion, and atmospheric loading with the g-software (Micro-g Solutions Inc.). The Earth tides were calculated from a tide generating potential from Tamura (1987) and Love numbers of the Wahr-Dehant-Defraign model (Dehant *et al.*, 1999). Additionally, the mean of the time series was subtracted because only relative gravity changes are of relevance in this analysis. A detailed description of the instrument is found in Niebauer *et al.* (1995) and processing and observational procedures are described in Lysaker *et al.* (2008). The coordinates of the stations are found in Table 2.1 and the geographical locations are illustrated in Fig. 2.3. The station heights and distances to the sea are also found in Table 2.1. All stations are located within 2 km from the Norwegian coast and are considered to be elevated stations.

Figure 2.5 shows observations and two predicted time series of the gravity effects due to OTL for stations in Fig. 2.3. For each station, two Green's functions were generated, one for sea level (red dashed line), and one for the actual height of the observation point (blue solid line).

Andøya

The gravity laboratory at Andøya is located at a height of 370 m on an island facing the Norwegian Sea. The distance to the coast is 1.3 km. Within 30 to 50 km from the gravity laboratory there are no large islands or winding fiords. The need for proper treatment of the station height is clearly illustrated by the two predicted OTL models. They differ by about 5 µgal at OTL maximum. The RMS reduction (Table 2.2) is 52 % for the OTL model designed for sea level and 87 % for the OTL model which includes the height factor. Also, this OTL model removes all periodic variations in the gravity time series. Hence, a remarkably good fit is obtained between the observations and the OTL model when the height factor is included.

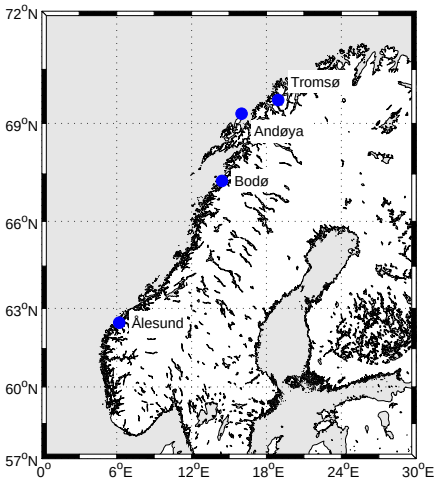

Figure 2.3: The gravity stations used to analyze the effect of a Green's function with a height factor.

Bodø

Bodø is located 2.0 km from the ocean on a small hill, 68 m above sea level. Bodø is the lowest station in this study and is located farthest from the coast. The NAO99b model was used without any modifications in Bodø. The second panel (from above) of Fig. 2.5 shows that there are no significant deviations between the two OTL models. Approximately the same RMS reduction is obtained by both models, i.e. 49 % for the model with the height factor and 44 % for the model for sea level. Except for a low minimum on day 196, both models fit the observations well. The origin of the outlying observations is at present not known. In summary, the height factor is of minor importance in Bodø.

Tromsø

The gravity laboratory in Tromsø is located on an island, 102 m above sea level and 1.1 km from the coast. The island is located in the middle of a fiord. This implies relatively small tidal basins close to the laboratory and a limited attraction component from the local ocean tides. Consequently, the OTL signal is expected to be weaker in Tromsø than at stations facing the open sea. This is seen in the third panel (from above) of Fig 2.5. Deviations of 2 to 3 µgal are found between the two OTL models in Tromsø. The model tailored to the station's height fits

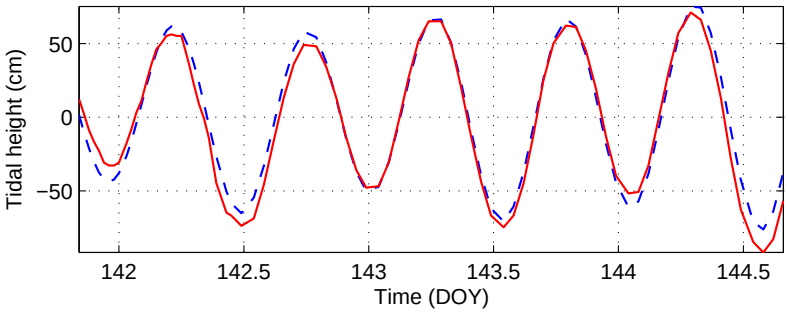

Figure 2.4: Comparison of predicted tidal heights from NAO99b (blue dashed line) and tides observed with the tide gauge in Ålesund (red solid line). The NAO99b predicted tidal heights are computed from tidal constituents at 5.75° E 62.25° N.

the observations best. It reduces the gravity time series RMS by 58 % compared to 53 % for the OTL model at sea level.

Ålesund

Ålesund is located on a peninsula at the mouth of Storfjorden in Norway. The peninsula is surrounded by several islands and fiords making the figure of the local coastline complex. The gravity laboratory is located at a horizontal distance of 200 m from the ocean and 140 m above sea level.

Before convolving the NAO99b ocean tide model with the Green's functions, the ocean tide model was modified in the area close to Ålesund. This was necessary because the ocean tides within 10 km from the observation point are not included in the original model. Lysaker *et al.* (2008) showed that it is of vital importance to include the local ocean tides for proper calculation of the attraction component. Thus, a new grid point was added at 6.25° E 62.25° N. The ocean tides at the new grid point was found by adopting the NAO99b tidal constituents for the grid point at 5.75° E 62.25° N. Tidal heights computed from these coefficients were compared to tide gauge observations in Ålesund, see Fig. 2.4. For the epochs coincident with the FG5 observations, the overall fit is good. The standard deviation is 8.8 cm and the maximum deviation is 20 cm. Ocean tides of corresponding heights create gravitational attraction of 0.5 µgal and 1.2 µgal, respectively. Thus, the expansion of the NAO99b ocean tide model is considered to be a sufficiently accurate representation of the ocean tides within 5 to 10 km from the observation point.

The lower panel of Fig. 2.5 shows significant deviation between gravity ob-

Table 2.2: RMS of the gravity time series with and without OTL corrections. Two OTL models were computed. One based on a Green's function with a height factor (Model 1), and one based on a Green's function at sea level (Model 2).

Station	**No OTL-corrections**	**Model 1**	**Model 2**
Andøya	8.0 µgal	1.1 µgal	3.8 µgal
Bodø	5.1 µgal	2.6 µgal	2.8 µgal
Tromsø	3.8 µgal	1.6 µgal	1.8 µgal
Ålesund	7.8 µgal	3.9 µgal	6.2 µgal

servations and the OTL model calculated from the Green's function at sea level. Better fit to the observations was obtained by using the Green's function with a height factor. The same pattern is reflected by the RMS values listed in Table 2.2. The OTL model which includes the height factor reduces the RMS by 50 % while the OTL model at sea level reduces the RMS by 21 %. We notice that some of the observations in the gravity series in Ålesund deviate significantly from both OTL models. The origin of this variation is at present unknown.

2.5 Discussion

The percentage contribution from each OTL component was calculated for the OTL models at sea level and at the height of the stations. The ratios were estimated by summing up the amplitudes from each tidal constituent. Then the sum was divided by the total sum of all amplitudes:

$$\text{Contribution from component } j = \frac{\sum_{i=1}^{11} A_j^i}{\sum_{i=1}^{11}\sum_{j=1}^{3} A_j^i} \cdot 100\% \qquad (2.21)$$

In Eq. (2.21) the OTL component (attraction, displacement, and the gravitational effect of crustal deformations, cf. Eq. (2.1)) is assigned by the index j, and A_j^i is OTL constituent i of component j. Equation (2.21) does not take into account phase relationships between the constituents and the components. Thus, the estimated ratios should be considered as approximate estimates of each component's contribution to the total OTL signal.

The results are shown in Table 2.3. It is evident that proper height treatment is crucial for modeling the attraction component of coastal stations. At station height, the percentage contribution from the attraction component makes a significant part of the total OTL signal at all stations. The situation is different at sea level where the attraction component is the weakest of the three components.

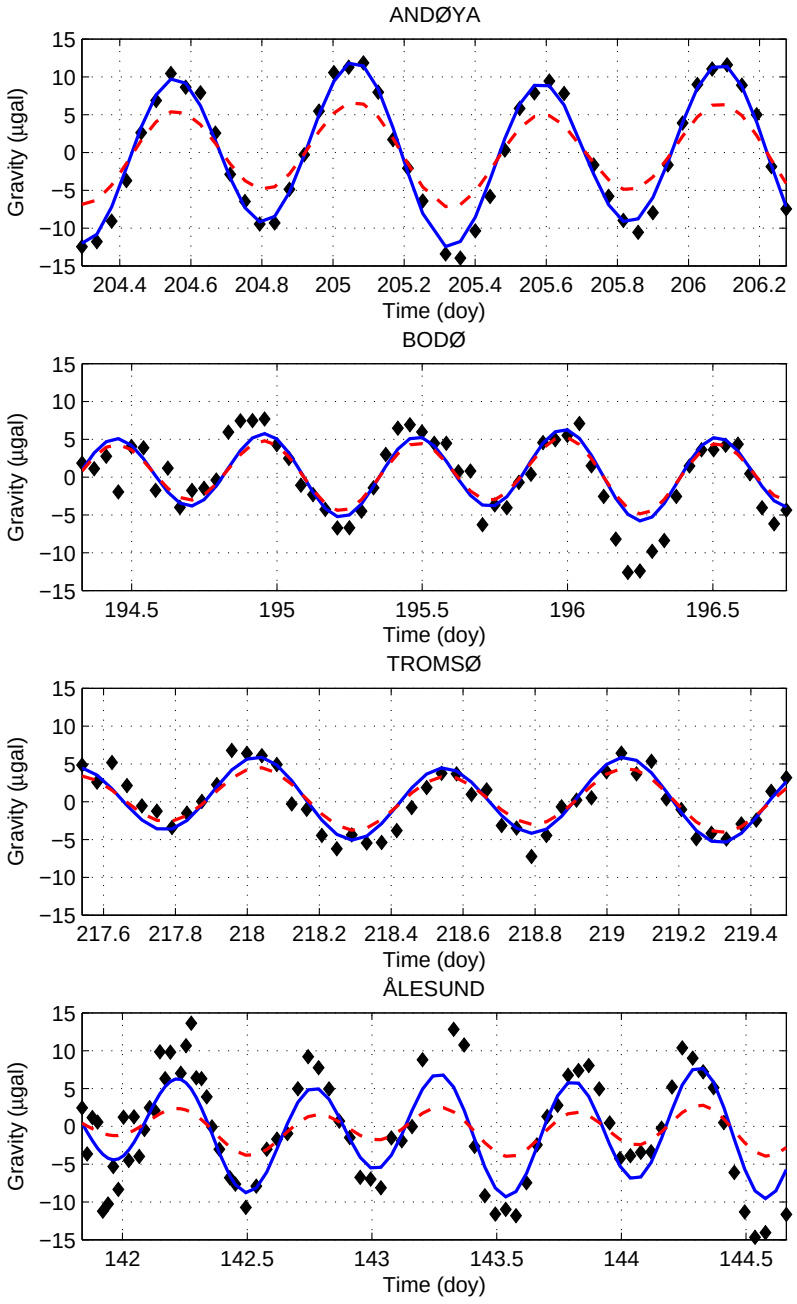

Figure 2.5: Time series of observed gravity residuals with no OTL corrections are shown as diamonds for Andøya, Bodø, Tromsø and Ålesund, Norway. Modeled OTL effects are shown as blue lines (with height factor) and red dashed lines (without any height factor). The importance of proper height modeling for an elevated observation point close to the sea is evident.

Table 2.3: The percentage contribution from each OTL effect at station height and sea level.

Station	Height	Attraction	Displacement	Crustal deformations
Andøya	370 m	42.3%	46.6%	11.1%
	sea level	11.8%	71.2%	17.0%
Bodø	68 m	22.7%	63.2%	14.0%
	sea level	12.1%	71.9%	18.0%
Tromsø	102 m	30.4%	56.3%	13.2%
	sea level	13.0%	70.4%	16.5%
Ålesund	140 m	58.4%	34.9%	6.7%
	sea level	8.0%	77.2%	14.8%

The height factor influences the attraction from the local tides most strongly, and it is therefore most important to correctly model the attraction from the local tides surrounding an elevated gravity laboratory.

The effect of the height factor is largest in Ålesund and at Andøya. This can be explained as the effect of relatively large local tidal basins and the relationship between the station height and distance to the ocean. The effect is especially prominent in Ålesund, where the distance to the ocean is approximately the same as the laboratory's height above sea level. This corresponds to the relationship found in the right panel of Fig. 2.1. The effect of a Green's function tailored the station's height is not so prominent at Tromsø and Bodø. In Tromsø this can be explained by small local tidal basins and in Bodø by the modest height of the station.

2.6 Conclusion

A Green's function for gravity with a height factor was deduced. The station's height affects the OTL signal through two components, i.e. the attraction component and the gravity change due to crustal deformations. The largest effect is found for the first component and for most applications the effect is negligible for the latter component.

Graphical representations of the Green's function show that it is important to include the height factor when the spherical distance between the observation point and the load is small. For the attraction component, it was found that the effect of the station height is largest when the distance to the ocean is approximately equal to the station's height. For distances larger than about 1° to 5° the height effects are much smaller and need not be taken into account for proper

modeling of gravity changes due to OTL.

The deduced Green's function was used to predict gravity changes due to OTL and the predictions were compared to gravity observations at Andøya, Bodø, Tromsø, and Ålesund. The Green's function with the height factor improves the OTL model. This was illustrated by using the predictions to correct the gravity observations for OTL. The RMS was significantly reduced when the Green's functions with the height factor were used. The examples clearly illustrated the need for a height factor for elevated gravity laboratories close to the ocean.

Acknowledgements

I am indebted to Olav Mathisen, Dagny I. Lysaker, and Bjørn R. Pettersen for useful and interesting discussions. Gravity observations at Andøya were made by Ove C. D. Omang.

Appendix 1: Expansions of the Green's function for practical calculations

The Newtonian attraction

The attraction term in Eq. (2.8) is:

$$\frac{\partial W}{\partial r} = -\frac{g}{M}\sum_{n=0}^{\infty}(n+1)f^n\,P_n(\cos\alpha) \tag{2.22}$$

Manipulation of the sum yields:

$$\begin{aligned}\frac{\partial W}{\partial r} &= -\frac{g}{M}\cdot\frac{\partial}{\partial f}\left\{\sum_{n=0}^{\infty}f^{n+1}P_n(\cos\alpha)\right\}\\ &= -\frac{g}{M}\cdot\frac{\partial}{\partial f}\left\{f\sum_{n=0}^{\infty}f^n\,P_n(\cos\alpha)\right\}\end{aligned} \tag{2.23}$$

From Eq. (1-103) in Hofmann-Wellenhof and Moritz (2005) an analytical expression for the term inside the brackets in Eq. (2.23) is adopted.

$$\begin{aligned}\sum_{n=0}^{\infty}\mu^n P_n(u) &= \frac{1}{\sqrt{1-2\mu\,u+\mu^2}}\\ \Rightarrow f\sum_{n=0}^{\infty}f^n P_n(\cos\alpha) &= \frac{f}{\sqrt{1-2f\cos\alpha+f^2}}\end{aligned} \tag{2.24}$$

A final analytical expression for the attraction term is obtained by differentiating Eq. (2.24) with respect to f, and by setting $f = R/(R+H)$ and $r = R+H$.

$$\frac{\partial W}{\partial r} = -\frac{g\,r^2}{M}\left[\frac{r-R\cos\alpha}{(r^2-2r\,R\cos\alpha+R^2)^{3/2}}\right] \tag{2.25}$$

The vertical displacement

The gravitational effect of vertical displacement is from Eq. (2.13):

$$\delta g = -\frac{g}{M}\sum_{n=0}^{\infty} 2h'_n P_n(\cos\alpha) \tag{2.26}$$

Manipulation of the sum yields two sums:

$$\begin{aligned}\delta g &= -\frac{2g}{M}\sum_{n=0}^{\infty}(h'_\infty - h'_\infty + h'_n)P_n(\cos\alpha)\\ &= -\frac{g}{M}\left[2h'_\infty\sum_{n=0}^{\infty}P_n(\cos\alpha) + 2\sum_{n=0}^{\infty}(h'_n - h'_\infty)P_n(\cos\alpha)\right]\end{aligned} \tag{2.27}$$

An analytical function for the first sum is found in Farrell (1972):

$$\sum_{n=0}^{\infty}P_n(\cos\alpha) = \frac{1}{2\sin(\alpha/2)} \tag{2.28}$$

The second sum is well behaved and may be truncated for e.g. degree $n = 10000$.

$$\delta g = -\frac{g}{M}\left[\frac{h'_\infty}{\sin(\alpha/2)} + 2\sum_{n=0}^{\infty}(h'_n - h'_\infty)P_n(\cos\alpha)\right] \tag{2.29}$$

The change in Earth's potential

The sum in Eq. (2.18) is separated into two sums.

$$\begin{aligned}\frac{\partial\Phi}{\partial r} &= -\frac{g}{M}\sum_{n=0}^{\infty}(n+1)k'_n f^n P_n(\cos\alpha)\\ &= -\frac{g}{M}\left[\sum_{n=0}^{\infty}n\,k'_n f^n P_n(\cos\alpha) + \sum_{n=0}^{\infty}k'_n f^n P_n(\cos\alpha)\right]\end{aligned} \tag{2.30}$$

Both sums in Eq. (2.30) are manipulated into well behaved sums. First sum of Eq. (2.30):

$$\begin{aligned}\sum_{n=0}^{\infty}n\,k'_n f^n P_n(\cos\alpha) &= \sum_{n=0}^{\infty}\left[k'_\infty - k'_\infty + n\,k'_n\right]f^n P_n(\cos\alpha)\\ &= k'_\infty\sum_{n=0}^{\infty}f^n\,P_n(\cos\alpha) + \sum_{n=0}^{\infty}(n\,k'_n - k'_\infty)f^n\,P_n(\cos\alpha)\\ &= \frac{k'_\infty}{\sqrt{1-2f\cos\alpha+f^2}} - k'_\infty + \sum_{n=1}^{\infty}(n\,k'_n - k'_\infty)f^n\,P_n(\cos\alpha)\end{aligned} \tag{2.31}$$

Second sum of Eq. (2.30) is first manipulated by changing the limits of summation. Because $k'_0 = 0$ the summation is set to start at $n = 1$:

$$\sum_{n=0}^{\infty}k'_n\,f^n\,P_n(\cos\alpha) = \sum_{n=1}^{\infty}k'_n f^n P_n(\cos\alpha) \tag{2.32}$$

Then the sum in Eq. (2.32) is split into two sums in a similar manner as the first sum of Eq. (2.30):

$$= \sum_{n=1}^{\infty} \frac{1}{n} \left[k'_\infty - k'_\infty + n\, k'_n\, f^n\right] P_n(\cos\alpha)$$

$$= k'_\infty \sum_{n=1}^{\infty} \frac{1}{n} P_n(\cos\alpha) + \sum_{n=1}^{\infty} \frac{1}{n}(n\, k'_n\, f^n - k'_\infty) P_n(\cos\alpha) \tag{2.33}$$

Khan (2005) gives an analytical expression for the sum in the first term of Eq. (2.33):

$$\sum_{n=1}^{\infty} \frac{1}{n} P_n(\cos\alpha) = -\log\left[\sin(\frac{\alpha}{2}) + \sin^2(\frac{\alpha}{2})\right] \tag{2.34}$$

Equation (2.34) inserted into Eq. (2.33):

$$\sum_{n=0}^{\infty} k'_n\, f^n\, P_n(\cos\alpha) =$$

$$-k'_\infty \log\left[\sin(\alpha/2) + \sin^2(\alpha/2)\right] + \sum_{n=1}^{\infty} \frac{1}{n}(n\, k'_n\, f^n - k'_\infty) P_n(\cos\alpha) \tag{2.35}$$

Substitution of the expressions in Eq. (2.31) and (2.35) into Eq. (2.30) gives the final expression for the change in Earth's potential. The sum is well behaved because the asymptotic part of the sum is factorized out. The sum can be truncated for e.g. $n = 10000$.

$$\frac{\partial \Phi}{\partial r} = \frac{g\, k'_\infty}{M} \left(1 + \log\left[\sin(\alpha/2) + \sin^2(\alpha/2)\right] - \frac{1}{\sqrt{1 - 2f\cos\alpha + f^2}}\right)$$

$$-\frac{g}{M} \sum_{n=1}^{\infty} \left[(n\, k'_n - k'_\infty) f^n + \frac{1}{n}(n\, k'_n\, f^n - k'_\infty)\right] P_n(\cos\alpha) \tag{2.36}$$

Appendix 2: Convergence of the attraction term

On the sphere, Eq. (2.8) converges to the same function as the first term of Eq. (2.2). This is demonstrated here by finding the function of convergence for the two terms. To do this, two identities from Appendix 1 in Farrell (1972) are useful:

$$\sum_{n=0}^{\infty} n\, P_n(\cos\alpha) = -\frac{1}{4\sin(\alpha/2)} \tag{2.37}$$

$$\sum_{n=0}^{\infty} P_n(\cos\alpha) = \frac{1}{2\sin(\alpha/2)} \tag{2.38}$$

The first term of Eq. (2.2) is identical to Eq. (2.37) multiplied with g/M.

On the sphere, $f^n = 1$ and Eq. (2.8) can be written

$$\begin{aligned} & -\frac{g}{M}\sum_{n=0}^{\infty}(n+1)P_n(\cos\alpha) \\ &= -\frac{g}{M}\left[\sum_{n=0}^{\infty} n\,P_n(\cos\alpha) + \sum_{n=0}^{\infty} P_n(\cos\alpha)\right] \end{aligned} \tag{2.39}$$

Equation (2.37) and (2.38) inserted into Eq. (2.39) results to:

$$\begin{aligned} & -\frac{g}{M}\left[-\frac{1}{4\sin(\alpha/2)} + \frac{1}{2\sin(\alpha/2)}\right] \\ &= -\frac{g}{M}\cdot\frac{1}{4\sin(\alpha/2)} \end{aligned} \tag{2.40}$$

Thus, Eq. (2.8) agrees with the first term of Eq. (2.2) on the sphere.

Chapter 3

Paper B: The gravitational effect of ocean tide loading at high latitude coastal stations in Norway

Abstract. Gravity measurements close to the ocean are strongly affected by OTL. The gravitational OTL effect consists of three parts, i.e. a change in gravity caused by direct attraction from the variable water-masses, by displacement of the observing point due to the load, and by redistribution of masses due to crustal deformation. We compare the OTL gravitational effect of several global models to observed time series of gravity to identify the best model for four arctic observation sites. We also investigate if the global models are sufficient for correcting gravity observations. The NAO99b model fits the observations best at three stations. At two stations (Tromsø and Bodø) the global models explain the variability in the observations well. At the other two (Honningsvåg and Andøya), a significant periodic signal remains after the OTL correction has been applied. We separate two of the gravitational effects, the direct attraction and the change in gravity due to displacement, to study the local effects. Simple geometric models of the water load and independent measurements from local tide-gauges are used to calculate these effects. This leads to improved correspondence with the OTL signal, hence demonstrating the importance of careful modeling of local effects for correction of gravity observations in coastal stations.

Published in Journal of Geodesy Vol. 82(9), 2008, pages 569-583

Coauthored by D.I. Lysaker and B.R. Pettersen

3.1 Introduction

The Earth is deformed by gravitational forces from celestial bodies. These deformations are periodic and known as body tides. Gravitational forces also affect the oceans, resulting in ocean tides. The load of the water masses causes additional deformations of the Earth's crust and is called ocean tide loading (OTL). OTL causes vertical displacement, horizontal displacement, a change in the potential (and in its gradient, i.e. the gravity), tilt and strain. This study addresses the gravitational change, which has three components, namely gravitational change caused by the direct Newtonian attraction from the water masses, by the displacement due to the load, and by the redistribution of masses due to crustal deformation. The OTL effects are usually modeled by convolving appropriate Green's functions and an ocean tide model. Global ocean tide models are known to have reduced accuracy close to the coast, especially along complex coastlines, at high latitudes and in shallow waters. Thus, global models of the OTL effect have reduced accuracy in such regions.

A variety of studies have modeled one or several tidal effects (Francis and Melchior, 1996; Baker and Bos, 2003; Urschl *et al.*, 2005). Ocean tide models have been validated, often indirectly by looking at the OTL effect (Bos *et al.*, 2002; Timofeev *et al.*, 2006) and models of the OTL effects have been compared directly with observations, using the displacement components and/or the gravitational component (Neumeyer *et al.*, 2005). The displacement components of the OTL effect have been studied from gravity measurements (Jentzsch *et al.*, 2000) or GPS displacement measurements (Khan and Scherneck, 2003; Melachroinos *et al.*, 2007). All these studies compare the models with a long time series of observations (49 days to several years), hence frequency analysis is possible.

Gravimeter recordings include the tidal gravitational attraction from celestial bodies, in addition to the gravity effects induced by various geophysical and geodynamical sources on regional and global scales, (e.g. Neumeyer *et al.*, 2005). Absolute gravity observed by a FG5 instrument (Micro-g Solutions Inc.) must be corrected for all tidal effects in order to obtain the correct gravity value. At many Norwegian coastal stations, significant periodic residuals were detected when tidal corrections (see Sect. 3.2) were applied.

The body tides and the OTL effects are difficult to distinguish, because their temporal variation is similar and they are derived from the same astronomical ephemerides (i.e., the positions of the celestial bodies). However, their spatial characteristics may be very different. The body tide is mostly dependent on the global rheology and varies smoothly over the Earth's surface. The OTL effects are more irregular due to local properties such as the local elasticity of the lithosphere, the complexity of the coastline, and variations in the ocean tide

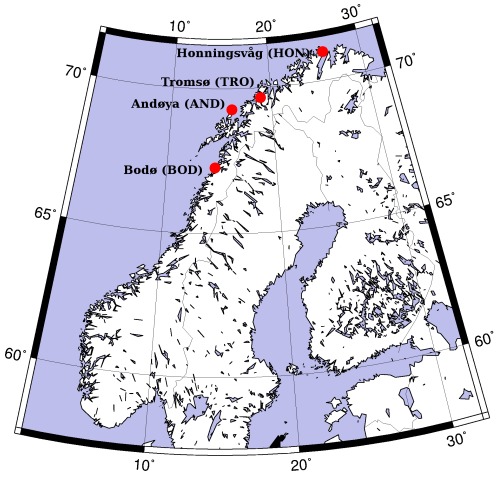

Figure 3.1: Location of gravity and tide-gauge stations used in this study.

amplitudes (Farrell, 1972). If the Earth's response to the tidal body force can be modeled sufficiently accurately, the load tide may be separated from the body tide by simply subtracting the modeled body tide from the observed tide. Several studies show that the body tidal parameters agree very well with observations (Baker *et al.*, 1996; Wang, 1997; Bos *et al.*, 2002; Baker and Bos, 2003). In this study, the body tide is thus considered as a known quantity. It is removed from our observations and the signal left is interpreted as the observed OTL effect.

We have analyzed FG5-observations from four arctic (latitude $> 67°$ N) stations along the Norwegian coast (Fig. 3.1). The gravity residuals are compared to different global models of the OTL gravity effect in order to identify the best model for the area. The time series are dominated by a semidiurnal signal, for which we estimate the amplitude and phase. Global models reproduce the phase acceptably, but are systematically smaller in amplitude. Discrepancies are reduced by considering local effects. Simple geometric models of the water load and independent measurements from local tide-gauges are used to calculate these effects. This shows the importance of careful modeling of the local effects when correcting gravity observations at coastal stations. We also discuss how the different OTL models affect the mean absolute gravity value and its standard deviation.

3.2 Data

Ocean tide models

Global ocean tide models predict the variations in time and space of the ocean surface height due to the tide-generating potential. Most models provide amplitudes and phases for 11 main constituents, i.e. semidiurnal waves M2, S2, N2, K2, diurnal waves K1, O1, P1, Q1, and long-period waves Mf, Mm, and Ssa. More than 95 % of the tidal signal is explained by these 11 constituents (Lambeck, 1988).

In this study, six global ocean tide models were used, i.e. the Schwiderski model (Schwiderski, 1980), FES95.2 (Le Provost *et al.*, 1998), FES2004 (Letellier, 2004), NAO99b (Matsumoto *et al.*, 2006), GOT00.2 (Ray, 1999), and the latest TOPEX/Poseidon model TPXO.7 (Egbert and Erofeeva, 2002). The Schwiderski model is included in this study because it was the first model accurate enough for geophysical studies, and it is still used as default for OTL corrections in the software from the FG5 instrument provider. The other models were selected since they are the latest models from different ocean tide research groups and partly because they claim improvement in arctic regions and/or in shallow waters.

Ocean tide loading models

Models of the OTL effect used in this paper, in the following called OTL models, were obtained from the OTL-provider web-site of H.-G. Scherneck and M. S. Bos (`http://www.oso.chalmers.se/~loading/`). The OTL-provider computes amplitudes and phases (relative to Greenwich) for the 11 main tidal constituents by convolving an ocean tide model with an appropriate Green's function according to Farrell (1972). The OTL-provider uses Green's functions computed for a Gutenberg-Bullen Earth model with a continental crust. Initially, the Green's functions are developed on the Earth's surface. However, when the gravitational effect is considered, the height must be taken into account. It can be shown that this may be handled by multiplying the nth degree of the Green's function with a factor $[R/(R+h)]^n$, where R is the mean radius of the Earth and h is the height (Scherneck, 1991). It originates in the deduction of the Green's function for the gravitational effect outside a sphere instead of on the sphere. Note that this height factor has an impact on all three gravitational components, with largest impact on the direct attraction. This factor is used in the OTL-provider, (H.-G. Scherneck, personal communication, 2007). Amplitudes and phases for the *gravitational effect* are provided, hence the height above sea level of the observing site is important. Orthometric heights for the observation sites were obtained with a hand-held GPS receiver and controlled by detailed maps (scale 1:5000 with contour intervals of 5 m). Two of the stations (Tromsø and Bodø) have leveled height

values.

The coastline resolution is about 600 m and is taken from the Generic Mapping Tools (GMT) package (Wessel and Smith, 1996). No correction for the motion of the Earth's center of mass due to the ocean tides was applied, since this study does not deal with satellite observations.

The OTL models were downloaded from the OTL-provider on 29 January 2007. They were provided in BLQ-format and had to be transformed into a time series. The method used here is in accordance with the International Earth Rotation and Reference Systems Service (IERS) Conventions (McCarthy and Petit, 2003, Chap. 7). The OTL correction Δc_i for an epoch t_i is given by

$$\Delta c_i = \sum_j A_j \cos\left[\omega_j \cdot (t_i - t_0) + \chi_j(t_0) - \phi_j\right] \tag{3.1}$$

where A_j is the amplitude, ω_j the angular velocity, χ_j the astronomical argument, ϕ_j the phase of the jth tidal constituent, and t_i is the time of the ith epoch. For the starting time t_0 of each time series, the astronomical arguments χ_j were computed with the subroutine ARG.f downloaded from the IERS's web-page (`ftp://tai.bipm.org/iers/convupdt/chapter7`). The angular velocities in Eq. (3.1) were the same as used in the ARG.f subroutine. The actual observing epochs and the sampling interval (one hour or 30 min) of the gravity observations, see Sect. 3.2, were used in the calculation of Δc_i.

Observations

During the summers of 2005 and 2006 several gravity stations in Norway were occupied by FG5-226 for 24 h of measurements or more. This study is based on data obtained at the stations in Table 3.1, see also Fig. 3.1.

FG5 measurements were collected in sets with a sampling interval of 1 h or

Table 3.1: Location of the gravity stations, duration of time series, and distance to tide gauge. The heights are orthometric and the reference system is WGS84.

Station	**Latitude**	**Longitude**	**Height**	**Length of time series**	**Dist. to tide gauge**
Honningsvåg	70.97761° N	25.96658° E	20.0 m	61 h[1] 36 h[2]	0.5 km
Tromsø	69.66280° N	18.93970° E	102.0 m	48 h	2 km
Andøya	69.27840° N	16.00870° E	370.0 m	48 h	7 km
Bodø	67.27972° N	14.39530° E	13.4 m	56 h	1 km

Time series collected in: [1] 2005, [2] 2006.

30 min. One set is the average of 50 drops, with an interval of 10 s between each drop. The data collection was paused at intervals of about 24 h to check the mechanical and optical set up of the FG5. The time series from one station thus consists of several data strings merged together.

The merged data have been processed using the software provided with the instrument, i.e., g_v4 from Micro-g Solutions Inc. The measurements are normally corrected for observed local atmospheric pressure, polar motion, and tidal effects (i.e. body tides and ocean tide loading) (Micro-g Solutions Inc.). The tide generating potential of Tamura (1987) and the Love numbers of the Wahr-Dehant-Defraigne model are used for the body tide correction in g_v4 (O. Francis, personal communication, 2007). Final polar motion parameters from the IERS were used (`http://www.iers.org`). In our processing all corrections were applied, except the OTL correction. The time series then produced, show periodic variations in phase with the local ocean tide. Residuals in µgal (10^{-8}m s^{-2}) were formed by subtracting the simple mean of the entire time series from each set.

All gravity stations are located within 7 km of a tide-gauge (cf. Table 3.1). The observed gravity signal is in phase with the observed ocean tide signal at the tide-gauges for all stations. Tide-gauge data were obtained from the website of the Norwegian Hydrographic Service (NHS) (`http://vannstand.statkart.no`). The observed water level for every 10th min was downloaded for the stations close to the gravity stations. Figure 3.2 shows the gravity measurements and the tide-gauge observations at Andøya. Note the artificially selected scales. The variation in the gravity measurements are in phase with the independent tide-gauge measurements. This indicates that the residual signals in the gravity observations are due to OTL. All other stations show the same pattern.

3.3 Observational results compared to global models

The time series observed with FG5-226 are shown in Fig. 3.3 together with a collection of global OTL models. Both observations and models are dominated by a semidiurnal pattern. The time series are too short (36 to 61 h) for frequency analysis. Instead, the amplitude A and phase ϕ for a semidiurnal signal were estimated for both observed and predicted time series in order to compare the over all pattern and size of the observations and the models. They were found in a least-squares adjustment according to the formula

$$y_i = A\cos(2\pi\, f\, t_i - \phi) \tag{3.2}$$

where y_i is observed or predicted value of the OTL effect at epoch t_i, and f is the semidiurnal frequency. The M2 frequency with period 12.42 h was chosen to estimate the amplitudes and phases since it is known to dominate the OTL

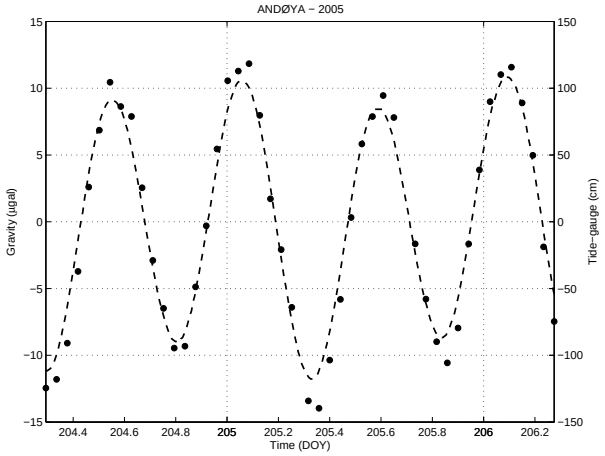

Figure 3.2: Andøya; observed gravity residuals (no OTL correction) in µgal (dots) and tidal ocean heights (dashed line) in centimeters. The mean is removed from the time series and the scales are artificially selected.

signal. The time scale is days elapsed since the turn of current year of observation (1 January, epoch 00.00). All estimated phases are referred to the selected epoch.

Generally in Fig. 3.3, the phases of the observed gravity residuals are within the range of the models, except for Honningsvåg, where the models are approximately 25 min advanced. The observed amplitudes are mostly larger than those of the models. The smallest difference is found for Tromsø and Bodø. There are significant differences for Honningsvåg and Andøya. This is also evident by the semidiurnal M2 amplitudes and phases summarized in Table 3.2.

The discrepancies between the global models vary from site to site, but generally they are not large. The global models were used to correct the gravity observations, and the RMS was calculated to quantify the variability in the time series. Different RMS values were obtained before and after the gravity observations were corrected and are summarized in Table 3.3. The RMS, as defined by Eq. (3.3), is a measure of a series total variance, i.e. the square root of the mean squared deviation of the observations (y_i) from the time series mean (Weisstein, 2007). In this analysis, every time series mean is zero. The percentage reduction in RMS is also considered.

$$RMS = \sqrt{\frac{1}{n}\sum_{i=1}^{n}(y_i - \bar{y})^2} = \sqrt{\frac{1}{n}\sum_{i=1}^{n} y_i^2} \tag{3.3}$$

Table 3.2: Estimated semidiurnal amplitudes in µgal and phases in degree for the observed gravity residuals (no OTL correction) and the different OTL models. All phases are referred to 1 January of the year of observation.

Station	Obs	SCHW	GOT00.2	FES95.2	FES2004	NAO99b	TPXO.7
Honningsvåg[1]	6.4	2.3	1.9	2.3	2.2	2.7	2.3
	203.9	200.4	192.9	192.8	186.8	181.9	197.1
Honningsvåg[2]	9.9	3.8	3.8	3.4	3.6	4.4	3.6
	100.1	98.0	86.7	92.3	86.5	81.4	93.9
Tromsø[1]	4.8	4.3	3.5	3.1	3.3	4.9	3.3
	136.3	152.9	140.9	141.9	132.7	134.7	141.8
Andøya[1]	11.0	8.5	7.9	8.3	7.8	9.3	7.7
	122.0	128.1	118.3	119.5	116.5	117.2	120.0
Bodø[1]	4.5	3.5	4.1	4.1	4.2	6.2	3.7
	115.9	120.3	117.1	115.5	115.3	117.8	117.9

Time series collected in: [1] 2005, [2] 2006.

Table 3.3: RMS for the gravity residuals corrected with different OTL models. No model means observations without any OTL correction. All units µgal.

Station	No model	SCHW	GOT00.2	FES95.2	FES2004	NAO99b	TPXO7
Honningsvåg[1]	5.5	4.2	4.5	4.3	4.4	4.2	4.3
Honningsvåg[2]	7.8	5.5	5.6	5.7	5.8	5.4	5.7
Tromsø[1]	3.8	1.9	1.9	2.0	2.0	1.6	1.9
Andøya[1]	8.0	2.2	2.5	2.3	2.6	1.7	2.7
Bodø[1]	3.5	1.4	1.2	1.3	1.2	1.7	1.4

Time series collected in: [1] 2005, [2] 2006.

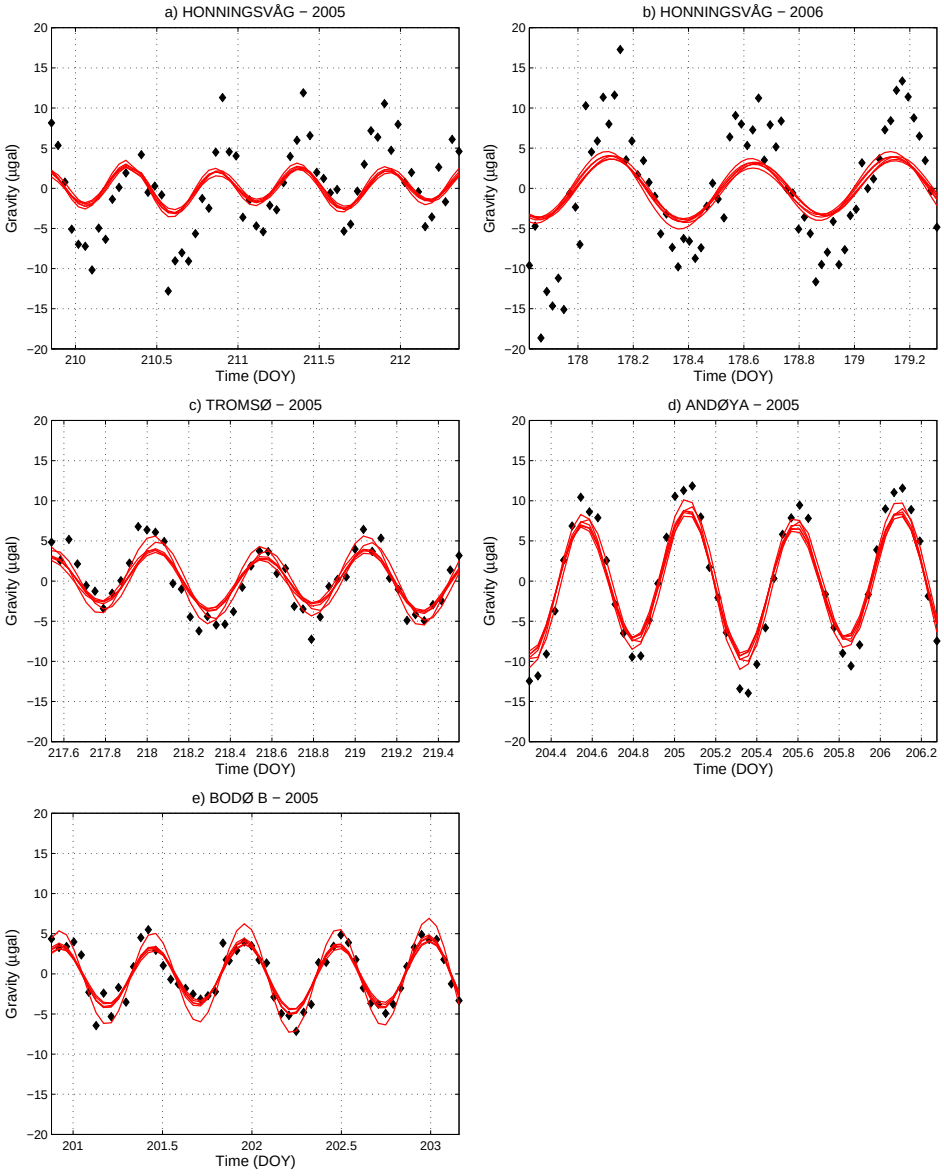

Figure 3.3: Time series of six global OTL models (solid lines) and observed gravity residuals (dots). The global models are Schwiderski, GOT00.2, FES95.2, FES2004, NAO99b and TPXO.7.

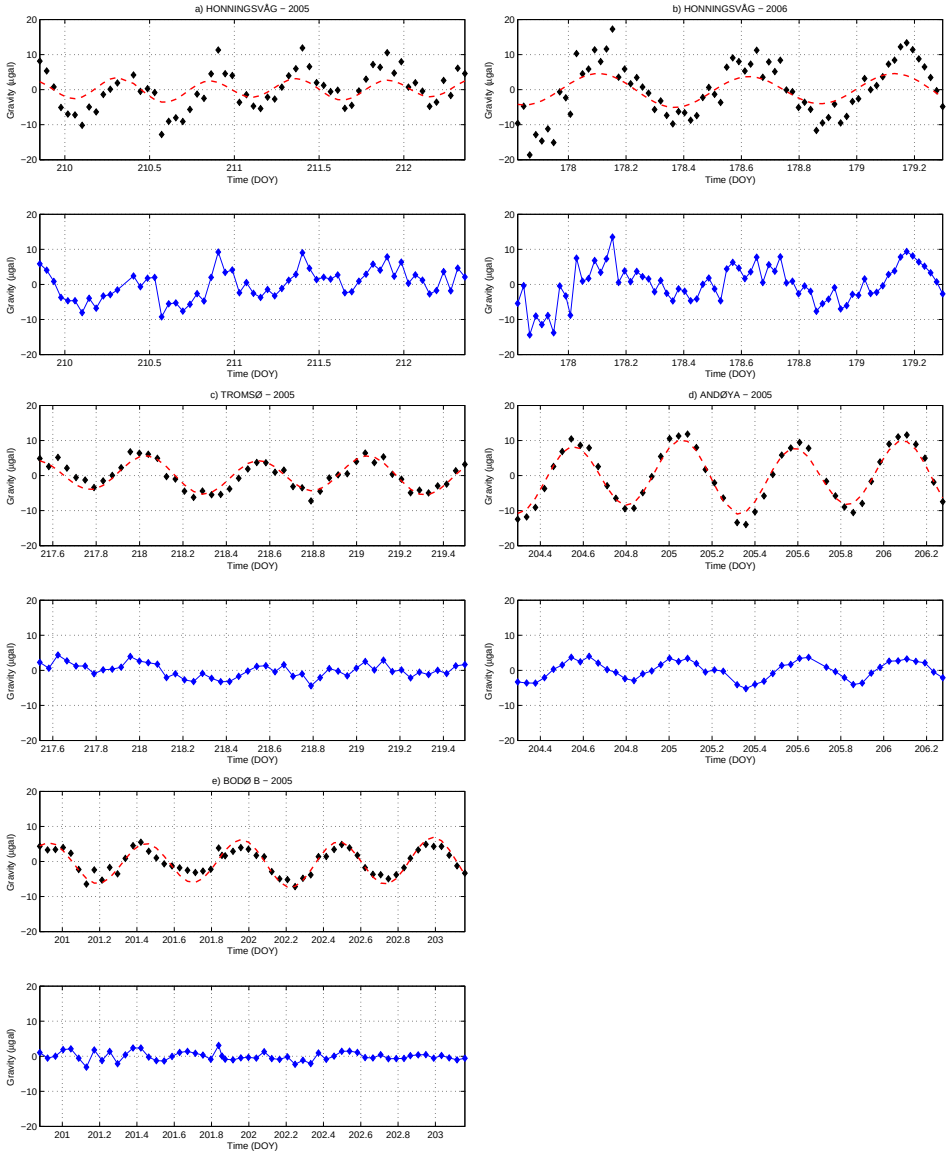

Figure 3.4: The upper panel for each station shows the time series of observed gravity residuals (dots) and the best OTL model (dashed line). The lower panel for each station shows the observations corrected with the best OTL model. In Bodø the OTL model is the FES2004, while it is the NAO99b in all other stations.

Honningsvåg

Honningsvåg is located on Magerøya, the northernmost island of mainland Norway. To the north is only open ocean, the Barents Sea. The station is located on the south side of the island, 20 m above sea level and 70 m away from the shore, see Fig. 3.9. Observations were made in 2005 and 2006. Noisy observations occurred both years, probably caused by strong winds. In Fig. 3.3a and 3.3b, the global models have amplitudes smaller than the observations. This is also seen in Table 3.2.

The observed signal has a semidiurnal amplitude of 6 and 10 µgal in 2005 and 2006, respectively. The corresponding amplitudes of the models are approximately 2 and 4 µgal. The models are approximately in phase with the observations, but slightly advanced. The closest fit is achieved by the NAO99b model, which has a marginally larger amplitude than the other models, but deviates most in phase, cf. Table 3.2. It reduces the RMS by 30 % in 2005 and with 24 % in 2006, cf. Table 3.3. Considerable variability remains in the observations, even after the OTL correction was applied. A semidiurnal signal with amplitudes of approximately 5 and 7 µgal is easily seen in Fig. 3.4a and 3.4b respectively. The global models do not explain the total observed signal.

Tromsø

Gravity station Tromsø is centrally located on an island, about 1 km from the sea and 102 m above sea level. The island is located in a fiord and it is surrounded by several larger islands, cf. Fig. 3.9. Figure 3.3c reveals a good correspondence between the observed signal and the global models, especially NAO99b. This is also evident in Table 3.2. Applying the NAO99b OTL model reduces the RMS with 58 % in Table 3.3 and almost completely removes the semidiurnal signal, as seen in Fig. 3.4c. The observed amplitude of 4.8 µgal in Table 3.2 is comparable to the M2 amplitude of 4.5 µgal found in Dittfeld *et al.* (1997), where approximately six months of data from a LaCoste & Romberg instrument were analyzed.

Andøya

Gravity station Andøya is located on a mountainous island, 370 m above sea level and 1.4 km in horizontal distance from the sea. The island faces the North Atlantic ocean, see Fig. 3.10. The distance to the edge of the continental shelf is 30 km. In Fig. 3.3d the global models nearly match the observed gravity signal. The amplitudes are slightly too small as seen in Table 3.2. The NAO99b model fits the observations marginally better than the other models and reduces the RMS by 79 %, see Table 3.3. In Fig. 3.4d a semidiurnal signal with an amplitude

of approximately 3 µgal remains when the observations are corrected with the NAO99b model.

Bodø

Gravity station Bodø is in the basement of a school in the center of the town. It is 13 m above sea level, 600 m from the shore. Bodø is located on a peninsula at the mouth of Saltfjorden. Many small islands protect it from the open ocean, see Fig. 3.10. The Bodø series contains three merged data strings, cf. Sect. 3.2. The first observation day has a shift of approximately 5 µgal relative to the following observations. This shift was treated as a bias. The time series was split into two parts, one for the first 24 measurements and one for the last 33. The mean was computed for each part, and these two different means were subtracted from the measurements to obtain the residuals.

The NAO99b model has a larger amplitude than the other models in Fig. 3.3e. This is also seen in Table 3.2 where the amplitude is 1.6 µgal larger than the observed one, while the rest of the models have smaller amplitudes than the observed. Applying the OTL corrections, both the GOT00.2 model and the FES2004 yield a RMS of only 1.2 µgal in Table 3.3. The RMS is reduced by 65 %. When the FES2004 or the GOT00.2 model is applied, the semidiurnal signal vanishes completely in Fig. 3.4e. The overall agreement between the observations and the models is good in Bodø.

3.4 A local approach

The global models match the observations well in Bodø and Tromsø, but a half-day periodic feature remains in Tromsø. In Honningsvåg and Andøya, the global models leave significant periodic signals in the time series. In an attempt to alleviate this situation, we have computed a local disk model for the four stations analyzed in this paper. The local model considers the gravitational effects of the direct attraction and the vertical displacement of each site. We employed the computations of H.-G. Scherneck and M. S. Bos, which allow to download the displacement effect and/or the total gravity effect. The third gravitational effect from redistribution of masses is not considered, since the OTL-provider website only provides the total gravity effect.

The direct attraction does not affect deformation measurements, but is a significant component when gravity is observed. If the station is less than 1 km from the coast, " ... the direct gravitational attraction of the tidal water mass is more than likely dominating the loading" (see `http://www.oso.chalmers.se/~loading/`). Thus, the variations in local ocean tides must be taken into account in order to obtain a good OTL correction for gravity measurements.

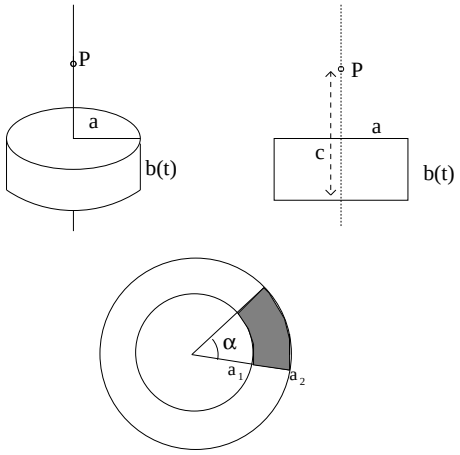

Figure 3.5: The figure illustrates the geometry used to calculate the direct attraction in an external point P from ocean tides modeled as disk sectors.

A simple model for the direct attraction can be developed by describing the water-masses as a circular disk with radius a and time dependent height $b(t)$ as given by the local tide-gauge observations. The observing point P is located on the axis of the disk at a distance c above the base of the disk, see Fig. 3.5. The attraction at P is obtained by (Heiskanen and Moritz, 1967, page 128)

$$A_e(t) = 2\pi G\rho\left(b(t) + \sqrt{a^2 + (c - b(t))^2} - \sqrt{a^2 + c^2}\right) \tag{3.4}$$

where G is the gravity constant ($6.67 \cdot 10^{-11}$ m^3 kg^{-1} s^{-2}) and ρ the average density of sea water (1027 kg m^3) (Heiskanen and Moritz, 1967).

The coastline of Norway is very complex. None of the observing points are surrounded only by water, thus a circular disk is geometrically incorrect. We model the water masses by sectors and compartments of sectors. The attraction from a sector is obtained by multiplying Eq. (3.4) with the factor $\frac{\alpha}{2\pi}$, where α is the opening angle of the sector. The attraction of a compartment (e.g. the marked part in Fig. 3.5) is given by

$$A = \frac{\alpha}{2\pi}(A(a_2) - A(a_1)) \tag{3.5}$$

where a_1 and a_2 are the radii of the circles bounding the compartment. The direct attraction from water-masses at a large horizontal distance from the observation point has a small effect on the observed gravity, thus only the near surroundings of the observing point is included in the model. Figure 3.6 shows that the water-masses within a radius of 10 km generate most of the attraction from a disk. The

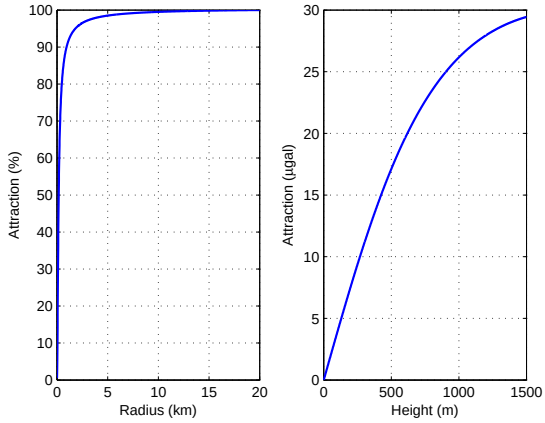

Figure 3.6: Left panel: The attraction from a disk changes for increasing radius, i.e. the percentage attraction from the disk compared with a Bouguer plate. The relative attraction is expressed as a percentage (calculated by $A_R/A\infty \cdot 100\,\%$ where A_R is vertical attraction from a disk of radius R, and A_∞ that of a Bouguer plate). An observation site 100 m above sea level and a circular disk with constant thickness 1 m were assumed. Right panel: Vertical component of the attraction from a torus of ocean tides versus the observations point's height above sea level. A disk with radius 1000 m was subtracted from a disk with radius 10000 m. This reflects a horizontal distance of 1000 m between the observation point and the sea. The torus was assigned a thickness of 1 m.

distance from the observing point to the sea is also an important parameter, so the non-existing "water masses" inside the solid rocks can be removed properly, see Fig. 3.7.

The direct attraction was computed from the observed local ocean tides according to Eq. (3.4). Figure 3.11 to 3.14 show the coastline and the circle sectors around each observation site to a radial distance of 10 km. All angles and radii are listed in Table 3.4. The full resolution coastline downloaded form Wessel and Smith (1996) was used to fit the sectors. This is the same coastline as used at the OTL-provider website. The entire ocean surface inside a given distance is assumed to experience the same tidal amplitude as that recorded by the nearby tide-gauge. The tide-gauge observations are given by NHS as heights of sea surface above Chart datum (`http://vannstand.statkart.no`). The time series mean was eliminated before the observations were substituted into Eq. (3.4).

The coastline is rather complex and the disks have occasionally a coarse fit to it. The computation is very sensitive to the land-sea distribution close to the

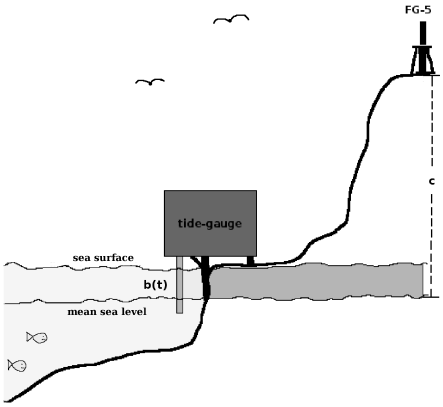

Figure 3.7: Schematic drawing of the observation situation and the modeled disk of water (see text).

Table 3.4: Radii in km (first row) and angles in degrees (second row) of the circle sectors in Fig 3.11 to 3.14. Asterisks identify sectors with land inside sectors of water.

Honningsvåg	A*	B*	C*	D	E	F	G*	
	4.5	1.9	1.2	10.0	10.0	1.4	0.3	
	35	30	55	179	35	95	160	
Tromsø	A*	B*	C*	D*	E*	F*	G	
	3.0	1.4	2.0	3.8	2.0	1.3	4.0	
	48	110	27	30	35	60	30	
	H	I	J	K				
	80	27	65	108				
	2.5	3.3	7.0	4.0				
Andøya	A*	B*	C*	D*	E			
	7.0	6.5	2.0	1.4	10.0			
	25	116	69	80	290			
Bodø	A	B	C*	D*	E*	F*	G*	H*
	10.0	6.0	2.0	4.0	3.2	1.0	4.0/3.0	2.5/1.8
	190	78	105	30	33	100	60	60

observation site. In Fig. 3.6 it is seen that good fit within 1 km of the observation site ensures that 91 % of the attraction is taken into account for a station with an elevation of 100 m. This percentage is dependent on the height of the observation site. If the height is 10 m, 99 % of the attraction is taken into account within 1 km. The highest observing site in this study is located at 370 m, where 67 % of the attraction is accounted for within 1 km.

Two numerical examples show that the water close to the observation site is most important for correct modeling of the direct attraction. First, consider the bay inside sector E in Bodø, which is incorrectly modeled as land (cf. Fig. 3.14). The distance from the observing site to the bay is 1.0 km to 1.5 km. The area is approximately 0.5 km^2, which represents 17 % of the area of sector E. If this area is covered with 1 m of water, the attraction would be about 0.04 µgal. This is only 1 % of the attraction of the entire E sector. Secondly, if sector F is divided in two, the area would be approximately the same as for the above mentioned bay, i.e. 0.5 km^2. This half F sector, however, is reaching from the observing site to 1 km, thus representing an attraction of 5.7 µgal if it is covered with 1 m of water. The attraction from the bay with the same area as the half F sector, but further away from the observation point, represents less than 1 % of these 5.7 µgal.

The vertical displacement of the Earth's crust due to OTL influences the measured gravity directly. Actually, for some stations the effect of the vertical displacement may exceed the direct attraction. The gravitational effect may be estimated by

$$\Delta g = \frac{\partial g}{\partial h} \Delta h, \tag{3.6}$$

when the vertical displacement Δh and the gravity gradient $\partial g / \partial h$ are known.

Some places in the world, e.g. Brest in France, the vertical displacement due to OTL is large and possible to observe by continuous GPS (Vey *et al.*, 2002). At our gravity laboratories, the displacement signal is weaker and within the noise level of GPS. Consequently, another approach was used in this analysis. In several studies global models are found to explain the displacement component of the OTL effect well (e.g. Khan and Scherneck, 2003). A global OTL model was thus used to quantify the vertical displacement from epoch to epoch. Amplitudes and phases for the displacement components were downloaded from the OTL-provider website. A time series was produced in accordance with the IERS Conventions (McCarthy and Petit, 2003, Chap. 7), taking nodal modulations into account. Then the gravitational effect of the vertical displacement was computed according to Eq. (3.6). NAO99b was used at Honningsvåg, Tromsø, and Andøya, and FES2004 was used at Bodø, because these models show the closest fit to the gravity observations (cf. Table 3.3). Density anomalies in the ground close to the observation point is capable of making local vertical free-air gravity gradients

deviating significantly from the standard free-air gradient. However, the standard gradient of 0.3086 µgal mm^{-1} (Heiskanen and Moritz, 1967, p. 131) should be used in Eq. (3.6), because the density anomalies experience the same displacement as the observation point.

The local model is compared to the observed gravity time series in Fig. 3.8. The gravity time series are dominated by a semidiurnal periodic variability which correlates closely with the local model. The phase and amplitude of the local model track the gravity observations, when the effects of both direct attraction and vertical displacement are included.

Table 3.5 shows resulting statistics, i.e. RMS before and after the observations are corrected in accordance with the two different effects of the local model and the sum of them. The same parameters are also shown for the best global model at each site.

Honningsvåg

Improved fits with the observations are obtained in Fig. 3.8a and 3.8b by applying local model corrections. The direct attraction effect is considerable and has a maximum value of 4.5 µgal in 2005 and 5.0 µgal in 2006. Accordingly, the maximum value of the vertical displacement effect is 4.7 µgal and 6.1 µgal for 2005 and 2006, respectively. The local OTL model captures more of the variability in the observations than the best global model. This is seen by comparing the RMS values in Table 3.5. The RMS is reduced by 42 % for the 2005-series and 47 % for the 2006-series when the local model is applied. The RMS reduction for the global NAO99b model were 24 and 30 % respectively, cf. Sect. 3.3. In contrast to Fig. 3.4a and 3.4b, the residual plots for Honningsvåg in Fig. 3.8a and 3.8b show no semidiurnal periodicity. The local model removes the periodic signal completely.

Tromsø

At Tromsø, the direct attraction effect is small, but it has a weak periodic signal. The maximum value of the direct attraction effect is 1.3 µgal and the vertical displacement effect is 6.2 µgal. When the local model is applied, the RMS is reduced by 61 %. The global NAO99b model reduced the RMS by 58 %. Thus, the local OTL model captures slightly more of the variability in the observations than the best global model. The local model removes the periodic signal completely in the lower panel of Fig. 3.8c.

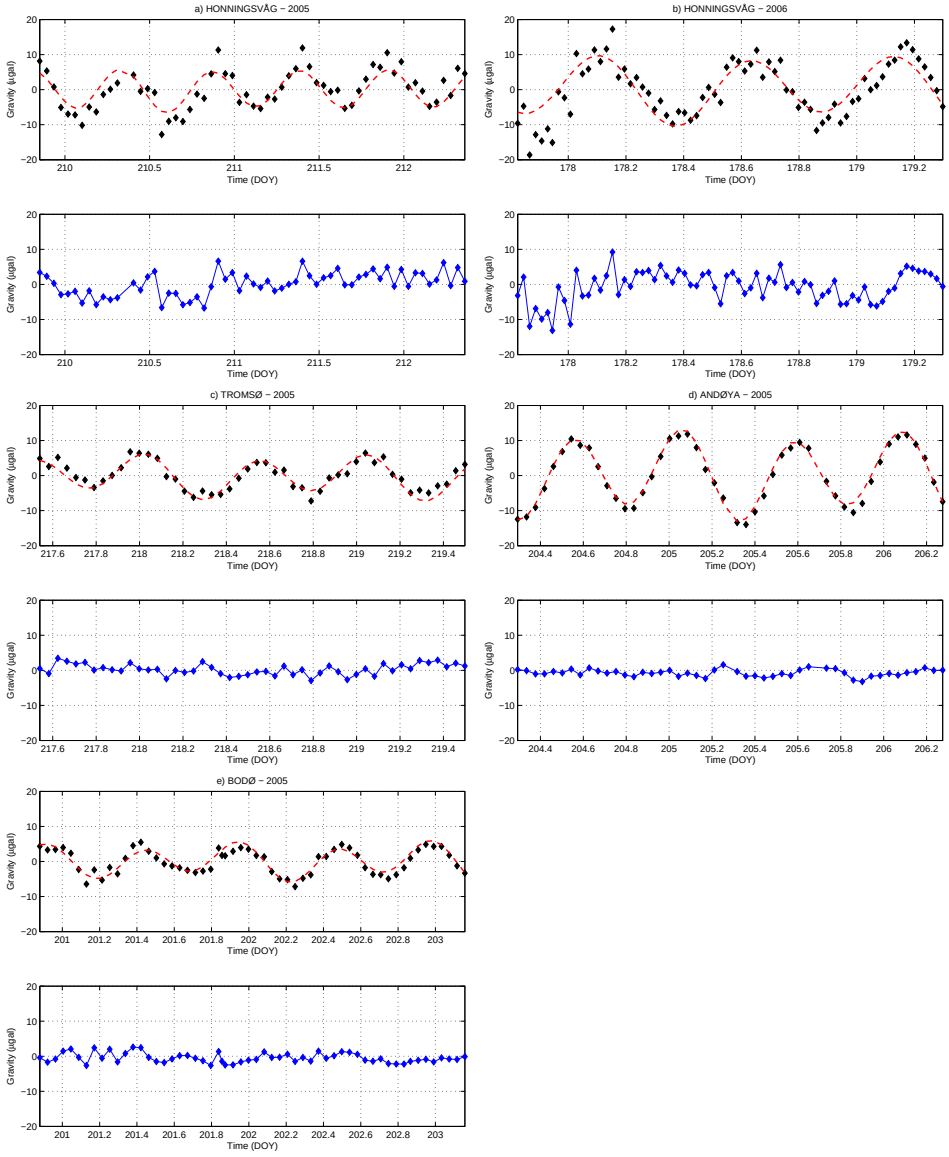

Figure 3.8: The upper panel for each station shows the time series of observed gravity residuals (black diamonds) and the local OTL model (red dashed line). The lower panel for each station shows the gravity observations corrected with the local OTL model.

Table 3.5: RMS for the gravity residuals corrected with different OTL models. No model means observations without any OTL correction. Global means the best global model according to Table 3.3. All units µgal.

Station	No model	Attr.	Disp.	Attr. + Disp.	Global
Honningsvåg[1]	5.5	3.9	4.1	3.2	4.2
Honningsvåg[2]	7.8	5.1	5.7	4.1	5.4
Tromsø[1]	3.8	3.2	1.5	1.6	1.6
Andøya[1]	8.0	5.5	2.8	1.0	1.7
Bodø[1]	3.5	3.3	1.5	1.5	1.2

Time series collected in: [1] 2005, [2] 2006.

Andøya

Both the direct attraction and the vertical displacement effects are considerable at Andøya. The maximum values are 4.3 µgal and 9.5 µgal, respectively. The periodic residual seen in Fig. 3.4d, is removed by the local model in the lower panel of Fig. 3.8d. The local model reduced the RMS by 88 % while the NAO99b model reduced it by 79 %. The local model captures the variability in the observations almost completely. The RMS for the gravity residuals is only 1.0 µgal, cf. Table 3.5.

Bodø

The direct attraction effect in Bodø is very small. The maximum value is only 0.2 µgal. This is not due to a small amplitude in the tide-gauge measurements, which is approximately 1 m at all stations in this paper. The vertical displacement effect is considerably larger, with a maximum value of 6.4 µgal. When the local model is applied, the RMS is reduced by 57 %. According to Sect. 3.3 the FES2004 model reduces the RMS by 65 %, a larger reduction than our local model. The periodic signal in the observations is however removed completely by both our local model (Fig. 3.8e) and by the global FES2004 model (Fig. 3.4e).

3.5 Discussion

Analysis of the local gravity OTL effects shows that the global models appear to fit well when the direct attraction is small. This is evident at Bodø, where the series shows almost no effect of the direct attraction and the global model removes the semidiurnal signal completely. At Tromsø, the direct attraction effect is small and the global models fit quite well. At Andøya and Honningsvåg, where a considerable direct attraction effect is present, the global models deviate from

the observations.

A possible explanation is inaccuracies in the global ocean tide models. This was checked by utilizing the software developed to compute the local models. Initially, we computed the direct attraction from locally observed tidal water, while a global model was used for the displacement. For comparison we have replaced the observed tidal water with modeled tidal water from NAO99b at all four stations. The modeled NAO99b tidal water was computed for the location of the tide-gauges with software downloaded from Matsumoto *et al.* (2006) and was then used in the local model. The differences between the local model when using observed and modeled tidal water are negligible. The largest difference was found for Andøya, where the mean difference was -0.4 µgal. Thus, the use of locally observed tidal water-masses may not be necessary in the modeling of the direct attraction. The global models appear to predict the tidal water sufficiently well.

The accuracy of the coastline close to the observing point is of crucial importance. If the mapped coastline has large deviations from the actual one close to the observation point, the calculation of the attraction will be incorrect. This is seen in Honningsvåg, where comparison to high resolution maps from the Norwegian N50 map-series (scale 1:50000) shows that a bay next to the observing site of approximately 0.1 km^2 is not included in the coastline used and accordingly is incorrectly modeled as land. If this bay, at a distance 70 m to 450 m from the observing site, is covered with 1 m of water, the direct vertical attraction is about 2 µgal.

The two parameters that influence the direct attraction strongest are the distance to the ocean in combination with elevation above the sea. Because of a more favorable angle to the water for an elevated observing site, the attraction from water-masses further away have an impact in addition to the water close to the observing site. It is the vertical component of the direct attraction that is recorded by a gravimeter.

As mentioned in Sect. 3.4, the OTL-provider website states that the direct attraction is dominating the OTL gravity effect close to the coast. This is not necessarily true, even if the station is less than 1 km from the shore. Gravity station Bodø, located 600 m from the sea, shows almost no effect of the direct attraction. Actually, the vertical displacement effect exceeds the direct attraction effect at all four stations in this study, cf. Section 3.4. On the other hand, the gravity laboratory at Andøya is located both quite close to the coast and has a considerable height above the sea. This suggests a considerable direct attraction, which is also shown by the local model.

As mentioned, the effect due to vertical displacement exceeds the estimated attraction from the ocean tides at all our study sites. Actually, Table 3.5 shows

Table 3.6: Standard deviations for the absolute gravity values when different OTL models were applied. All units µgal.

Station	SCHW	GOT00.2	FES95.2	FES2004	NAO99b	TPXO.7	Local
Honningsvåg[1]	0.54	0.57	0.54	0.56	0.53	0.55	0.40
Honningsvåg[2]	0.57	0.58	0.60	0.59	0.56	0.59	0.40
Tromsø[1]	0.29	0.28	0.31	0.29	0.23	0.29	0.23
Andøya[1]	0.33	0.37	0.34	0.38	0.26	0.40	0.14
Bodø[1]	0.18	0.16	0.16	0.16	0.20	0.18	0.18

Time series collected in: [1] 2005, [2] 2006.

that the RMS is reduced more at Tromsø if only the vertical displacement is accounted for instead of the complete local model. This is probably because the local model only includes two of the gravity effects. The third effect, redistribution of masses, was not addressed. A preliminary study indicates that this effect may be of significant importance. It is in anti-phase with the other two effects, thus dampening the total effect. This must be a subject for further studies.

The most prominent constituents of the OTL signal have semidiurnal periods and average close to zero if the FG5 data are collected during an integer number of twelve hour periods. This is almost true for the time series in this paper and reduces the impact of the OTL models on the mean absolute gravity value. We have estimated mean absolute gravity values using the observed gravity time series corrected with the individual global OTL models. Maximum differences between these mean absolute values reach 0.03 µgal (2005) and 0.19 µgal (2006) at Honningsvåg, 0.05 µgal at Tromsø, 0.20 µgal at Andøya, and 0.04 µgal at Bodø.

The standard deviations of the mean absolute gravity values are shown in Table 3.6. The differences between the global models are small, reaching only 0.15 µgal. In accordance with the RMS analysis, NAO99b appears to be the model which lowers the noise level most at Honningsvåg, Tromsø and Andøya. At Bodø there are no differences between the series corrected with GOT00.2, FES95.2 and FES2004. Compared to the best global models, the local model reduces the standard deviations at Honningvåg and Andøya, while it remains the same at Tromsø and is slightly increased at Bodø.

3.6 Conclusions

We have presented new gravity observations and compared them to a suite of published global OTL models. Time series of a few days for four arctic sites along the Norwegian coast reveal semidiurnal gravity variations that exceed the amplitudes predicted by the OTL models. The phases of the modern models

agree with observations. This results in a residual periodic signal of the gravity observations, after applying published models for all tidal effects. The NAO99b model predicts the observations best at three stations. For Tromsø, it predicts the periodic signal almost completely. At Honningsvåg and Andøya, a considerable residual periodic signal remains. The FES2004 and the GOT00.2 models predict the periodic signal completely at Bodø.

We have used a local approach in an attempt to remove the periodic signals. Two of the gravitational OTL effects, direct attraction and vertical displacement, are considered in a local model. We have used local tide-gauge observations to model the direct attraction from the ocean tides within 10 km from the observation point. A geometrical description of the local coastline is used to separate land from ocean. The gravitational effect due to vertical displacement is modeled by combining the free air gravity gradient and deformations predicted by a global OTL model. When the local OTL model is applied, we have shown that all periodic signals in the gravity observations are reduced considerably or completely removed.

By separation of the local effects, we have analyzed how gravity changes due to OTL arise at an observation point close to the coast. The direct attraction is not necessarily the dominant component of the gravity changes due to OTL, even if the station is located close to the ocean. However, the effect is considerable when the station is both close to the ocean and elevated above the sea surface. Additionally, the attraction component is extremely sensitive to an accurate coastline description close to the observing site.

We have also investigated the impact of using locally observed ocean tides and the tides predicted by the global NAO99b ocean tide model. The differences between the local OTL models when using the observed or predicted ocean tides are negligible. The choice of OTL model has little, if any, impact on the mean absolute gravity value. The local OTL model produces the smallest standard deviations for these mean values.

Acknowledgement

It is a pleasure to thank Olav Mathisen for interesting discussions and useful comments. Financial support from the Research Council of Norway through the Ocean Circulation and Transport between the North Atlantic and the Arctic Sea (OCTAS) project is gratefully acknowledged. Thanks are also due to the Norwegian Mapping Authority for access to their gravity laboratories and for in-kind contributions. Observations in Bodø and Andøya were made by Dr. Ove Omang. The authors thank the reviewers for their valuable comments which improved the manuscript.

Appendix 1: Detailed maps of the gravity laboratories

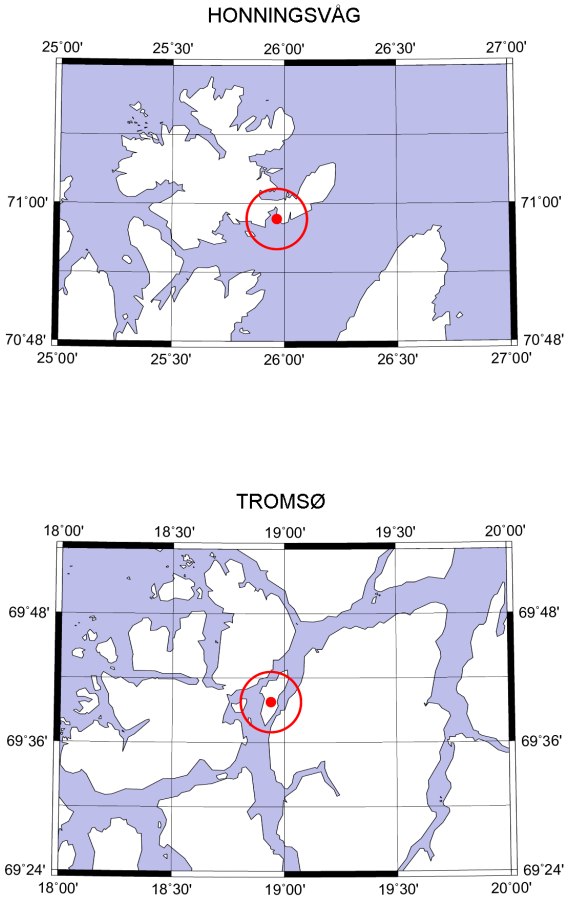

Figure 3.9: Detailed maps of the gravity laboratories. Dots mark the locations of FG5 observing sites.

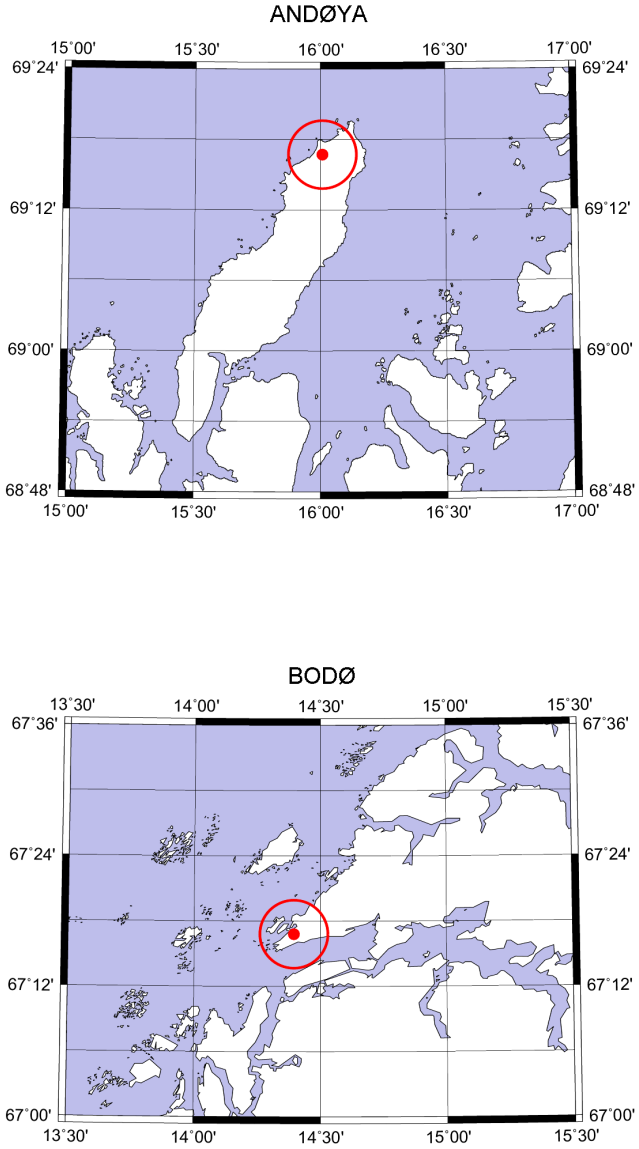

Figure 3.10: Similar to Fig. 3.9, but for Andøya and Bodø.

Appendix 2: Schematic drawing of the coastline and the circle sectors

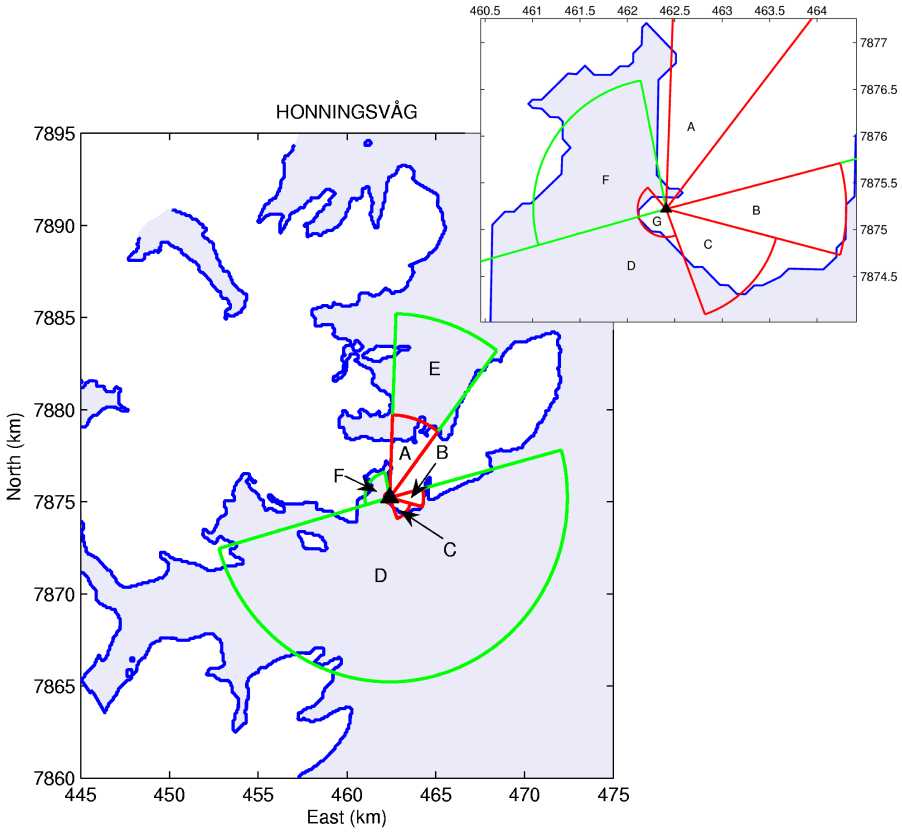

Figure 3.11: Schematic drawing of the coastline and the circle sectors at Honningsvåg. All green sectors are assumed to contain only water. Red sectors are eliminated from the computation because they represent solid bedrock. Thus, the attraction from the ocean tides is obtained by subtracting the red sectors from the green.

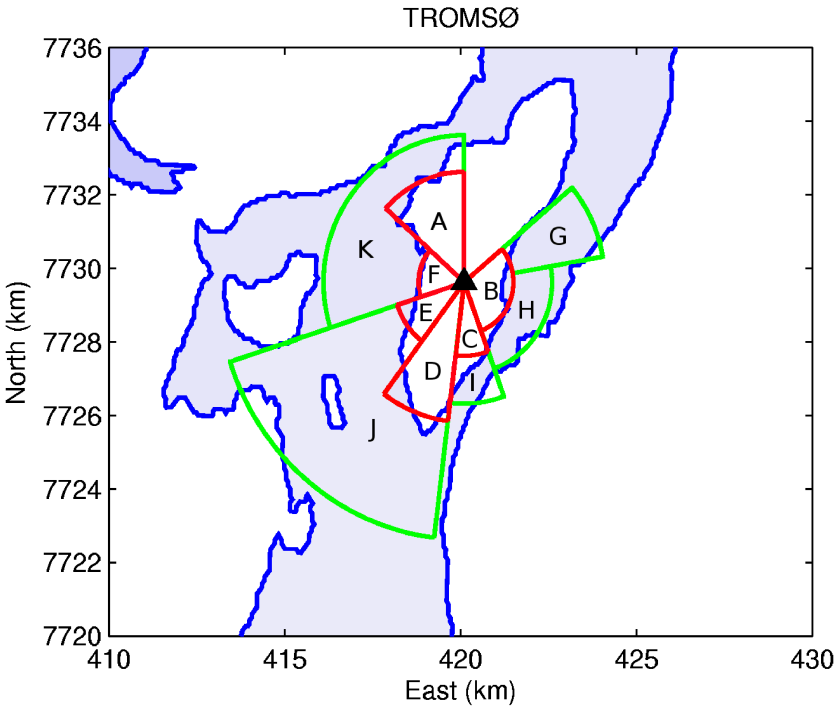

Figure 3.12: Similar to Fig. 3.11, but for Tromsø.

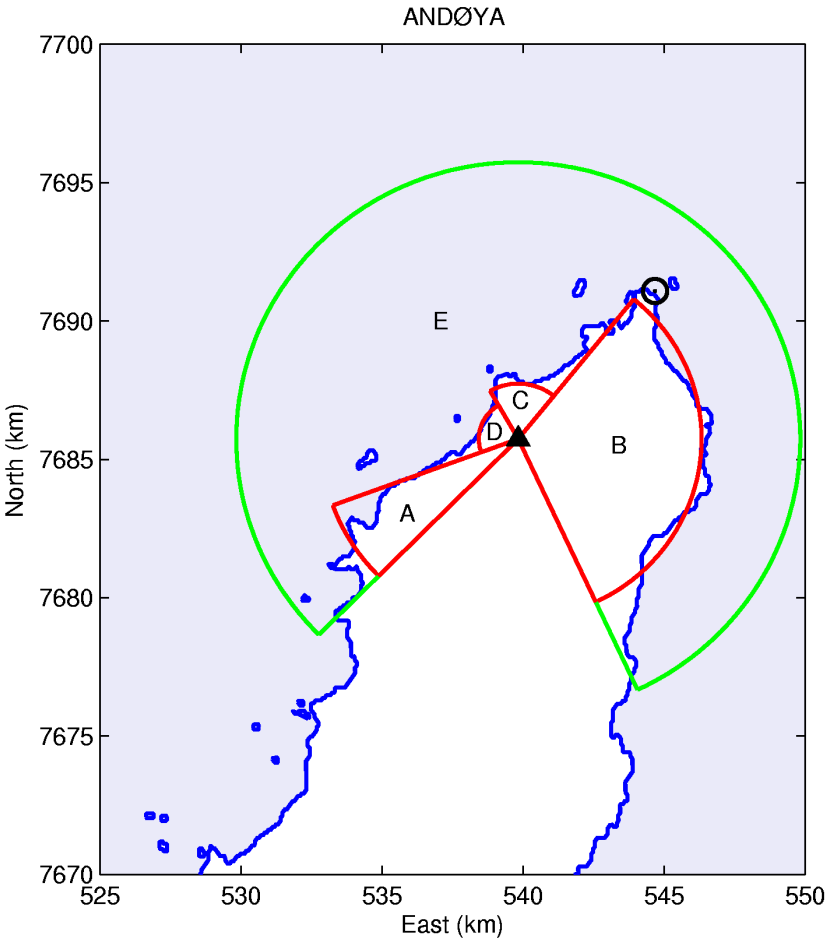

Figure 3.13: Similar to Fig. 3.11, but for Andøya.

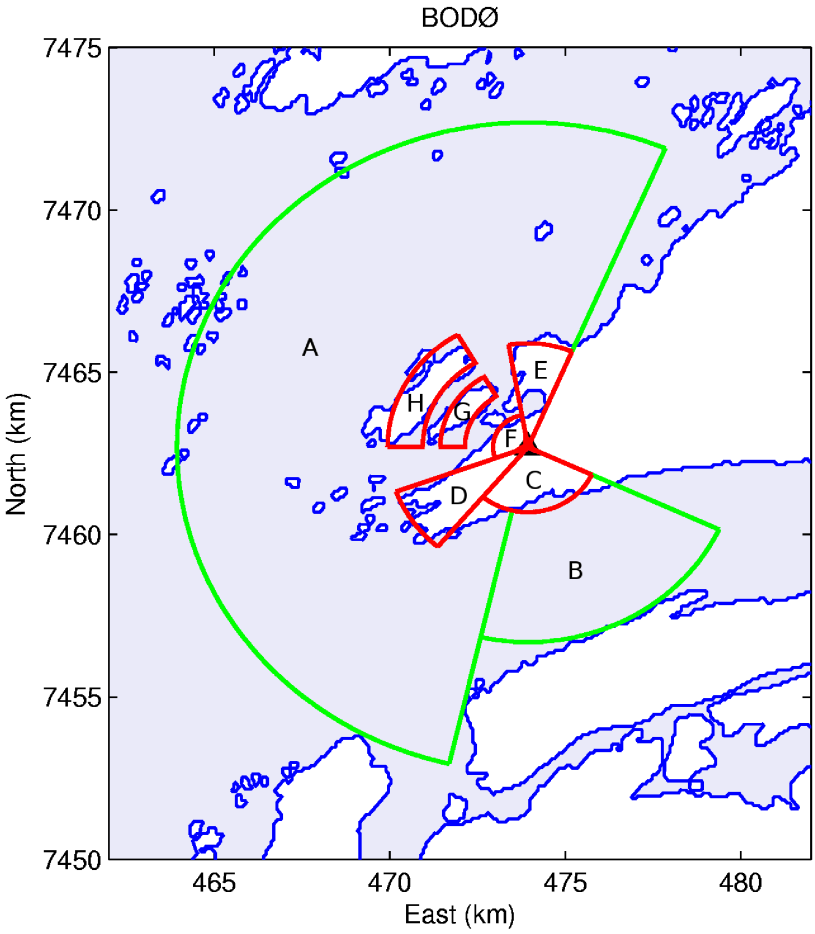

Figure 3.14: Similar to Fig. 3.11, but for Bodø.

Chapter 4

Paper C: Short periodic GPS height variability at arctic coastal stations

Abstract. Vertical displacements observed by GPS were analyzed at five stations along the Norwegian coast and at one station inland Sweden. For each station, the Bernese 5.0 software was used to estimate a one year long GPS height time series. The time series were transformed into periodograms to identify periodic signals. At all the coastal stations, the M2 constituent dominated the periodogram. In addition, the S2 constituent and a number of unidentified signals were detected at several stations. From the GPS height time series, we estimated the amplitude and phase of eight OTL constituents and compared them to a suite of global ocean tide loading models.

Unpublished manuscript

4.1 Introduction

This investigation addresses ocean tide loading (OTL) signals in GPS time series from high latitude stations along the Norwegian coast. The OTL signals from the Norwegian coast are of interest because Lysaker *et al.* (2008) demonstrated that the global OTL models at several stations underestimate the gravity change due to OTL in this area. Compared to absolute gravity observations, the global OTL models yield residuals with semidiurnal oscillations of nearly 10 µgal (1 µgal $= 10^{-8}$ m s^{-2}) peak to peak. Lysaker *et al.* (2008) presented an alternative scheme for modeling gravity changes due to OTL. The methodology relied on locally observed ocean tides and a global model for vertical displacement due to OTL. Without further investigations, the global models for vertical displacement were assumed more accurate than the gravity models. Hence, there is a need to validate the global OTL models along the Norwegian coast.

Several authors have previously studied geometrical deformations due to OTL, e.g. Sovers (1994); Dragert *et al.* (2000); Vey *et al.* (2002); Khan and Scherneck (2003); Petrov and Ma (2003); Allinson *et al.* (2004); King *et al.* (2005); Urschl *et al.* (2005); Melachroinos *et al.* (2007); Penna *et al.* (2008). They address displacements due to OTL in areas where the OTL signals are strong, e.g. the vertical OTL signal in Gulf of Alaska is 4 to 5 cm peak to peak, 10 to 12 cm peak to peak in Brittany, and the M2 signal reaches a magnitude of approximately 9 cm peak to peak in parts of UK. Along the Norwegian coast, the vertical deformations due to OTL are only 2 to 4 cm peak to peak and close to the noise level of GPS observations. Hence, OTL signals are easily mixed by spurious signals originating from e.g. mismodeled tropospheric path delay, multipath, and effects due to the semidiurnal orbital period of the GPS satellites.

We follow-up Lysaker *et al.* (2008) by analyzing GPS height time series from five stations along the Norwegian cost. The series are examined for both OTL signals and spurious signals by a periodogram analysis. In a second step, the amplitude and phase of the detected signals are estimated by least squares adjustment. The estimated constituents are compared to a suite of global OTL models. We also present a new methodology for validating the phase of predicted OTL signals when observations exist. By this, we investigate if significant discrepancies exist between models and observations, and if some OTL models are better than others in the study area. To investigate the possible existence of spurious signals, the continental station Arjeplog inland Sweden was included. This station was assumed to experience only minor deformations due to OTL. Any strong diurnal or semidiurnal signal at this station indicates a weakness of the chosen GPS processing strategy. Hence, Arjeplog is an appropriate station for validating the methods used to identify OTL signals at the coastal stations.

4.2 Methods and data

GPS-processing

The GPS analysis was done with the Bernese version 5.0 software (Dach *et al.*, 2007) which performs a double difference analysis for baseline computations. The baseline strategy has several advantages compared to precise point positioning (PPP) solutions. With double differences, errors and noise in satellite clocks, receiver clocks, and satellite ephemerides are eliminated, or at least strongly reduced. In addition, the geocenter motion due to OTL cancels in the inter-site distances (Khan and Scherneck, 2003).

Across the study area of northern Scandinavia, a network of baselines up to 300 km was formed. The challenge was the need to isolate the relative OTL-signal to one baseline endpoint. This was obtained by computing differential height changes relative to a continental station assumed to experience small OTL induced height changes. A star configuration was selected, using the continental station Kiruna (KIR0) as reference station for all baselines. The positions of the stations are listed in Table 4.1 and are graphically illustrated in Fig. 4.1. In contrast to double difference solutions, PPP yields absolute estimates of the deformations due to OTL (Allinson *et al.*, 2004). This is a significant advantage compared to the double difference solutions discussed in the present analysis.

For all stations, GPS observations were provided as RINEX files with sampling rate of 30 seconds by Statens Kartverk (the Norwegian Mapping Authority) and Lantmäteriet (The Swedish Mapping, Cadastre and Land Registration Authority). The GPS processing was based on IGS precise ephemerides, earth orientation parameters, and satellite clocks to ensure consistent information from the same solution. All positions of all stations were corrected for solid Earth tides, pole tides and permanent tides in accordance to the International Earth Rotation and Reference Systems Service Conventions (McCarthy and Petit, 2003). All GPS processing make use of relative satellite and receiver phase center models.

A stepwise procedure was followed to resolve the height changes from epoch to epoch. In a preliminary step, a simultaneous processing of the network provided daily position estimates without resolving the fixed ambiguities. Then, the L1 and L2 fixed ambiguities for each baseline were found by processing each baseline individually. A quasi ionospheric-free solution was obtained where the biases of the ionospheric refraction were reduced by introducing global ionosphere models. All fixed ambiguities and coordinates were saved and introduced as a priori known quantities in subsequent processing.

Final estimates of the temporal height changes were found by an ionospheric-free linear combination (L3) of the GPS observables. The processing strategy implied a common adjustment of position estimates and site specific zenith tro-

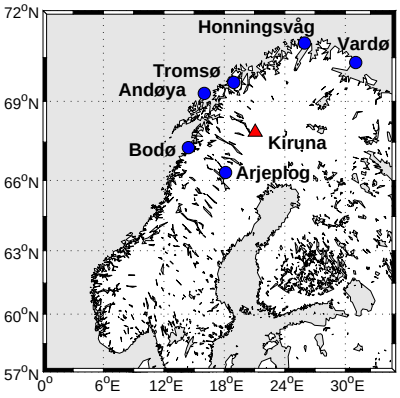

Figure 4.1: Map of the study stations Andøya, Arjeplog, Bodø, Honningsvåg, Tromsø, and Vadsø (circular markers) together with the reference station in Kiruna (triangle).

Table 4.1: Coordinates and ellipsoidal heights of the GPS stations. The time series from Andøya, Arjeplog, Bodø, Honningsvåg, Tromsø, and Vardø were analyzed for OTL and spurious signals while the station in Kiruna served as reference station in the GPS processing.

Station	**Longitude**	**Latitude**	**Height**
Andøya	16.0087° E	69.2780° N	370 m
Arjeplog	18.1249° E	66.3180° N	489 m
Bodø	14.4340° E	67.2875° N	68 m
Honningsvåg	25.9649° E	70.9771° N	54 m
Kiruna	21.0602° E	67.8776° N	498 m
Tromsø	18.9397° E	69.6628° N	102 m
Vardø	31.0312° E	70.3363° N	175 m

pospheric delay (ZTD) parameters. The coordinates were estimated as piecewise constants every hour and hence considered as kinematic. The estimated ZTD parameters were used as corrections to an a priori model of tropospheric path delay. We used the a priori model of Saastamoinen (Saastamoinen, 1973). For final processing a parameter spacing of 2 h was used. The Niell mapping function (Niell, 1996) was used to map both the wet and dry part of the troposphere with an elevation mask of 3°. Low elevation satellites are useful because the study stations are located at high latitudes and because low elevation satellites improve the geometry of the GPS solution. Horizontal tropospheric gradients were estimated by the tilting method every 24 h (Dach *et al.*, 2007). It should be noticed that the Niell mapping function is no longer recommended by the IGS guidelines which adopts the IERS conventions (Kouba, 2009). In the updated version of the IERS conventions (McCarthy and Petit, 2009), the Vienna Mapping Function 1 (Boehm *et al.*, 2006b) and the Global Mapping Function (Boehm *et al.*, 2006a) are recommended. These two improved models are not implemented in the official release of the Bernese GPS software.

In order to reduce the noise level in the GPS height time series, constraints were applied to the a priori horizontal coordinates. In general, heavily constrained horizontal coordinates may cause spurious signals in the vertical dimension which is here to be analyzed for OTL signals. Hence, the constraints must be balanced to allow movements which may occur in the horizontal dimension due to OTL. Differential displacements due to OTL were calculated from the ocean tide model FES2004 (Lyard *et al.*, 2006) for the time interval covered by the time series. The maximum values (see Table 4.2) were considered in order to find proper constraints. Horizontal displacements may reach 3.5 mm and vertical displacements may reach 20.0 mm. Thus, horizontal constraints were set to 0.02 m and a loose constraint of 1.00 m was selected for the vertical direction. These constraints are sufficient to allow the kinematic station freedom to move due to OTL.

Each baseline was processed separately to avoid propagation of unmodeled height changes between the stations in the network. In the preliminary step, a priori station coordinates were obtained by processing GPS observations corrected for changes due to OTL. In the final kinematic processing, no GPS observations were corrected for OTL.

For each epoch, the height residual was calculated with respect to a linear model fit to the height time series. The linear model included a trend only, i.e. no steps or seasonal cycle were estimated. Residuals three times larger than the standard deviation of the time series were classified as outliers and eliminated from the time series before further analysis. For all series, about one percent of the observations were identified as outliers. The GPS height time series are

Table 4.2: Maximum FES2004 predicted differential displacement in the vertical (UD), east-west (EW) and north-south (NS) directions due to OTL. The displacements were calculated between the reference station in Kiruna and the study stations.

Station	**UD**	**EW**	**NS**
Andøya	18.7 mm	1.5 mm	1.3 mm
Arjeplog	1.3 mm	0.5 mm	0.7 mm
Bodø	15.2 mm	2.7 mm	1.7 mm
Honningsvåg	14.8 mm	3.0 mm	1.5 mm
Tromsø	12.4 mm	2.0 mm	1.8 mm
Vardø	20.0 mm	3.5 mm	2.1 mm

graphically illustrated in Fig. 4.2.

Ocean tide loading models

OTL models were used in the preliminary steps of the GPS processing and for comparison with OTL signals estimated from the GPS height time series. Site-dependent amplitudes and phases for eleven OTL constituents (M2, S2, N2, K2, K1, O1, P1, Q1, Mf, Mm, and Ssa) were downloaded from the OTL-provider website of H.-G. Scherneck and M. S. Bos found at `http://www.oso.chalmers.se/~loading/` (Last visited September 2009). The OTL models were chosen to not include the effect of the Earth system's center of mass motion due to the ocean tides because this motion cancels in the inter-site distances (Khan and Scherneck, 2003).

Predictions of the vertical displacement due to OTL were calculated by Eq. (4.1) in accordance with McCarthy and Petit (2009).

$$\Delta c(t) = \sum_k f_k A_k \cos(\chi_k(t) + u_k - \phi_k) \tag{4.1}$$

$\Delta c(t)$ is the predicted effect of OTL at epoch t, and A_k, ϕ_k are site dependent amplitude and Greenwich phase lag for OTL constituent k. The astronomical argument χ_k can be calculated by the ARG.f subroutine provided by the IERS at `ftp://tai.bipm.org/iers/convupdt/chapter7` (last visited September 2009). Formulas for nodal modulation phase and amplitude corrections (u_k, f_k) were found in Schüler (2001).

For the initial GPS analysis, OTL corrections calculated from the FES2004 ocean tide model were used. This model was chosen because it is the latest of the models within the FES-family, and it is one of the models recommended in the

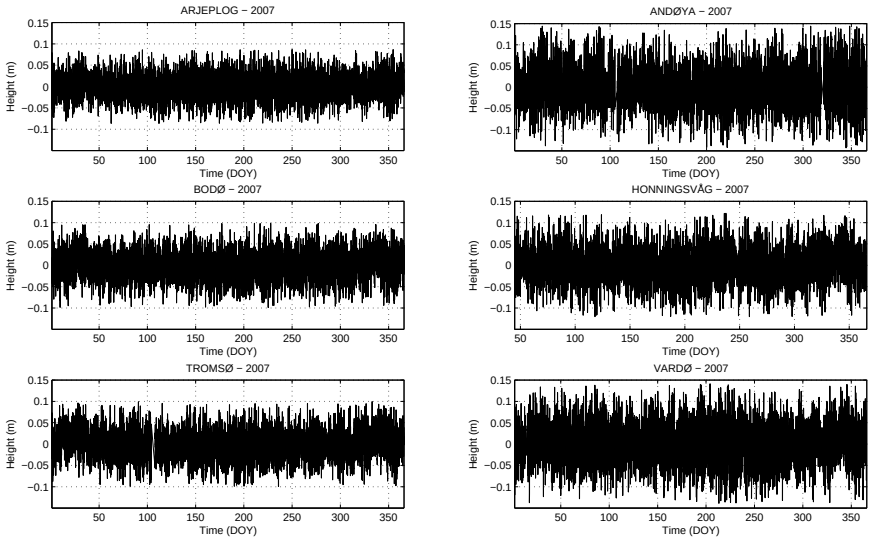

Figure 4.2: GPS height time series at Arjeplog, Andøya, Bodø, Honningsvåg, Tromsø, and Vardø.

updated version of the IERS Conventions (McCarthy and Petit, 2009).

For comparison, OTL predicted time series were used. They were calculated from ten different ocean tide models: Andersen 06 (AG06) (Andersen *et al.*, 2006), CSR4.0 (Eanes and Shuler, 1999), EOT08a, (Savcenko and Bosch, 2008), FES95.2 (Le Provost *et al.*, 1998), FES2004 (Lyard *et al.*, 2006), GOT00.2 (Ray, 1999), GOT4.7, NAO99b (Matsumoto *et al.*, 2000), Schwiderski (SCHW) (Schwiderski, 1980), and TPXO.7.1 (Egbert and Erofeeva, 2002). The list of models include the models discussed in Lysaker *et al.* (2008), and is expanded by AG06, EOT08a, CSR4.0, and GOT4.7 for completeness. A short review of the models are found at e.g. `http://www.oso.chalmers.se/~loading/tidemodels.html` and in Bos *et al.* (2002).

Periodograms

The GPS height time series were transformed into periodograms to evaluate the existence of any periodic components. We chose to use the redefined Lomb-Scargle transform (Scargle, 1982) because it handles unevenly spaced data. The present analysis addresses signals with diurnal and semidiurnal periods. The long periodic OTL constituents are weak and are not considered. Thus, the analysis was restricted to periods between 2 h (the Nyquist interval) and 30 h. This interval includes 29 independent frequencies and eight of the main diurnal and

semidiurnal OTL constituents. By truncating at 30 h we aim to include all nearly diurnal signals in the periodogram analysis.

A periodogram of noisy data is noisy. Large spurious peaks may occur and may erroneously be interpreted as signals. Hence, it is important to evaluate the statistical significance of the peaks in the periodogram. Scargle (1982) showed how a detection threshold can be calculated for data with noise variance equal to unity. For data with noise variance different from unity, the detection threshold must be scaled by the variance of the data series.

$$z_0 = -\sigma^2 \ln\left[1 - (1 - p_0)^{1/N}\right] \tag{4.2}$$

Here z_0 is the detection threshold, p_0 is a chosen false alarm probability, N is the number of independent periods to be evaluated, and σ^2 is the variance of the data series. The detection threshold sets a limit for peaks in the periodograms to exceed in order to be interpreted as real signals. With a chosen false alarm probability, the conclusion will only be wrong p_0 of the time.

4.3 Results

Analysis of the GPS height time series

Periodograms of the GPS time series are shown in Fig. 4.3 and 4.4. In order to distinguish signals and noise in the periodograms, the detection threshold was calculated for every GPS time series by Eq. (4.2). The detection threshold is illustrated by the horizontal dashed line in the periodograms. Peaks above the detection threshold indicate the presence of real signals in the time series. Smaller peaks are considered as noise. We choose a false alarm probability $p_0 = 0.01$. The periodogram at each station is discussed below:

- Three significant peaks are found in Arjeplog, but the periodogram from this station is flat compared to the periodograms at the other stations (notice the scale of the periodograms). The strongest peak has an estimated period of 23.93 h, i.e. one sidereal day. The origin of this signal could be the K1 constituent, or it could be an artifact of the double orbital period of the GPS satellites. The two other peaks are found at 12.42 h and 12.39 h. The first corresponds to the M2.

- At Andøya, the periodogram is dominated by M2 with a period of 12.42 h. Peaks at 11.97 h and 12.00 h correspond to the K2 and S2 tidal periods, respectively. Several other peaks are detected at periods of 4.92 h, 6.19 h, 7.63 h, 8.17 h, 8.36 h, 10.86 h, 11.57 h, 12.39 h, 21.08 h, 22.44 h, 25.70 h, and 27.7 h.

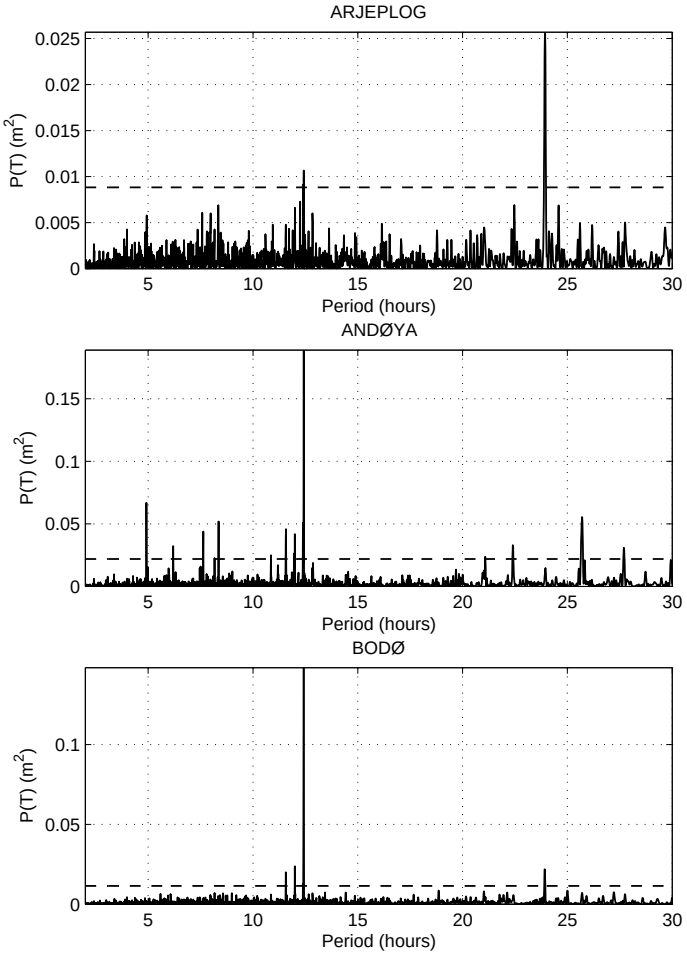

Figure 4.3: Periodograms of GPS height time series at Andøya, Arjeplog, and Bodø. The dashed line indicates the detection threshold. Notice that the figures are of different scale. The results are relative to the reference station in Kiruna.

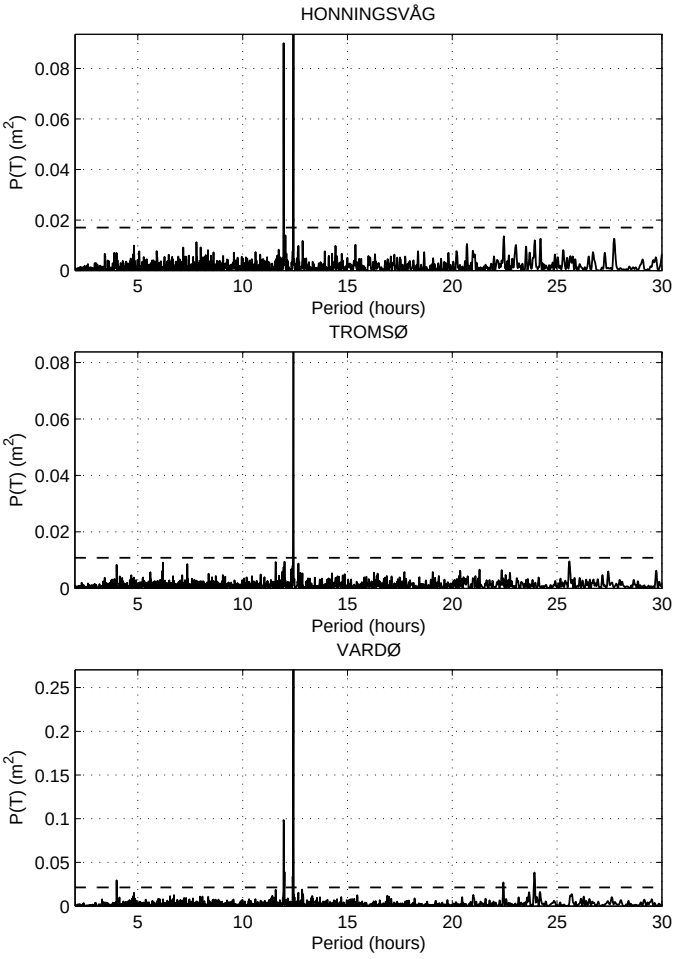

Figure 4.4: Similar to Fig. 4.3, but for the stations Honningsvåg, Tromsø, and Vadsø.

- In Bodø five peaks are detected, of which three have periods corresponding to OTL constituents (M2, S2, and K1). The peaks at 11.57 h and 12.39 h are unidentified.
- Two strong tidal signals are detected in Honningsvåg. They have periods corresponding to the M2 at 12.42 h and K2 at 11.97 h.
- The periodogram for Tromsø consists of one significant peak at the M2 tidal period. For all other periods, the periodogram is void of significant peaks.
- Vardø, located farthest east and bordering the Barents Sea, shows strong M2 and K2 peaks. Other peaks are found at 3.99 h, 12.00 h, 12.39 h, 22.40 h, and 23.94 h. The 12.00 h and 23.94 h peaks correspond to the S2 and K1 tidal periods, respectively.

Amplitudes and phases of the major signals

Amplitudes and phases of signals in the GPS height time series were estimated by least squares adjustment. The analysis includes eight semidiurnal and diurnal OTL constituents (M2, S2, N2, K2, K1, O1, P1, and Q1) as well as spurious signals identified in the periodograms in Fig. 4.3 and 4.4. For the eight OTL constituents, nodal modulation phase and amplitude corrections were applied and Greenwich phase lags were estimated, cf. Eq. (4.1). Local phase lags were estimated for the spurious signals. For comparison, amplitudes and phase lags were also computed for time series predicted from the OTL models. The results are tabulated in Table 4.3 and 4.5.

Some of the tidal constituents have periods close to each other, e.g. S2/K2, and K1/O1. The Rayleigh criterion was used to check which periods are possible to separate and distinguish from one year of data. The Rayleigh criterion implies that the duration of the recorded or modeled time, required to separate two frequencies f_1 and f_2, must be

$$\geq \frac{1}{|f_1 - f_2|} \tag{4.3}$$

(Foreman, 1977). Based on Eq. (4.3), the minimal length of a time series necessary to separate the eight main tidal constituents is 183 days. The length of the time series in the present analysis fulfills this criterion. For GPS data, even longer time series may be beneficial because some of the tidal constituents have weak signal to noise ratio.

Most of the periodic variability in the GPS time series was captured by the model used to estimate the amplitudes and phases. Hence, the calculated formal errors (standard deviations) in Table 4.3 are useful to quantify the accuracy of

the estimated OTL constituents. They were also used to evaluate the significance of the estimated signals. T-statistics were calculated for all estimated amplitudes:

$$T = \frac{\hat{A}}{\hat{s}} \tag{4.4}$$

In Eq. (4.4), $\hat{A}$ and $\hat{s}$ are estimated amplitude and corresponding standard deviation, respectively. A signal was considered as significantly different from zero and thus detected if T was greater than the upper $p_0/2N$ percentage point of the Student t_{n-N} distribution where n is the number of observations and N is the number of estimated frequencies to be evaluated. This corresponds to a Bonferroni quintile (Montgomery *et al.*, 2001). Because a different number of spurious signals are detected at each station, the Bonferroni quintile will also vary. With $p_0 = 0.01$, the Bonferroni quintiles are at 3.26, 3.48, 3.29, 3.22, 3.22 and 3.32 at Arjeplog, Andøya, Bodø, Honningsvåg, Tromsø and Vardø, respectively. The quintiles were calculated by Matlab. Only significant OTL constituents are compared to the OTL models. They are written with bold numbers in Table 4.3.

At Arjeplog, which was included to validate the processing strategy, signals with periods corresponding to M2, S2, and K1 have significant amplitudes. The estimated amplitudes are up to one order stronger compared to the model predictions. Considering also the phase of these signals, only M2 agrees with the models. If the OTL models are assumed to be correct, the analysis of Arjeplog shows that spurious signals with periods corresponding to the OTL constituents and amplitudes of up to 3 mm may arise.

At Andøya, five OTL constituents are significant, i.e. signals with periods corresponding to M2, S2, K2, K1, and O1. The M2 amplitude agrees within 1 mm for all models. The observed M2 phase deviates by up to 9.6° from the models. Only the phase of TPX0.7.1 agrees within one standard deviation. Fair agreement is also found for the S2 amplitude and phase. The phases of EOT08a, FES2004, GOT4.7, and NAO99b agree within one standard deviation from the observed S2 phase. For the other constituents the observed phases deviate strongly from the models.

In Bodø the M2, S2, N2, K2, and K1 constituents have significant amplitudes. The phase of M2, S2, and N2 agree within one standard deviation of most models.

For Honningsvåg, the M2, S2, N2, K2, and K1 amplitudes are significant, but only M2 agrees fairly well with models for both amplitude and phase. The estimated M2 phase fits exactly to the phase predicted by Schwiderski, but is 8.1 to 22° larger than the other models. This corresponds with Lysaker *et al.* (2008) who showed that the OTL models are slightly advanced with respect to the gravity observations at Honningsvåg. In the periodogram, K2 equaled the strength of M2 and the amplitude was estimated as large as 3.5 mm. This is not supported by

the models. In addition, the estimated K2 phase deviates significantly from the model predictions. This indicates an additional source to the K2 signal.

In Tromsø the M2, S2, N2, and K2 amplitudes are significant. Good agreements between models and observations are found for M2 and S2. The observed O1 phase agrees within 12° from all models, but the amplitude of the observed signal is not significant at the 99 % level.

In Vardø the M2, S2, N2, K2, and K1 amplitudes are significant. The amplitude and phase for M2 fit several of the OTL models. None of the models are within one standard deviation from the observed S2 phase. The phase of the K2 signal compares reasonably to models, but the amplitude is far too strong.

Standard deviations of the estimated amplitudes and phases are also found in Table 4.3. They reflect the noise level of the time series, i.e. for the amplitudes the smallest standard deviations are found at Arjeplog, Bodø, and Tromsø. All amplitudes are larger than the corresponding standard deviations, which are typically about ±0.5 mm. The standard deviations of the phases cover larger intervals and vary between stations and constituents. The strongest signals have the smallest standard deviations, e.g. for the M2 phase the standard deviation ranges from 3.2 to 12.0° while for the N2 phase it ranges from 12.3 to 24.5°.

The stability of the solutions were evaluated by processing the time series from Andøya with the reference epoch of the ZTD estimates shifted 30, 60, and 90 minutes with respect to the solution already discussed. For each of the time series, amplitudes and phases were estimated for the eight main OTL constituents. The results are tabulated in Table 4.4. In principle all solutions should be the same, but discrepancies exist. The amplitudes of the significant constituents vary by -0.6 to 0.4 mm and the phases by -12.18 to 10.9° from the mean of all solutions. The variation indicates the uncertainty resulting from the ZTD estimates alone. The uncertainties are comparable to the magnitude of the standard deviations estimated from the noise in the GPS time series.

The spurious signals tabulated in Table 4.5 are strong and reach several millimeters, e.g. at Andøya six signals have vertical amplitudes larger than 4 mm. All spurious signals found significant in the periodograms were also found to be significant with respect to the test in Eq. (4.4).

Table 4.3: Differential amplitudes in millimeters and phases in degrees for the OTL constituents estimated from GPS height time series and model predicted time series. The phase lags are with respect to Greenwich and lags positive. Significant estimates are written with bold numbers. The italic numbers represent estimated formal errors for the GPS estimates.

Site	**Model**	**M2**		**S2**		**N2**		**K2**		**K1**		**O1**		**P1**		**Q1**	
		A	ϕ	A	ϕ	A	ϕ	A	ϕ	A	ϕ	A	ϕ	A	ϕ	A	ϕ
Arjeplog	AG06	0.6	72.2	0.3	97.6	0.2	23.0	0.0	129.4	0.3	306.1	0.1	264.6	0.1	295.0	0.0	60.1
	CSR4.0	0.6	70.2	0.3	98.8	0.2	25.7	0.1	92.0	0.3	300.5	0.0	251.9	0.1	293.7	0.0	49.8
	EOT08a	0.7	77.8	0.2	119.5	0.2	46.4	0.0	115.1	0.2	298.5	0.0	252.4	0.1	299.7	0.0	65.2
	FES95.2	0.7	71.6	0.2	118.7	0.3	38.6	0.1	129.7	0.3	312.9	0.0	217.6	0.1	304.4	0.0	60.8
	FES2004	0.7	78.7	0.2	120.8	0.2	53.6	0.0	107.9	0.3	302.9	0.0	220.9	0.1	300.1	0.0	63.2
	GOT00.2	0.8	76.9	0.3	95.3	0.2	42.3	0.1	101.9	0.3	306.2	0.0	250.2	0.1	306.0	0.0	59.5
	GOT4.7	0.7	75.7	0.2	109.2	0.2	46.2	0.1	102.6	0.3	304.4	0.0	281.6	0.1	304.4	0.1	52.8
	NAO99b	1.0	60.9	0.3	100.2	0.2	51.7	0.1	91.6	0.2	314.8	0.0	276.8	0.1	301.6	0.0	35.2
	SCHW	0.9	77.2	0.3	109.4	0.2	45.8	0.1	113.2	0.2	295.9	0.0	217.7	0.1	300.0	0.0	56.8
	TPXO.7.1	0.8	75.8	0.2	124.9	0.2	33.3	0.0	81.2	0.2	309.1	0.0	315.3	0.1	308.8	0.0	52.1
	GPS	**2.0**	**70.9**	**1.7**	**88.8**	1.2	9.5	0.6	79.9	**3.1**	**264.6**	0.4	181.3	0.2	73.2	0.7	6.9
	Std	*0.4*	*12.0*	*0.4*	*13.3*	*0.4*	*20.5*	*0.3*	*31.8*	*0.4*	*6.6*	*0.3*	*52.5*	*0.4*	*104.3*	*0.3*	*26.5*
Andøya	AG06	9.7	156.2	4.3	205.1	3.1	136.1	1.1	213.4	1.6	13.0	0.7	237.8	0.5	1.8	0.3	176.4
	CSR4.0	9.9	155.1	4.2	207.8	3.3	136.3	1.2	207.8	1.6	15.4	0.4	234.3	0.5	8.4	0.3	177.5
	EOT08a	10.3	159.1	3.6	199.3	2.3	138.0	0.9	203.3	1.3	11.0	0.7	232.6	0.4	9.6	0.3	173.9
	FES95.2	9.9	160.9	3.5	203.6	3.1	134.9	1.0	213.8	1.1	4.9	0.6	230.2	0.3	355.9	0.3	176.7
	FES2004	10.3	158.2	3.6	199.5	2.4	139.9	0.8	200.3	1.3	11.2	0.7	232.7	0.4	8.6	0.3	174.8
	GOT00.2	10.5	159.7	4.2	207.1	2.3	134.6	0.9	216.9	1.2	6.5	0.7	235.8	0.3	3.3	0.3	176.4
	GOT4.7	10.5	159.6	3.8	201.4	2.3	137.7	1.0	205.6	1.1	11.2	0.8	228.4	0.3	8.8	0.3	178.1
	NAO99b	10.4	159.7	3.4	198.2	2.0	135.8	0.9	193.1	1.1	4.7	0.7	233.4	0.4	352.4	0.3	161.3
	SCHW	10.8	171.3	4.0	208.7	2.1	137.8	1.1	202.8	1.2	13.9	0.7	228.0	0.3	6.4	0.3	166.9
	TPXO.7.1	10.4	162.0	3.4	204.0	2.2	133.5	1.0	194.5	1.1	16.4	0.7	223.4	0.3	12.6	0.3	159.2
	GPS	**9.8**	**164.7**	**4.4**	**193.8**	1.5	108.4	**3.0**	**337.0**	**2.2**	**174.3**	**2.4**	**248.7**	1.3	267.6	0.8	245.1
	Std	*0.6*	*3.7*	*0.6*	*8.1*	*0.6*	*24.5*	*0.5*	*9.0*	*0.6*	*14.6*	*0.5*	*12.7*	*0.6*	*26.4*	*0.5*	*36.0*

Table continues on next page

Site	**Model**	**M2**		**S2**		**N2**		**K2**		**K1**		**O1**		**P1**		**Q1**	
		A	ϕ	*A*	ϕ	*A*	ϕ	*A*	ϕ	*A*	ϕ	*A*	ϕ	*A*	ϕ	*A*	ϕ
Bodø	AG06	8.1	144.9	2.9	185.9	1.8	121.1	0.8	200.4	1.4	350.4	0.7	241.6	0.4	339.9	0.3	148.9
	CSR4.0	8.2	144.7	2.9	188.2	2.1	120.4	0.8	189.7	1.2	353.5	0.4	236.5	0.4	343.0	0.2	153.6
	EOT08a	8.5	146.0	3.0	185.9	1.8	123.3	0.7	189.4	1.2	355.2	0.5	231.2	0.4	351.7	0.2	165.6
	FES95.2	7.6	146.2	2.9	186.7	2.1	112.8	0.8	196.7	1.0	356.1	0.5	222.8	0.3	343.7	0.2	145.4
	FES2004	8.4	145.6	3.0	186.4	1.9	125.5	0.6	189.1	1.2	355.2	0.5	231.1	0.4	352.0	0.2	168.5
	GOT00.2	8.9	146.5	2.8	187.0	1.9	120.2	0.6	197.0	1.2	352.9	0.7	232.3	0.4	349.8	0.2	144.4
	GOT4.7	8.8	146.0	3.0	187.4	1.9	124.3	0.8	192.0	1.2	355.0	0.6	224.9	0.3	352.8	0.2	164.2
	NAO99b	8.1	144.0	2.7	183.5	1.6	120.5	0.7	179.3	1.0	352.4	0.6	234.1	0.3	340.2	0.2	150.8
	SCHW	7.4	141.4	2.5	176.3	1.5	115.7	0.7	173.3	1.0	346.5	0.5	221.1	0.3	344.8	0.2	155.7
	TPXO.7.1	8.5	147.1	2.8	190.3	1.7	119.2	0.7	186.0	1.1	360.0	0.5	227.7	0.3	353.5	0.2	147.9
	GPS	**8.4**	**140.2**	**3.3**	**187.6**	**1.7**	**108.2**	**1.2**	**113.0**	**2.8**	**330.1**	0.9	232.4	0.5	244.8	0.5	281.9
	Std	*0.5*	*3.2*	*0.4*	*7.9*	*0.5*	*15.5*	*0.3*	*16.3*	*0.4*	*8.4*	*0.4*	*25.4*	*0.4*	*54.2*	*0.4*	*41.9*
Honningsvåg	AG06	7.4	228.3	3.2	268.2	2.5	203.6	0.7	278.8	1.7	85.7	0.2	228.7	0.5	70.0	0.3	198.8
	CSR4.0	7.3	230.0	3.2	271.2	2.5	204.7	0.9	269.7	1.7	85.9	0.2	348.4	0.5	80.3	0.3	196.4
	EOT08a	8.6	238.4	2.4	277.7	2.1	211.8	0.6	281.0	1.4	64.2	0.3	248.7	0.5	63.8	0.3	205.5
	FES95.2	7.8	238.6	2.4	279.5	2.9	213.5	0.7	281.7	1.1	89.0	0.2	234.1	0.3	81.4	0.3	199.9
	FES2004	8.5	237.4	2.4	277.6	2.1	211.6	0.4	263.2	1.4	65.8	0.3	249.8	0.5	61.7	0.3	205.2
	GOT00.2	8.3	242.2	3.3	269.1	2.0	212.4	0.7	279.7	1.3	80.1	0.4	234.1	0.4	81.2	0.3	199.6
	GOT4.7	8.6	242.0	2.6	278.5	2.0	215.6	0.6	280.2	1.1	77.8	0.3	224.6	0.3	78.1	0.4	210.7
	NAO99b	8.1	238.7	2.1	277.6	1.6	231.1	0.5	271.2	0.9	75.9	0.3	230.6	0.3	62.5	0.2	188.2
	SCHW	7.8	250.3	2.4	283.6	1.7	216.9	0.7	282.0	1.1	74.8	0.2	232.8	0.3	75.3	0.2	193.2
	TPXO.7.1	8.4	241.8	2.3	285.0	2.1	199.8	0.7	257.7	1.1	75.1	0.4	223.0	0.3	87.9	0.2	186.0
	GPS	**7.3**	**250.3**	**2.0**	**338.8**	**2.1**	**178.9**	**3.5**	**333.2**	**2.3**	**134.1**	0.4	211.6	0.9	58.0	0.6	297.1
	Std	*0.6*	*4.8*	*0.6*	*16.6*	*0.6*	*16.4*	*0.5*	*7.5*	*0.5*	*13.2*	*0.5*	*66.3*	*0.6*	*38.0*	*0.5*	*51.2*

Table continues on next page

Site	**Model**	**M2**		**S2**		**N2**		**K2**		**K1**		**O1**		**P1**		**Q1**	
		A	ϕ	A	ϕ	A	ϕ	A	ϕ	A	ϕ	A	ϕ	A	ϕ	A	ϕ
Tromsø	AG06	6.5	164.8	3.0	213.9	2.2	145.7	0.7	220.8	1.0	28.0	0.3	232.0	0.3	16.1	0.2	179.1
	CSR4.0	6.6	164.4	3.0	216.9	2.3	146.5	0.8	216.7	1.0	29.9	0.3	237.6	0.3	23.6	0.2	179.6
	EOT08a	6.6	169.0	2.3	208.4	1.5	148.5	0.6	212.2	0.8	22.3	0.4	234.9	0.3	22.4	0.2	179.8
	FES95.2	6.6	172.1	2.3	213.8	2.1	148.8	0.7	223.4	0.6	20.8	0.4	231.5	0.2	11.0	0.2	180.2
	FES2004	6.6	167.9	2.3	208.4	1.6	149.7	0.5	207.0	0.8	23.2	0.4	235.2	0.3	20.1	0.2	180.3
	GOT00.2	7.1	170.6	3.0	216.1	1.6	146.9	0.7	224.9	0.7	23.0	0.4	234.5	0.2	20.2	0.2	180.4
	GOT4.7	7.0	170.5	2.6	210.4	1.6	148.6	0.7	214.1	0.7	24.8	0.5	228.7	0.2	23.2	0.2	186.3
	NAO99b	7.5	170.3	2.4	207.5	1.4	147.6	0.6	201.6	0.7	15.7	0.5	232.1	0.2	2.7	0.2	164.4
	SCHW	7.1	183.4	2.5	220.6	1.4	150.8	0.7	215.6	0.7	27.7	0.4	230.3	0.2	21.4	0.2	172.0
	TPXO.7.1	7.0	172.8	2.2	213.2	1.5	143.6	0.7	204.8	0.7	29.0	0.4	223.8	0.2	26.1	0.2	164.2
	GPS	**6.4**	**168.0**	**2.0**	**217.1**	**2.0**	**125.7**	**1.1**	**325.9**	0.7	248.8	1.0	225.4	0.5	122.3	0.6	303.0
	Std	*0.5*	*4.1*	*0.4*	*12.4*	*0.5*	*13.0*	*0.3*	*17.2*	*0.4*	*32.9*	*0.4*	*20.7*	*0.4*	*53.0*	*0.4*	*37.0*
Vardø	AG06	10.4	288.4	3.9	336.2	3.2	266.5	0.9	351.4	2.7	108.1	0.0	24.1	0.7	94.9	0.3	217.3
	CSR4.0	10.8	289.0	4.0	337.7	3.3	267.2	1.1	338.7	2.7	107.7	0.4	43.0	0.8	103.0	0.3	212.6
	EOT08a	12.1	297.8	3.5	344.7	2.7	267.2	0.8	350.4	1.9	85.0	0.1	316.8	0.6	81.9	0.3	222.4
	FES95.2	12.2	297.1	3.8	344.3	4.3	268.6	1.0	350.9	1.9	108.4	0.0	300.1	0.6	102.9	0.3	217.5
	FES2004	11.8	297.5	3.5	344.5	2.7	267.5	0.5	348.0	1.9	85.6	0.2	313.5	0.6	80.2	0.3	222.2
	GOT00.2	12.7	298.1	3.9	336.1	2.7	269.6	0.9	349.8	2.0	102.4	0.1	286.9	0.6	102.0	0.3	218.0
	GOT4.7	12.7	298.9	3.7	343.5	2.8	269.3	0.9	348.2	1.7	102.9	0.1	230.9	0.5	103.2	0.4	222.0
	NAO99b	11.6	296.8	3.3	344.6	2.7	282.0	0.8	342.3	1.6	106.2	0.0	292.7	0.5	95.3	0.2	209.2
	SCHW	12.4	304.5	3.7	345.6	2.4	270.6	1.1	345.6	1.7	98.8	0.1	258.5	0.6	97.7	0.2	211.2
	TPXO.7.1	12.2	297.5	3.6	347.7	2.5	253.8	0.8	322.4	1.7	102.7	0.2	228.1	0.5	110.7	0.2	206.5
	GPS	**11.5**	**298.8**	**4.2**	**356.8**	**2.9**	**282.4**	**5.6**	**347.9**	**3.8**	**168.3**	0.8	266.4	1.8	37.8	0.6	330.4
	Std	*0.6*	*3.2*	*0.6*	*8.3*	*0.6*	*12.3*	*0.5*	*4.8*	*0.6*	*8.4*	*0.5*	*36.0*	*0.6*	*19.7*	*0.5*	*45.8*

Table 4.4: Amplitudes in millimeters (first row) and phases in degrees (second row) for Andøya estimated from time series processed with the ZTD estimates shifted in time (ΔT). The time shift is in minutes.

ΔT	**M2**	**S2**	**N2**	**K2**	**K1**	**O1**	**P1**	**Q1**
0	9.8	4.4	1.5	3.0	2.2	2.4	1.3	0.8
	164.7	193.8	108.4	337.0	174.3	248.7	267.6	245.1
30	10.2	5.2	1.2	3.2	2.2	2.2	1.9	1.4
	171.0	193.2	105.6	343.7	179.4	255.2	286.8	191.6
60	10.2	5.3	1.8	3.3	2.4	1.9	1.5	1.3
	171.5	193.8	96.2	335.1	178.5	232.1	305.3	184.9
90	10.6	5.0	1.7	3.7	2.3	2.3	0.8	0.6
	166.5	197.5	131.8	333.4	175.6	241.1	327.0	246.3
Mean	10.2	5.0	1.6	3.3	2.3	2.2	1.4	1.0
	168.4	194.6	110.5	337.3	177.0	244.3	296.7	217.0

Table 4.5: Estimated differential amplitudes (mm) and phases (degrees) for spurious signals detected in the periodogram analysis of the GPS height time series. The phase lags are local.

Andøya	Period	4.92 h	6.19 h	7.63 h	8.17 h
	A, ϕ	5.7 103.1	3.9 340.8	4.6 87.2	3.3 216.8
	Period	8.36 h	10.86 h	11.57 h	12.39 h
	A, ϕ	5.0 265.3	3.4 122.0	4.4 287.8	4.7 107.4
	Period	21.08 h	22.4 h	25.7 h	27.7 h
	A, ϕ	3.5 214.0	3.8 41.2	4.9 332.8	3.9 253.2
Arjeplog	Period	12.39 h			
	A, ϕ	1.8 98.0			
Bodø	Period	11.57 h	12.39 h		
	A, ϕ	3.0 192.5	1.5 141.1		
Vardø	Period	3.99 h	12.39 h	22.4 h	
	A, ϕ	3.8 75.9	3.2 52.2	3.6 195.4	

4.4 Discussion

The results and accuracy estimates from the Norwegian coast endorse other similar studies from different regions of the world. Khan and Scherneck (2003) analyzed 49 days of GPS data from Gulf of Alaska and demonstrated that M2 could be observed by GPS. The authors also foretold that the S2, N2, O1, Q1, and P1 constituents are detectable by GPS. This assumption was confirmed by the present analysis for S2 and partly for N2. Signals of the other OTL constituents are not confidently detected in the GPS time series of the present analysis.

Table 4.6: RMS misfit between models and observations.

Model	**RMS**
AG06	1.4 mm
CSR4.0	1.4 mm
EOT08a	1.0 mm
FES95.2	0.9 mm
FES2004	1.0 mm
GOT00.2	1.0 mm
GOT4.7	1.0 mm
NAO99b	0.9 mm
SCHW	1.2 mm
TPXO.7.1	0.9 mm

The best OTL model for the study area was tentatively identified by calculating the RMS misfit between observations and models. We used an equation similar to Eq. (1) in Yuan *et al.* (2008).

$$\text{RMS(model - gps misfit)} = \sqrt{\frac{1}{m}\sum_{j=1}^{J}\sum_{k=1}^{K}|Z_{k,j}|^2} \tag{4.5}$$

$$Z_{k,j} = A_{\text{GPS}}\left(\cos\phi_{\text{GPS}} + i\sin\phi_{\text{GPS}}\right)_{k,j} - A_{\text{model}}\left(\cos\phi_{\text{model}} + i\sin\phi_{\text{model}}\right)_{k,j} \tag{4.6}$$

In Eq. (4.5), it is summarized over $j = 1 \ldots J$ stations and $k = 1 \ldots K$ constituents. We focus on only the constituents confidently established, i.e. the M2 OTL signal at all stations, S2 at Andøya, Bodø, and Tromsø, and N2 at Bodø. All stations considered, this yields in total $m = 10$ constituents in the sum. The results are listed in Table 4.6 for each model. The differences between the models are small. Still, FES95.2, NAO99b, and TPXO.7.1 give the smallest RMS, while AG06, CSR4.0, and Schwiderski give the largest RMS. These results are partly in conflict with Allinson *et al.* (2004) who report the FES95.2 model to be the worst for stations on the British Islands.

When an OTL model is out of phase with the real signal, periodic oscillations will be generated in the residuals. Assuming perfectly modeled amplitudes, Fig. 4.5 shows the size of a phase error necessary to generate periodic residuals with an amplitude of 1 mm. The results are independent of the period of the constituent, but the figure clearly shows that a phase error is more critical for a constituent with large amplitude. For a signal with an amplitude of 10 mm (cf. the M2 constituent at Andøya), a phase shift of 6° generates periodic residuals with an amplitude of 1 mm. On the other hand, a 3 mm signal can be out of phase

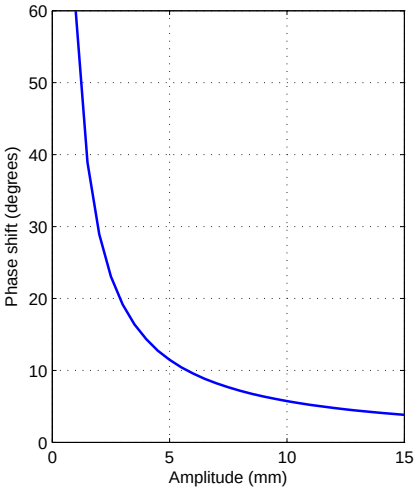

Figure 4.5: The phase shift necessary to generate periodic residuals of 1 mm amplitude depends on the amplitude of the signal. Example: A phase shift of approximately 6° generates a 1 mm error for a 10 mm amplitude signal.

by nearly 20° before the residual signal reaches an amplitude of 1 mm. This involves that the accuracy of the predicted phase of a weak signal is not critical for practical applications.

The curve in Fig. 4.5 can be used as an alternative method to evaluate phases predicted by OTL models. Firstly, the maximum allowed amplitude of the residuals must be established, e.g. 1 mm. Then, a curve similar to Fig. 4.5 can be calculated. The predicted phase is only approved if it deviates by less than indicated by the curve. For the M2 constituent in Table 4.3, most models fulfill this criteria. Exceptions are AG06, CSR4.0, FES2004 and Schwiderski at Andøya, TPXO.7.1 at Bodø, AG06 and CSR4.0 at Honningsvåg, CSR4.0 at Tromsø, and AG06, CSR4.0 and Schwiderski at Vardø.

The analysis of the GPS time series has revealed signals with periods corresponding to OTL constituents, but where the phase indicates an origin different from OTL. This applies to the K1 and K2 signals which are significant at several stations. The K1 and K2 tidal periods correspond with the orbital period of the GPS satellites. The correspondence makes it difficult to obtain K1 and K2 estimates free of GPS related systematic errors. In Allinson *et al.* (2004), it was found that the K2 phase differences between models and observations are typically in excess of 100° with consistent over-estimation of the amplitude. Similar results

were found at all stations discussed in this analysis.

Systematic errors are likely to be the origin of the strong 11.97 h signal observed at Honningsvåg. The amplitude and phase values in Table 4.3 differ from the model predictions of the K2 signal. This indicates that the origin is not OTL. This hypothesis was supported by analysis of tide gauge data from Honningsvåg. One year of data with a sampling interval of 1 h was analyzed similarly as the GPS height time series. No strong signal at 11.97 h was found in the tide gauge data. At Honningsvåg, multipath is a possible additional source at 11.97 h. Multipath may generate harmonic signals with diurnal and semidiurnal periods corresponding to the repeat cycle of the GPS satellites. Figure 4.6 shows that the GPS antenna is located near a small lighthouse with a conical metal roof that may act as a reflector of GPS signals.

In Vardø the 11.97 h peak is also significantly stronger than the model predictions. Here the signal is in phase with most of the OTL models. This suggests that the 11.97 h signal may represent the K2 OTL constituent.

Spurious signals shared by several stations can be generated if the reference station itself is exposed to multipath. We have not identified a spurious signal present in all periodograms. Still, a signal of period 12.39 h was found at four stations, i.e. Arjeplog, Andøya, Bodø, and Vardø. The amplitude of the signal was estimated to 1.8, 4.7, 1.5, and 3.2 mm, respectively. The presence of this signal at four stations relates it to the reference station in Kiruna.

Unmodeled ZTD may also generate spurious signals with diurnal or semidiurnal periods. A major shortcoming of GPS when used to observe OTL and other small vertical deformations is the strong correlation between the height change and the tropospheric path delay. The latter propagates with a factor of about four into the vertical component of the position estimates (Urschl *et al.*, 2005). Unmodeled ZTD may be the origin of the unexpected strong signal with period 23.93 h at Arjeplog corresponding to the K1 tidal constituent. Humphreys *et al.* (2005) argue that the Niell mapping function does not account for temperature-driven changes in the atmospheric scale height on time scales of less than one year. This results in diurnal errors in the ZTD estimates of similar order as the observed K1 signal at Arjeplog.

Finally, it should be noticed that unmodeled displacements due to Earth tides have the same temporal pattern as the OTL constituents and are another potential origin of spurious signals. However, Earth tides are spatially long wavelength phenomena and the effect of unmodeled Earth tide signals is reduced by using double differenced GPS observations. Thus, we do not consider unmodeled Earth tides as a likely source of spurious signals in this analysis.

Figure 4.6: The GPS antenna at Honningsvåg is placed close to the lighthouse with its characteristic sloping roof covered by plates of metal. Multipath signals from this roof are likely to be the origin of the strong signal with a period of 11.97 h found in the GPS height series.

4.5 Conclusion

One year long height time series from double differenced GPS observations for five coastal stations and one inland station have been analyzed. Periodograms and least squares analysis were used to detect periodic signals in the time series.

In summary, the analysis validated the M2 OTL signal at all stations, S2 at Andøya, Bodø, and Tromsø, and N2 at Bodø. At several stations, significant signals with periods corresponding to other constituents were also detected. The phase of these signals deviates however strongly from the model predictions. This indicates an origin different from OTL. Present signal to noise ratios of GPS observations have left several of the OTL constituents along the Norwegian coast not validated.

Comparison of the modeled and estimated signals indicates that FES95.2, NAO99b, and TPXO.7.1 are the best OTL models in this area. The established discrepancies are only of millimeter magnitude. The estimated discrepancies are too small to explain the harmonic signals found in Lysaker *et al.* (2008) between gravity observations and OTL models. Multiplied by the vertical gravity gradient of the Earth (0.3086 µgal mm^{-1}), a one millimeter error in the vertical displacement model results in a gravity change of only ∼0.3 µgal. This supports Lysaker

et al. (2008) who trust global OTL models for calculating the gravity change due to the vertical displacements.

Spurious signals were detected at several stations. Especially at Andøya, Honningsvåg, and Vardø the spurious signals are strong. At Honningsvåg multipath is suspected to be the origin of a signal with period 11.97 h. This observation illustrates the consequence of an inappropriate location of the GPS antenna when the observations are used for harmonic analysis.

Acknowledgements

The author is indebted to Bjørn Ragnvald Pettersen for discussions and comments which improved the manuscript considerably. Jon Glenn Gjevestad is acknowledged for assistance with the Bernese software and for useful suggestions. It is a pleasure to thank Lantmäteriet (The Swedish Mapping, Cadastre and Land Registration Authority) and Statens Kartverk (The Norwegian Mapping Authority) for access to GPS observations. Tide gauge observations from Honningsvåg were provided by The Norwegian Hydrological Service.

Chapter 5

Paper D: Absolute gravity values in Norway

Abstract. Absolute gravity observations yield insight into geophysical phenomena such as postglacial rebound, change in the Earth's hydrological cycle, sea level change, and changes in the Earth's cryosphere. In this paper, the first gravity values at 16 Norwegian stations measured by a modern absolute gravimeter of the FG5 type are presented. The gravity observations were corrected for Earth tides, varying atmospheric pressure, polar motion, and ocean tide loading. The ocean tide loading corrections were subject to special attention. A model based on locally observed ocean tides was applied at some of the stations. We estimated the total uncertainties of the gravity values to range from 3 to 4 µgal (1 µgal = 10^{-8} m s^{-2}). These errors are of magnitude one order less than previously presented absolute gravity values from Norway. The final gravity values are time tagged and will change due to postglacial rebound. The maximum effect is expected to be approximately -1 µgal yr^{-1}.

Accepted for publication in Norwegian Journal of Geography, 2009
Coauthored by J. G. Gjevestad, D. I. Lysaker, O. C. Dahl Omang, and B. R. Pettersen

5.1 Introduction

Gravity is a fundamental force of the Earth. From gravity observations, the figure and size of the Earth may be calculated. Gravity observations yield insight into geophysical phenomena, such as postglacial rebound (Larson and van Dam, 2000), changes in the Earth's hydrological cycle (Lambert *et al.*, 2006), sea level change (Sato *et al.*, 2001), and changes in the Earth's cryosphere (Luthcke *et al.*, 2008). Modern absolute gravimeters allow gravity to be observed at the microgal level (1 µgal = 10^{-8} m s^{-2}) by mobile instruments of the FG5 type (Niebauer *et al.*, 1995).

We present final absolute gravity values for 16 stations in Norway. The locations of the stations are given in Table 5.1 and are graphically shown in Fig. 5.1. Some stations have been observed more than once between 2005 and 2008. We have selected the best observation set for each station. The gravity values are time tagged and will change with time due to the ongoing postglacial rebound in the area. By adopting published GPS observed long-term height changes, we estimate the annual gravity change at each station. The ocean tides generate significant variability in gravity time series. The phenomenon is called ocean tide loading (OTL) and is a challenge to model at stations close to the coast due to the short distance to the attracting masses formed by the ocean tides. Hence, at some of the coastal stations, the gravitational effect of OTL was subject to special attention.

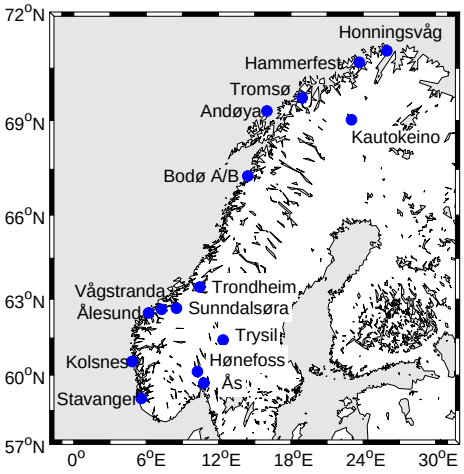

Figure 5.1: The gravity stations in Norway

Table 5.1: Station positions, number of observed sets, and sampling interval for the gravity stations. The heights are above sea level.

Station	Latitude	Longitude	Height	# sets	ΔT
Andøya	69° 16' 42.24" N	16° 00' 31.32" E	370 m	47	60 min
Bodø Asylhaugen	67° 17' 15.00" N	14° 26' 02.40" E	68 m	48	60 min
Bodø Bankgata	67° 16' 46.92" N	14° 23' 43.08" E	13 m	24	60 min
Hammerfest	70° 39' 42.48" N	23° 40' 32.16" E	17 m	42	30 min
Honningsvåg	70° 58' 37.92" N	25° 57' 53.64" E	20 m	144	30 min
Hønefoss	60° 08' 36.24" N	10° 14' 58.56" E	120 m	48	60 min
Kautokeino	69° 01' 19.56" N	23° 01' 10.20" E	388 m	36	60 min
Kolsnes	60° 33' 24.48" N	4° 49' 41.88" E	3 m	24	60 min
Stavanger-AA	59° 01' 03.00" N	5° 35' 53.88" E	55 m	24	60 min
Sunndalsøra	62° 39' 32.40" N	8° 30' 14.40" E	800 m	41	30 min
Tromsø	69° 39' 46.08" N	18° 56' 22.92" E	103 m	48	60 min
Trondheim-AA	63° 27' 18.36" N	10° 26' 44.52" E	30 m	48	60 min
Trysil	61° 25' 23.52" N	12° 22' 53.40" E	693 m	24	60 min
Vågstranda	62° 36' 45.36" N	7° 16' 29.28" E	38 m	34	30 min
Ålesund	62° 28' 34.32" N	6° 11' 54.60" E	140 m	96	30 min
Ås	59° 39' 56.16" N	10° 46' 40.80" E	95 m	48	60 min

The presented gravity values provide reference values for detailed gravity measurements such as, e.g., gravity measurements to estimate glacier mass balance (Breili and Rolstad, 2009). The network is useful for calibration and validation of ground based gravimeters and gravity satellites like GRACE and GOCE. In addition, the network is a reference for monitoring long term temporal changes in the gravity field of the Earth.

5.2 Field methods

The gravity observations were collected with the FG5-226 absolute gravimeter operated by the Norwegian University of Life Sciences. FG5-226 is a free fall instrument observing gravity with an accuracy of 1 to 3 µgal.

The final gravity values were calculated by averaging a time series obtained at each station. The time series consist of gravity measurements with a sampling interval of 30 or 60 minutes. Each of these measurements, called a set, is the average of 50 drops (free fall experiments). The number of sets and sampling interval for each gravity station are found in Table 5.1. The time series last between 21 hours and 3 days.

We used locally observed vertical gravity gradients in the equation of motion to calculate gravity from each drop. The gravity gradients were observed with a LaCoste & Romberg relative gravimeter (instrument G-761) by successively

Table 5.2: Observed gravity gradients (dg/dh) at the Norwegian gravity stations.

Station	dg/dh (µgal cm^{-1})
Andøya	-4.06
Bodø Asylhaugen	-3.30
Bodø Bankgata	-2.64
Hammerfest	-3.14
Honningsvåg	-3.52
Hønefoss	-2.90
Kautokeino	-3.08
Kolsnes	-2.80
Stavanger-AA	-2.80
Sunndalsøra	-2.52
Tromsø	-3.34
Trondheim-AA	-2.95
Trysil	-3.83
Vågstranda	-3.04
Ålesund	-2.92
Ås	-2.99

measuring the gravity difference between two positions separated by a known vertical distance. Typically, the gravity difference was measured 5 to 10 times over a vertical distance of 1.5 m. This yielded a precision of approximately ±0.05 µgal cm^{-1}. The gravity gradients are listed in Table 5.2.

5.3 Analysis

The raw gravity observations were processed with the g-software (version 6) provided by Micro-g Solutions Inc., the manufacturer of FG5-226. We used this software to correct the raw gravity observations for Earth tides, polar motion, and varying local atmospheric pressure.

The Earth tide corrections were calculated from the ETGTAB model, i.e. a tide generating potential from Tamura (1987) and Love numbers of the Wahr-Dehant-Defraigne model (Dehant *et al.*, 1999). Final polar motion coordinates provided by the International Earth Rotation and Reference Systems Service (IERS) were used to calculate the polar motion corrections.

For all stations except Hammerfest, the atmospheric pressure corrections were calculated from atmospheric pressure recorded by a barometer in the meteorological instrument package of the gravimeter. Due to instrument failure at Hammerfest, it was necessary to use pressure observations provided by the Norwegian

Meteorological Institute (MET). The observations from MET were reduced from the reference height of the weather station to the height of the gravimeter by utilizing the hydrostatic equation.

$$P = P_0 e^{-M\,g\,z/(R\cdot T)} \tag{5.1}$$

Here, P_0 and P are atmospheric pressure in hectopascals at the weather station and at the gravimeter, respectively, $M = 0.029$ kg mol^{-1} is the mean molecular weight of the mixture of gases constituting the atmosphere, $g = 9.80665$ m s^{-2} is the Earth's acceleration of gravity at 45° latitude (used all over the world in this standard atmospheric model), $R = 8.314$ J K^{-1}mol^{-1} is the universal gas constant, z is the height difference between the weather station and the gravimeter, and T is the air temperature in Kelvin (NASA, 1976). The barometric gravity corrections (b) were calculated by

$$b = A \cdot (P - P_n), \tag{5.2}$$

where $A = -0.3$ µgal hPa^{-1} is the barometric admittance factor, P is atmospheric pressure at the gravity station calculated from Eq. (5.1), and P_n is the nominal atmospheric pressure at the gravity station calculated by the g-software.

The OTL corrections were studied in more detail. Initially, OTL corrections were calculated from the two global models FES2004 (Lyard *et al.*, 2006) and NAO99b (Matsumoto *et al.*, 2000). These two models were selected because (Lysaker *et al.*, 2008) reported them to be the best global models at arctic gravity stations along the Norwegian coast. The two models were downloaded from the OTL service at `http://www.oso.chalmers.se/~loading/` (Scherneck and Bos, 2009). This service provides site-dependent amplitudes (A_k) and phases (ϕ_k) which represent constituents of the OTL signal. From these coefficients, the gravity change (Δg) due to OTL was calculated by Eq. (5.3).

$$\Delta g = \sum_{k=1}^{11} f_k A_k \cos(\chi_k(t) + u_k - \phi_k) \tag{5.3}$$

In Eq. (5.3), χ_k is the astronomical argument calculated by a subroutine provided by the IERS (`ftp://tai.bipm.org/iers/convupdt/chapter7`). Formulas for the nodal modulation phase and amplitude corrections (f_k, u_k) were found in Schüler (2001). Equation (5.3) is in accordance with the revised version of the IERS conventions (McCarthy and Petit, 2009).

At several stations, the global OTL models did not predict the gravity changes due to OTL sufficiently accurately. The misfit agrees with Lysaker *et al.* (2008) who presented an alternative procedure to model OTL. They calculated the Newtonian attraction from the local ocean tides by circular sectors with tidal height

equal to the ocean tides observed by a nearby tide gauge. By a global OTL model for displacement, the gravitational effect of the vertical displacement of the observation point due to OTL was calculated.

We adopted a similar procedure for the gravity laboratories with a tide gauge located within 10 km. The ocean tides within 10 km from the gravity station were modeled by a regular grid of resolution 100 m × 100 m. For each observing epoch, all grid points were assigned tidal height from the tide gauge. The tide gauge observations were provided by the Norwegian Hydrological Service and are related to mean sea level. Hence, the calculated OTL effect represents the deviation from the long time mean. The gravitational displacement component was calculated from one of the two global models FES2004 and NAO99b.

The different OTL models generate only sub microgal variability in the final gravity values. However, the model is of significant importance for the set scatter of the time series. For each station, we adopted the OTL model generating the lowest set scatter. Eight stations were processed with the local OTL model (Andøya, Bodø-Asylhaugen, Bodø-Bankgata, Hammerfest, Honningsvåg, Tromsø, Trondheim, and Ålesund). At these stations, the local model reduced the set scatter by up to 30 % compared to the best global model. Global models were used at Kolsnes, Sunndalsøra, Ås, Hønefoss, Vågstranda, and Stavanger. For the first five stations, global models were the only possibility due to lack of local tide gauge observations. At the inland stations Kautokeino and Trysil, the maximum predicted OTL effect is only 1.3 and 1.0 µgal, respectively. When the gravity time series from these two stations are corrected by global OTL models, additional noise is introduced. Hence, the lowest set scatter was obtained by processing the gravity time series without OTL corrections. Only the solutions with lowest set scatter are discussed further.

At stations with time series longer than one day, the effect of unmodeled semi-diurnal signals was further reduced by using observing intervals covering an integer multiple of 12 hours. Thus, these signals were averaged close to zero.

5.4 Results

The final gravity values, set scatters and uncertainties are presented in Table 5.3. The gravity values are referred to 1.20 m above the floor at the station. Gravity values reduced to the marker top can be calculated by using the local vertical gravity gradients found in Table 5.2.

5.5 Discussion

The set scatter of the gravity values varies between 0.9 and 3.2 µgal. A poorly modeled geophysical phenomenon like OTL increases the observed scatter consid-

Table 5.3: Central epochs as decimal year, observed final gravity values (g) in microgals (1 µgal $= 10^{-8}$ m s^{-2}), set scatters (σ), total uncertainties (ϵ), estimated annual gravity change rates ($\dot{g}$), and used OTL model for Norwegian gravity laboratories. The gravity values are referred to a height of 1.20 m above the marker on the floor of the gravity laboratory.

Station	**Epoch** (year)	$g \pm \sigma$ (µgal)	ϵ (µgal)	$\dot{g}$ (µgal yr^{-1})	**OTL model**
Andøya	2005.560	982532300 ± 1.7	3.4	-0.4	Local/FES2004
Bodø Asylhaugen	2007.106	982359939 ± 2.3	3.8	-0.5	Local/NAO99b
Bodø Bankgata	2005.554	982372234 ± 0.9	3.1	-0.5	Local/NAO99b
Hammerfest	2006.491	982615904 ± 2.6	3.9	-0.4	Local/NAO99b
Honningsvåg	2007.513	982660445 ± 3.2	4.4	-0.4	Local/FES2004
Hønefoss	2007.458	981900643 ± 2.8	4.1	-0.7	FES2004
Kautokeino	2008.527	982454529 ± 3.0	4.2	-0.8	No model
Kolsnes	2005.493	981972819 ± 0.9	3.1	-0.2	NAO99b
Stavanger-AA	2007.641	981832858 ± 1.8	3.5	-0.2	NAO99b
Sunndalsøra	2006.381	981896162 ± 1.6	3.4	-0.5	NAO99b
Tromsø	2009.532	982539909 ± 2.6	4.0	-0.5	Local/NAO99b
Trondheim-AA	2008.499	982145996 ± 2.6	4.0	-0.7	Local/NAO99b
Trysil	2008.391	981827002 ± 1.6	3.4	-1.0	No model
Vågstranda	2006.384	982074808 ± 1.8	3.5	-0.5	FES2004
Ålesund	2008.731	982063297 ± 2.7	4.1	-0.4	Local/FES2004
Ås	2007.610	981884415 ± 1.6	3.4	-0.6	NAO99b

erably. The magnitude of OTL varies along the Norwegian coast. At the stations Kolsnes and Stavanger, the effect is virtually void due to an amphidromic point (point where the ocean tides have zero amplitude) located in the North Sea. At these two stations the set scatter is a fair representation of the instrument's noise level. The OTL effect increases significantly northward from Stavanger and reaches more than 10 µgal at Andøya and Honningsvåg. Visual inspection of the residuals between the observations and the model reveals prominent semi-diurnal signals at these two stations. This is graphically illustrated for Honningsvåg in Fig. 5.2. The signal in the residuals is likely to have OTL as origin. The amplitudes of the semi-diurnal signal in the residuals at Andøya and Honningsvåg were estimated to 2.2 and 3.6 µgal, respectively. Hence, a considerable fraction of the set scatter at these two stations is generated by the remaining signal of OTL.

At other stations, no periodic signal is left in the gravity time series after correcting for OTL, e.g. the amplitude of the diurnal signal is reduced from 5.7 to 0.6 µgal at Ålesund after applying OTL corrections. Here, the rather high set scatter of 2.7 µgal may be generated by micro seismicity due to ocean waves. The gravity laboratory is located on a cliff only 200 m from the seashore.

These examples show that at some of the stations the set scatters in Table 5.3 do not only represent random noise in the gravity time series but also variation due to OTL.

Systematic errors of the instrument and field procedures are not included in

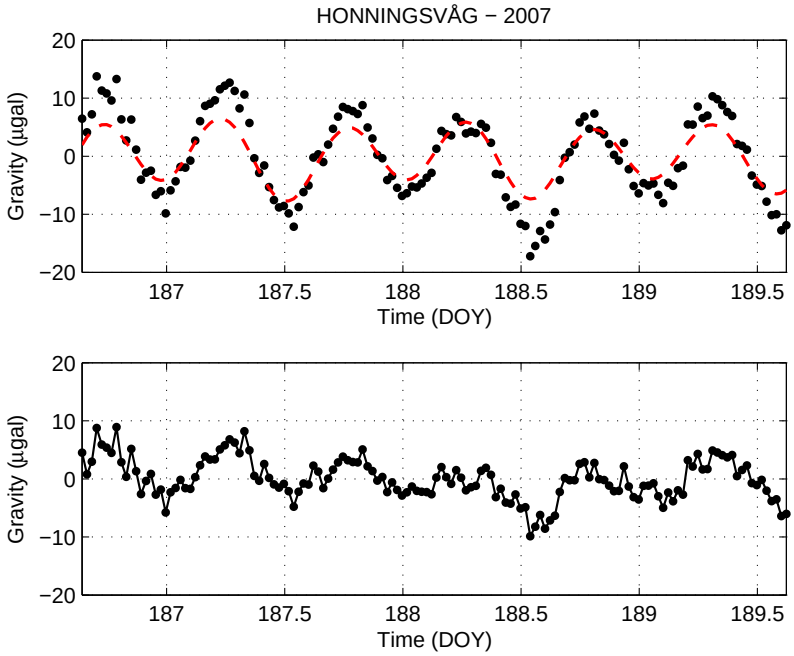

Figure 5.2: Upper panel: Gravity observations (filled circles) and the OTL model (dashed line) in Honningsvåg. The OTL model was calculated from local tide gauge observations combined with NAO99b. Lower panel: Residuals between observations and the OTL model. A significant semi-diurnal signal with an amplitude of 3.6 µgal is prominent in the time series of the residuals.

the calculated set scatters. The only way to calibrate an absolute gravimeter is by comparison with other similar instruments. This procedure will not reveal systematic errors that all instruments share. Comparisons of instruments used to observe gravity in Scandinavia, including FG5-226, show that all instruments agree within one standard deviation of 3 µgal. No systematic bias between the instruments was found, but occasional shifts may occur (Pettersen *et al.*, 2009). A similar result was obtained by comparison of 13 absolute gravimeters in Walferdange, Luxemburg, in 2003 which included observations by FG5, JILA-g, and A10 instruments. All instruments agreed within a standard deviation of less than 2 µgal (Francis and van Dam, 2006). They also investigated errors due to the operator, which was found to be less than 1 µgal. Thus, we adopt 3 µgal as an estimate of the size of systematic errors. The total uncertainty (ϵ) of the final gravity values were calculated by adding in quadrature 3 µgal to the set scatters

(σ) (see Table 5.3).

$$\epsilon = \sqrt{\sigma^2 + (3\ \mu\text{gal})^2} \tag{5.4}$$

Previously absolute gravity values for Norway are presented in e.g. Morelli *et al.* (1971). These gravity values were estimated by a common adjustment of absolute gravity measurements (older free fall instruments), pendulum measurements, and relative gravity measurements. In Norway, the resulting gravity measurements have errors between 16 and 40 µgal. Hence, the errors of the gravity values in Table 5.3 are of magnitude one order less.

The ongoing postglacial rebound in Fennoscandia changes the gravity values with time. The vertical deformations due to postglacial rebound reach almost 10 mm yr^{-1} around the Gulf of Bothnia and diminish towards the coast of Norway. From leveling, tide-gauges and continuous GPS, Vestøl (2006) estimated the apparent land up-lift rate in the study area to 0 - 5 mm yr^{-1}. Land up-lift with respect to the centre of the Earth is found by adding 1.5 mm yr^{-1} representing the sea level change over the last century (Cazenave and Nerem, 2004). With a proportionality constant of -0.15 µgal mm^{-1} between vertical crustal motion and gravity (Wahr *et al.*, 1995), we calculated annual gravity changes ($\dot{g}$) of -0.2 to -1.0 µgal yr^{-1} due to postglacial rebound in the study area (see Table 5.3). In addition, changes in the hydrological cycle of the Earth may generate temporal gravity changes of up to nearly 20 µgal (Breili and Pettersen, 2009).

5.6 Conclusion

Final gravity values for 16 Norwegian stations are presented in Table 5.3. This provides a framework for detailed gravity measurements, calibration purposes, and monitoring of long term temporal changes in the gravity field of the Earth. At each station, the best available method to correct the gravity time series for OTL was selected. We acknowledge the need for improved OTL models along the Norwegian coast. The errors of the presented gravity values were estimated to 3 - 4 µgal. These errors are of magnitude one order less compared to previously presented gravity values for the same area. Due to postglacial rebound at the gravity laboratories, the presented gravity values are expected to change by up to -1 µgal annually.

Acknowledgement

The authors thank the Norwegian Mapping Authority for access to their gravity laboratories and for in-kind contributions. The fieldwork was funded in part by the Research Council of Norway.

Chapter 6

Paper E: Effects of surface snow cover on gravimetric observations

Abstract. A three year long absolute gravity time series from Trysil, Norway, is presented. The series shows a significant seasonal pattern, i.e. high gravity values during the winter season and low during the summer. A hydrological model was developed. The model is based on direct observations of the local ground water, snow cover, and rainfall data. It successfully explains the seasonal pattern in the gravity time series and reduces the total variation in the time series by 64 %. The model shows that 58 % of the total variation is caused by the snow of which 90 % is generated by the snow cover within 200 m from the gravity laboratory.

Published in Journal of Geodynamics Vol. 48, 2009, pages 16-22

Coauthored by B. R. Pettersen

6.1 Introduction

The Earth's hydrological cycle causes temporal variations in the gravity field of the Earth. The gravity change arises because rainfall, drainage, evapotranspiration, and snow represent redistribution of masses and deformation of the Earth's crust due to the load of the masses. The contribution from continental water storages to gravity variations is one of the largest at seasonal time scales (Boy and Hinderer, 2006).

Superconducting gravimeters observe gravity with an accuracy of ∼0.1 µgal (1 µgal = 10^{-8} m s^{-2}) while absolute gravimeters have an accuracy of 1-3 µgal. This allows detection and monitoring of gravity changes due to hydrological phenomena at different spatial and temporal scales (Lambert *et al.*, 2006).

The gravitational effect of hydrology has been addressed by several authors, e.g. van Dam *et al.* (2001); Neumeyer *et al.* (2004); Crossley *et al.* (2005); Abe *et al.* (2006); Hokkanen *et al.* (2006); Boy and Hinderer (2006); Harnisch and Harnisch (2006); Hinderer *et al.* (2006); Imanishi *et al.* (2006); Neumeyer *et al.* (2006); van Camp *et al.* (2006); Meurers *et al.* (2007). They address time series from superconducting gravimeters (SG) in Europe, Japan, China, and Indonesia. The SGs are typically located at sites experiencing only modest winter conditions. At most sites, a significant annual signal (up to 5 µgal) is present in the time series. Strong correlation with hydrological models is established, but there exist also some anticorrelated stations, e.g. Vienna/Austria and Matsushiro/Japan (Neumeyer *et al.*, 2006).

There are also studies of gravity time series at cold-region locations where the ground is covered by snow in the winter season. Bower and Courtier (1998) analyzed four years of data from the SG located at the Canadian Absolute Gravity Site (CAGS) near Ottawa, Quebec. Evapotranspiration, snowmelt, and precipitation are the three components necessary to account for the residual gravity variation. For the snow cover, a model based on snow melting and temperature was utilized in preference of considering the load of the snow cover itself. At CAGS, the residual gravity was strongly correlated with local well readings only during the summer.

Boy and Hinderer (2006) argue that the snow is not correctly modeled in case of permanent ice regions in most hydrological models. This was confirmed by the work by Sato *et al.* (2006a) who compared a time series from the SG at Ny-Ålesund in the Arctic to global hydrological models, i.e. the Land Dynamics model (LaD) and data from the Japan Meteorological Agency (JMA). The JMA data are constrained by the actual snow observations in Ny-Ålesund, and the JMA data yield larger snow depth in Ny-Ålesund compared to the LaD model. This indicates that the snow close to the SG-station has a dominant effect which the

LaD model does not include. The errors in the LaD model were identified as the main reason for the differences between observations and hydrological predictions from the LaD model in the 2001-2002 interval. It was also demonstrated that the gravitational effect of the snow is much larger than the effect of soil moisture.

Also absolute gravimeters are used to observe gravity changes due to hydrology. Lambert *et al.* (2006) argue that absolute gravimeters can be used to calibrate annual soil moisture effects observed by GRACE.

In this study, we present a three year long gravity time series from Trysil, Norway. The gravity variability is almost 20 µgal. A significant seasonal pattern is prominent, i.e. high gravity values during the winter months and low during the summer. Trysil is located in a part of Norway experiencing winter conditions. The ground is typically covered by snow from November to May. The present analysis investigates the gravitational effect of the snow in particular. A hydrological model is developed. The model includes the Newtonian attraction from the local ground, the effect of rainfall, the Newtonian attraction from the local and regional snow cover, and the Earth's elastic response to the load of the snow. The gravitational effect of the components is modeled from direct observations of the ground water, rainfall data, and snow depth readings. The hydrological model quantifies the contributions from the different components of the model, and it is shown that a significant part of the variation in the absolute gravity time series is explained by taking the gravitational effect of the hydrology into account.

6.2 The absolute gravity observations

The gravity observations were made by the FG5-226 absolute gravimeter (Niebauer *et al.*, 1995) at Ørsjøsætra near Trysil, Norway ($\varphi = 61.423°$ N, $\lambda = 12.381°$ E, h = 695 m), see Fig. 6.1. The gravity laboratory is located at a small hill formed by metabasalt and surrounded by sandstone covered with moorland and forest on a lower level. The gravity laboratory is supplied with a permanent GPS receiver and wells which allow manual monitoring of the ground water level. Less than 1 km from the gravity laboratory, a weather station operated by the Norwegian Meteorological Institute (MET) is located. This station provides e.g. snow depth readings and rainfall data. A few small lakes are located within 10 km from the gravity laboratory. The largest one, Ørsjøen, covers an area of 0.5 km^2 and is located 2 km from the gravity laboratory. The pillar for gravity measurements is located at the ground level.

All raw gravity observations were processed by the g-software (Micro-g Solutions Inc.) provided by the instrument manufacturer. With this software, the gravity observations were corrected for Earth tides, varying local atmospheric pressure, pole tides, and ocean tide loading (OTL).

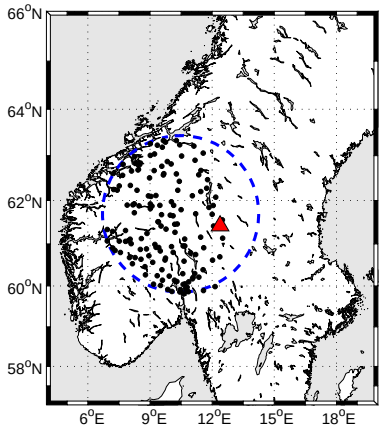

Figure 6.1: Map of southern part of Scandinavia. The gravity laboratory is indicated by a triangle and the dots indicate the weather stations. The dashed line is the border of the area covered by the regional snow loading model.

Due to Trysil's location ∼200 km from the coast, the gravity change resulting from OTL reaches only sub microgal magnitude. The g-software allows selection of several OTL models. The largest difference between various OTL-solutions was found for the short 6 h campaign at 21 April 2008. The Schwiderski solution differed by -0.49 µgal from the FES2004 solution. No OTL model stands out as better than others in Trysil. Hence, we chose the default model in the g-software, i.e. the Schwiderski model which includes the eleven main tidal waves (M2, S2, N2, K2, K1, O1, P1, Q1, Mf, Mm, and Ssa).

Final pole coordinates from the International Earth Rotation and Reference Systems Service (IERS) were used to calculate the pole tides. Throughout the period covered by the present analysis, the rubidium oscillator of the FG5-226 was frequently checked and calibrated by a GPS controlled rubidium atomic frequency standard.

Between August 2005 and August 2008, 26 observation campaigns of different length were accomplished. The gravity time series with error bars is graphically illustrated in Fig. 6.2 and the numerical values are listed in Table 6.1. It is seen that the weighted standard deviation (set scatter) of each campaign varies significantly throughout the time series. Increased noise levels are also prominent for each set (which consists of 50 drops) during these observation campaigns. The drop-to-drop scatter of a set may increase by a factor of five. In between the

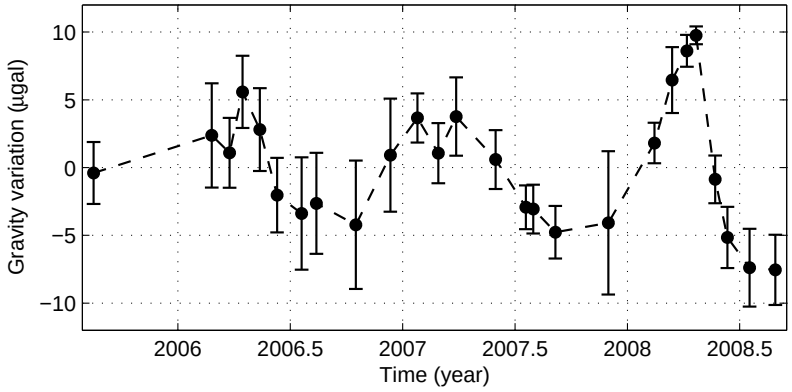

Figure 6.2: The gravity time series from Trysil. The error bars indicate the set scatter of each observation campaign.

observation campaigns in Trysil, the instrument was operated at other gravity laboratories. No other laboratory showed elevated noise levels as was episodically seen in Trysil. Hence, we argue that the increased noise levels were not due to the instrument. The origin is likely to be some sort of micro seismicity. However, the origin of the micro seismicity is at present unknown. For all observation campaigns, the instrument reference was oriented towards north.

Compared to superconducting gravimeters, data from the FG5 is not contaminated by drift problems. Shifts in absolute gravity time series may still occur due to replacement of mechanical parts of the instrument and deviating field procedures between different operators of the instrument. In addition, campaign-wise observations are episodic and suffer from lack of gravity information between the campaigns. This makes it challenging to capture unpredicted geophysical events.

6.3 Hydrological model

The local and regional hydrology were considered in order to explain the significant seasonal variations in the gravity observations of Fig. 6.2. Initially, the correlation between gravity observations and local well readings was investigated. The correlation coefficient was -0.16. Thus, the gravity observations appear virtually independent of the local ground water level. We found that the coefficient increased to 0.63 if only months without snow cover were considered. This indicates that the snow has a significant influence on the gravity observations. Hence, the hydrological model must include both the effects of ground water and snow cover.

Table 6.1: Observed absolute gravity (µgal), set scatter (µgal), sampling interval, and number of sets for the gravity campaigns in Trysil.

Epoch	**Number of sets**	**Sampling interval**	**Gravity**	**Set scatter**
20050816	57	60 min	981827001.87	2.28
20060224	392	30 min	981827004.64	3.84
20060325	86	60 min	981827003.36	2.58
20060415	26	60 min	981827007.85	2.66
20060513	61	60 min	981827005.08	3.05
20060610	64	60 min	981827000.23	2.75
20060720	24	60 min	981826998.88	4.14
20060813	24	60 min	981826999.63	3.73
20061016	17	60 min	981826997.90	4.74
20061211	25	60 min	981827003.18	4.17
20070124	41	60 min	981827005.93	1.81
20070227	24	60 min	981827003.33	2.22
20070328	24	60 min	981827006.03	2.89
20070531	25	60 min	981827002.86	2.17
20070719	18	60 min	981826999.34	1.61
20070731	35	30 min	981826999.19	1.80
20070905	24	60 min	981826997.50	1.94
20071130	72	30 min	981826998.17	5.29
20080213	25	60 min	981827004.08	1.49
20080313	24	60 min	981827008.72	2.43
20080406	40	30 min	981827010.88	1.18
20080421	6	60 min	981827012.02	0.66
20080522	25	60 min	981827001.43	1.76
20080611	24	60 min	981826997.06	2.26
20080717	24	30 min	981826994.88	2.87
20080828	25	60 min	981826994.45	2.59

The attraction from ground water and rainfall

The gravitational effect of hydrology is often modeled from precipitation measurements, soil moisture observations and geophysical modeling of the water flow in the ground (Hokkanen *et al.*, 2006). In Trysil, neither soil moisture observations nor a hydrogeological survey of the area exist. Hence, we followed an alternative and empirical approach based on the available direct observations of ground water level and rainfall data. The model to be determined has two terms, i.e. the attraction from the ground water (gw) and a rainfall model (rf).

Based on a Bouguer plate approximation, the gravitational effect of the varying ground water level was calculated by

$$gw_i = P \cdot 2\pi\, G\, \rho_{water}\, b_i, \tag{6.1}$$

where $G = 6.6742 \times 10^{-11}$ $\mathrm{m^3 kg^{-1} s^{-2}}$ is the Newtonian gravitational constant, $\rho_{water} = 1000$ kg $\mathrm{m^{-3}}$ is the density of water, P is the percentage porosity of the rocks in the ground beneath the gravity laboratory, and b_i is the thickness of the Bouguer plate at epoch i. b_i was calculated from Eq. (6.2) where wr_i is the well reading at epoch i and $\bar{wr}$ is the mean of all well readings in the interval covered by the gravity time series.

$$b_i = \bar{wr} - wr_i \tag{6.2}$$

With this formula, gw_i was assigned a negative sign when the distance down to the water table was longer than the average of all well readings. The local water table was manually measured in a 30 m deep well located only a few meters from the gravity platform. The mean distance down to the water table is ∼20 m. Throughout the observed period, the height of the water table changed by 3.36 m.

Rainfall data were provided as daily rainfall heights from MET. However, we do not have any information describing how the precipitation infiltrates the surrounding rocks and the layer of soil in the vicinity of the gravity laboratory. Still, we believe that the bedrock in the area adjacent to the gravity laboratory is covered by a rather thin layer of soil and the ground drains the rainfall water fast.

A connection between rainfall and gravity was established by a Bouguer plate approximation. For each gravity campaign, the thickness of the Bouguer plate was set equal to the average rainfall height r_i calculated for the days covered by the gravity campaign and one day in front of the campaign. In addition, an empirical coefficient C scaled the model. The model is similar to the precipitation model presented in Harnisch and Harnisch (2006).

$$rf_i = C \cdot 2\pi\, G\, \rho_{water}\, r_i \tag{6.3}$$

The rainfall model was only applied for gravity campaigns without any local snow cover. For observation campaigns with snow, the effect of rain is included in the snow model through the snow density. Equation (6.4) combines the two components gw and rf.

$$gh_i = gw_i + rf_i \tag{6.4}$$

The model was fitted to the gravity observations by least squares adjustment. To avoid biases from the snow cover, only gravity observations from epochs with local snow depth equal to zero as recorded by MET were used to search for the right porosity and the scaling coefficient. Best fit to the gravity observations was obtained for a porosity $P = 0.05$ and by scaling the rainfall model by $C = 0.59$.

The effect of the two components was studied by using the model to correct the gravity time series. We used the weighted root mean square (WRMS) defined in Eq. (6.5) to quantify the total variation in the ground water corrected and uncorrected time series. It includes both the variation due to systematic effects and random noise.

$$WRMS = \frac{n \cdot \sum_{i=1}^{n} \frac{1}{s_i^2} \left(g_i - \bar{g}\right)^2}{(n-1)) \sum_{i=1}^{n} \frac{1}{s_i^2}} \tag{6.5}$$

In Eq. (6.5), g_i is a corrected or uncorrected gravity observation, $\bar{g}$ is the mean of the gravity time series, and s_i is the set scatter of the gravity observation. If only ground water is considered, the WRMS is reduced by 22 %. The WRMS reduction increases to 52 % if also rainfall data is included into the model. Although the rainfall model is simple, it has a significant effect when the model is compared to the gravity observations.

The gravitational effect of soil moisture was not modeled separately. Due to the strong correlation between ground water level, precipitation, and soil moisture, the porosity and the scaling coefficient may also contain contribution from soil moisture variations caused by precipitation (Harnisch and Harnisch, 2006). This leads to a porosity coefficient likely to be estimated larger than the rock's actual porosity.

The modeled effects of the local ground water and the rainfall are graphically illustrated in Fig. 6.3. The gravitational effect of the ground water varies between -2 and 5 µgal and the effect of the rainfall reaches nearly 3 µgal. The maxima of the ground water model in Fig. 6.3, coincide with snow melting periods. This explains the maxima in spring 2006 and 2008, and in December 2007. A high in the ground water model was also expected in spring 2007, but no well reading captures this episode. The snow melting periods are also recognized in Fig. 6.5 which shows snow depth readings at Ørsjøsætra.

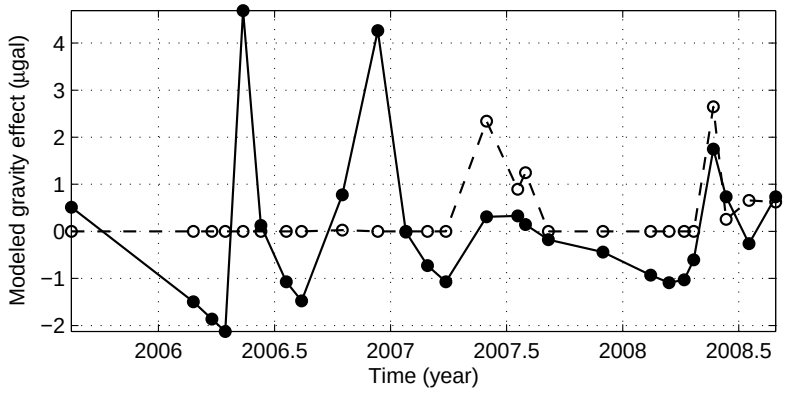

Figure 6.3: The modeled Newtonian attraction from the local ground water (filled circles) and the rainfall model (open circles).

Snow cover modeling

The gravitational effect of the snow cover was calculated in two steps. In step one the Newtonian attraction from the local snow cover is modeled, i.e. within 200 m. Step two takes regional effects in an area with radius 200 km into account, i.e. the attraction from the snow, and the Earth's elastic response due to the load of the snow.

Both models utilize snow depth readings from weather stations operated by MET and downloaded from `http://eklima.met.no`. The spatial locations of the weather stations are graphically illustrated in Fig. 6.1.

The density of the snow (ρ_j) was calculated for each observation epoch by

$$\rho_i = \frac{SWE_i}{SA_i} \tag{6.6}$$

Snow water equivalent data (SWE_i) and snow depth readings (SA_i) in Eq. (6.6) were provided by the Norwegian Water Resources and Energy Directorate (NVE). NVE calculates SWE for a 1 km × 1 km grid of Norway and with one day temporal resolution. The calculations are based on observations of temperature and precipitation (Engeset *et al.*, 2004). In this analysis, we used data from the cell containing the gravity laboratory in Trysil. Throughout the entire study area, the density of snow was assumed to be constant.

The mass of a prism of snow in the local or regional model was calculated by

$$m_{i,j} = \rho_i \, dx_j^2 \, SA_{i,j} \tag{6.7}$$

In Eq. (6.7), $m_{i,j}$ is the mass of prism j at epoch i, dx_j^2 is the area of the prism and

$SA_{i,j}$ is the snow depth of the prism provided by MET (for density calculations, snow depth readings were provided by NVE).

Attraction from local snow

The Newtonian attraction from the local snow cover was calculated by considering both the mass of the snow and the topography of the terrain in the vicinity of the gravity laboratory. A DTM with a spatial resolution of 1 m × 1 m covering the area within 200 m from the gravity laboratory was generated. The innermost zone covering 5 m × 5 m approximating the gravity laboratory was excluded from the model. If snow accumulates on the roof of the gravity laboratory, this effect has opposite sign to the overall snow effect. Due to lack of observations, this effect was not included in the snow cover model presented here. For each grid point, the height of the terrain was calculated by interpolating between GPS measurements in the area. The raw GPS measurements were processed using a kinematic precise point positioning strategy with the software Terrapos (Kjørsvik *et al.*, 2008). The interpolation was done with the Matlab routine *griddata*. Around each grid point, rectangular prisms were formed. The vertical component of the gravitational force ($sl_{i,j}$) from prism j at epoch i was calculated by

$$sl_{i,j} = G\frac{m_{i,j}}{l_j^3} \cdot (h_j - h_0), \tag{6.8}$$

where h_j is the height of the prism's center, h_0 is the height of the gravity laboratory, and l_j is the distance between the gravity laboratory and the center of the prism. Snow depth readings from a weather station located ∼1 km from the gravity laboratory were used. The total gravitational effect of the local snow was calculated by summing the effect from all prisms in the local model.

The Newtonian attraction from the local snow cover is graphically illustrated in Fig. 6.4. The gravity signal from the local snow cover generates a significant annual signal. It is seen that the effect of the local snow is largest throughout the winter 2008. At 13 March 2008, the maximum of 13.4 µgal was reached. For comparison, snow depth readings from Ørsjøsætra are shown in Fig. 6.5. The strong correlation between the local snow cover model and the local snow depth is prominent.

Regional snow loading

The regional gravitational effect of the snow cover was calculated by generating a second grid covering most of southern Norway and part of Sweden. The boundary of the study area was formed as a circle with centre at $\varphi = 61.643°$, $\lambda = 10.474°$ and radius of 200 km. The resolution of the grid was successively refined from 15 km × 15 km to 0.5 m × 0.5 m in the gravimeter's innermost zone.

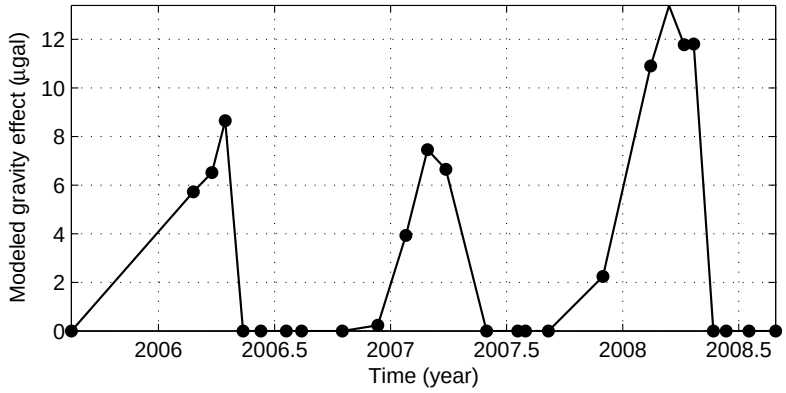

Figure 6.4: The modeled Newtonian attraction from the local snow cover.

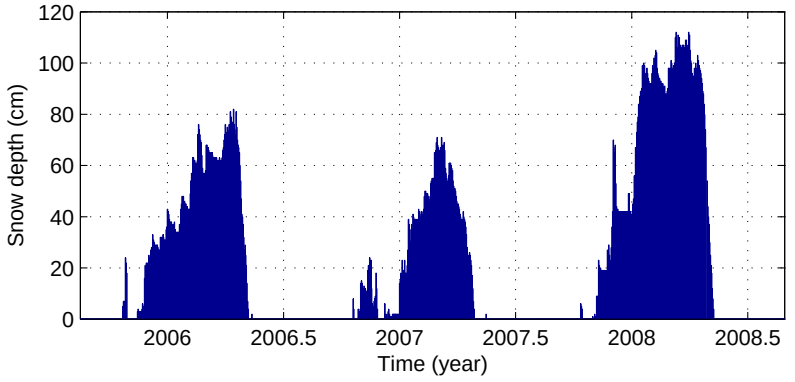

Figure 6.5: The snow depth observed at the weather station Ørsjøsætra, located approximately 1 km from the gravity laboratory.

The gravitational effect of the snow in each prism ($sr_{i,j}$) was calculated by convolving a Green's function for gravity with a snow model representing the mass of the snow within each prism.

$$sr_{i,j} = G(\psi_i)\, m_{i,j} \tag{6.9}$$

The Green's function $G(\psi_j)$ depends on the spherical distance ψ_j between the center of the prism and the gravity laboratory and yields the gravitational effect of a 1 kg load. The convolution in Eq. (6.9) involves a scaling with the prism's actual mass. A Green's function for the PREM Earth model (Dziewonski and Anderson, 1981) tabulated in Pagiatakis (1990) was adopted. The tabulated coefficients represent the elastic response of the Earth due to the load, i.e. the gravitational effect of the vertical displacement of the Earth's crust, and redistribution of masses inside the Earth due to the deformations. The Newtonian component of the Green's function ($G_N(\psi_j)$) was calculated in accordance with Farrell (1972)

$$G_N(\psi_j) = -\frac{G}{4R^2 \sin(\psi_j/2)}, \tag{6.10}$$

where $R = 6371 \times 10^3$ m is the Earth's radius. Notice that the Newtonian component was put equal to zero in the area represented by the local model.

Several weather stations are located within the study area of the regional model. Hence, for each grid point, the depth of the snow observed by the nearest weather station was adopted and used in Eq. (6.7) to calculate the mass of each prism. Finally, the total regional snow loading effect was calculated by summing the effect from all cells in the regional model. The regional snow loading model is illustrated in Fig. 6.6. It correlates well in time with the local snow model. The magnitude reaches nearly 1 µgal during the winter 2006 and 2007 and 1.2 µgal in the winter of 2008. This is about 10 % of the attraction from the local snow cover.

6.4 Discussion

We now compare the hydrological model to the gravity observations. First, the linear trend in the gravity time series was removed by

$$gc_i = g_i - \alpha \cdot (t_i - t_1), \tag{6.11}$$

where gc_i and g_i are corrected and uncorrected gravity values at epoch i, α is the annual gravity change, t_i is the epoch of gravity observation g_i, and t_1 is the epoch of the first gravity observation in the time series. There are several ways to estimate the trend. We chose to estimate it from the gravity time series corrected for hydrology. The trend was estimated by least squares adjustment to

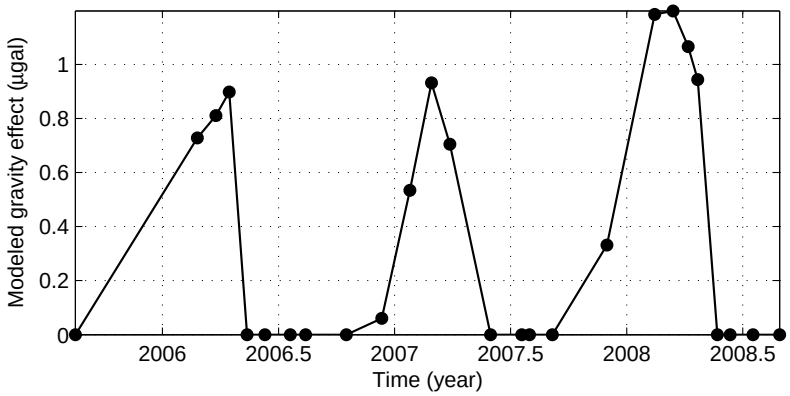

Figure 6.6: The modeled regional snow loading effect.

-1.90±0.4 µgal yr^{-1}. The origin of the trend is assumed to be mainly due to the ongoing post glacial rebound (PGR) in the area. However, the interval covered by the gravity observations is too short to obtain a reliable estimate of the annual gravity change due to PGR.

The trend corrected gravity time series and the hydrological model are compared in the upper panel of Fig. 6.7. The hydrological model successfully recreates the overall pattern of the gravity time series, i.e. high gravity values during the winter and low during the summer. This is also illustrated by the high correlation of 0.92 between the hydrological model and the PGR corrected gravity observations. The overall fit between the observations and the model was investigated further by using least squares adjustment to estimate a scale factor between the snow model and the gravity observations. Best fit to the gravity observations was obtained by scaling the hydrological model by a factor of 1.05 ± 0.08. This is not significantly different from unity, and indicates that the snow model does not systematically overestimate or underestimate the gravitational effect of the snow cover.

Also the range of the seasonal gravity changes is recreated by the model. The lower panel of Fig. 6.7 shows the residuals between the gravity time series and the hydrological model. The variation in the gravity and the residual time series was quantified by the WRMS to 6.3 µgal and 2.3 µgal, respectively. Hence, the total hydrological model reduces the weighted variation in the gravity time series by 64 %. The amplitude of the annual signal of the residuals was estimated to 2.5 µgal, compared to 7.2 µgal in the gravity time series. No annual signal is left in the residuals. We also calculated the WRMS reduction of the snow model alone.

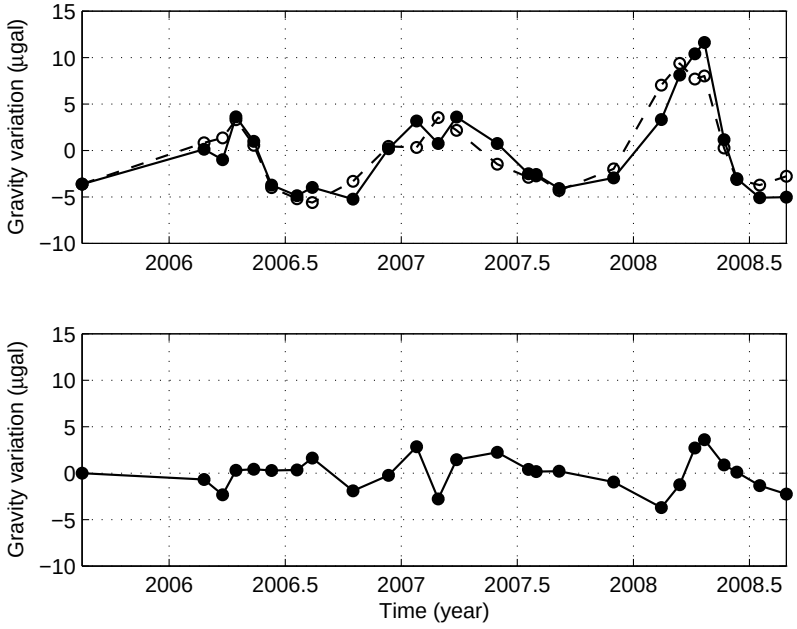

Figure 6.7: Upper panel: The gravity observations (filled circles) with all known corrections applied except hydrological ones, and the complete hydrological effect (open circles). Lower panel: Residuals of the gravity observations after applying hydrological corrections.

It was estimated to 58 %, i.e. the snow cover is the most important contributor to the variability in the gravity time series.

We also calculated the correlation between the gravity observations corrected for the gravitational effect of snow and the local ground water. The coefficient of correlation then improved from -0.16 to 0.67. This is close to the correlation of 0.63 calculated for months without snow only.

The local and regional snow loading models were analyzed to find the contribution from snow at different spatial distances from the gravity laboratory. The accumulated percentage contribution was calculated for different distances. This is graphically illustrated for the campaign with central epoch 13 March 2008 in Fig. 6.8. The chosen campaign is the one where Fig. 6.4 shows the largest gravitational effect. In general, gravimeters are not very sensitive to shallow-angle mass variations. This is also evident in Fig. 6.8. For the local model (left panel), the accumulated percentage contribution increases rapidly and flattens out towards

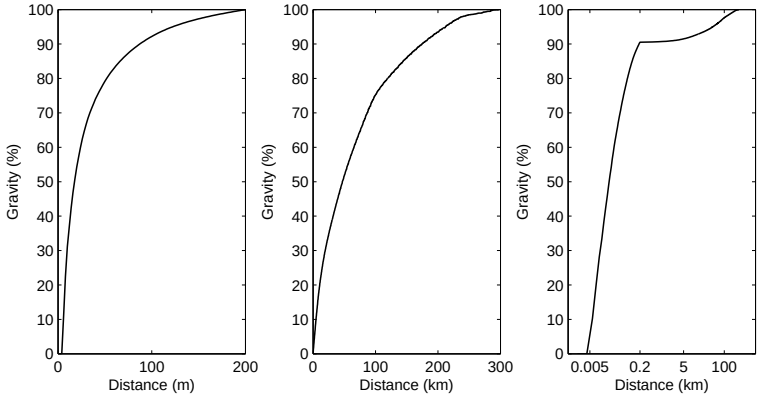

Figure 6.8: The figures illustrate the accumulated percentage contribution from the snow at increasing spatial distances from the gravimeter. The left, middle and right panels represent the local, regional, and the sum of the two models, respectively. Note the scale used on the distance-axis in the right most panel.

the outer limit of the local model. 90 % of the Newtonian attraction is due to the snow within 80 m from the gravity laboratory. For a gravity change of 10 µgal it is important to carefully model the attraction from the nearby snow. Figure 6.8 indicates that it is sufficient to restrict the local model to the innermost 200 m from the gravity laboratory.

The curve for the regional model in the middle panel of Fig. 6.8 rises more slowly and the flattening is less pronounced. This shows that the snow located far from the gravimeter also contributes to the elastic response of the Earth due to the snow load. The area of the regional model could well be extended. However, the magnitude of the regional snow loading model contributes only 1.2 µgal. If the model misses 10 % of the true effect, the effect of the omitted area is only ∼0.1 µgal. Hence, the extension of the regional model is appropriate at present measurement precision.

The right panel of Fig. 6.8 shows the combination of the local and regional model. More than 90 % of the total snow effect originates from the snow within 200 m from the gravity laboratory.

An improved hydrological model should focus on recreating the local effects as accurately as possible. This involves investigations of the soil moisture content and the infiltration of rainwater into the ground. More accurate snow cover modeling could be obtained by making the snow depth readings and density measurements close to the gravity laboratory. Also the gravitational effect of the snow on the roof

of the gravity laboratory should be included. This effect is of opposite sign to the overall snow effect and may reach several microgals (Virtanen, 2006). However, at Trysil the effect is difficult to quantify. Firstly, the snow depth at the roof was not observed and the depth is known to deviate significantly from the snow depth readings at the weather station. Additionally, the snow depth varies across the roof due to winds. Hence, we did not attempt to include this effect into the presented model.

An improved model should also consider the contribution from global effects. Boy and Hinderer (2006) conclude that the contribution to gravity variations from the continental water storage changes is one of the largest at seasonal timescales. For SGs in Europe, global hydrological models have an amplitude of less than one microgal. Global models are consequently of minor importance in Trysil, but still not negligible.

6.5 Concluding remarks

The present analysis demonstrates the capacity of modern absolute gravimeters in monitoring temporal gravity changes of the Earth. The hydrological model developed for Trysil explained 64 % of the weighted variation of the gravity time series and removed successfully most of the annual signal. In the present analysis, $\sim$90 % of this variation was caused by the local snow cover. Differences between the model and the observations might be due to inaccurate estimates of the snow density in the model. The model is most sensitive to density errors because this error propagates directly into the modeled gravity value.

Acknowledgement

The authors thank the Norwegian Mapping Authority for access to the gravity laboratory in Trysil and in-kind contributions. We also thank Reidar P. Bjørnstad for assistance at the gravity laboratory in Trysil. The Norwegian Water Resources and Energy Directorate and Hallgeir Elvehøy are gratefully acknowledged for providing water equivalent data. The free-access policy of the Norwegian Meteorological Institute for meteorological observations and climatological data is appreciated and acknowledged. The project was partly funded by the Research Council of Norway. The manuscript was substantially improved by comments from two anonymous reviewers.

Chapter 7

Paper F: Ground based gravimetry for measuring small spatial scale mass changes on glaciers

Abstract. Gravity change on a glacier surface is a composite of several effects, e.g. melting and accumulation of snow and ice, redistribution of mass with depth by refreezing of meltwater, and height and thickness changes of the snow and ice layers. Models and equations necessary to estimate the measured gravity change due to different effects are presented, and the propagation of observational errors is evaluated. The paper presents experiences with ground based gravity measurements carried out on Hardangerjøkulen, Norway, in spring and autumn 2007. It was found that the vertical gradient of gravity contributes most to the uncertainty in the determined mass change. With present instrumentation, the gravity can be measured with the required accuracy to determine the mass loss to ∼10 % of the loss determined by conventional mass balance measurements. Finally improvements in field procedures to achieve the required accuracy for measuring the mass/density changes directly combining gravity measurements and GNSS (Global Navigation Satellite Systems) are discussed.

Published in Annals of Glaciology Vol. 50, 2009, pages 141-147

Coauthored by C. Rolstad

7.1 Introduction

The gravity field at the Earth's surface is determined by its own internal distribution of mass, by the mass distribution at or near the surface and by other nearby masses such as the sun, moon and planets. The field is not static, but varies continuously with time because of the movement of these masses. The principal sources of gravity variation are tides, hydrology, land uplift/subsidence, ocean tide loading, atmospheric loading, and changes in the Earth's cryosphere.

It has been recently shown that mass changes of ice sheets with sufficiently large spatial coverage can be measured from satellites. The Gravity Recovery and Climate Experiment (GRACE) has measured gravity fields at latitudes above 60° providing monthly estimates of mass changes to accuracies of 10 mm in equivalent water thickness when averaged over discs of radius 600 to 700 km and larger (Velicogna and Wahr, 2006b). GRACE data has revealed a mass loss of $248 \pm 36\,\mathrm{km^3\,yr^{-1}}$ in the period 2002 to 2006 of the Greenland Ice sheet (Velicogna and Wahr, 2006a), which is equivalent to 0.5 ± 0.1 $\mathrm{mm\,yr^{-1}}$ increase in global sea level. GRACE data also show that in the period 2002 to 2005 the volume of the Antarctic ice sheet decreased by $152 \pm 80\,\mathrm{km^3\,yr^{-1}}$, equivalent to a $0.4 \pm 0.2\,\mathrm{mm\,yr^{-1}}$ contribution to global sea level (Velicogna and Wahr, 2006b). As discussed by Velicogna and Wahr, and also by Murray (2006), uncertainties in these results stem from tidal and non-tidal changes in the oceans, changes in the atmosphere, and from rebound of the Earth's mantle since the last ice age, where the latter contributes most to the uncertainty.

Ground based gravimeters operate at the surface of the Earth and are integrating sensors that observe the vertical component of Earth's gravitational acceleration. Today ground based gravimeters observe gravity with a repeatability of some microgals ($1\mu\mathrm{gal} = 10^{-8}\,\mathrm{m\,s^{-2}}$) and are widely used for geoid determination and observation of gravitational effects of geophysical phenomena such as post glacial rebound (Larson and van Dam, 2000), solid Earth tides (Baker and Bos, 2003), ocean tide loading (Lysaker *et al.* (2008), Dittfeld *et al.* (1997)), density anomalies in the Earth's lithosphere, and mass changes due to e.g. mining.

It is important to be aware of the conceptual differences between orbital and ground based gravimeters. First of all, the spatial resolution is different. The short distance to the attracting masses means that ground based gravimeters have a much finer spatial resolution compared to space born gravimeters such as GRACE, which observes the gravitational signal from a ground footprint with a radius of 500 to 700 km. This means that space born gravitational sensors are only suitable to observe mass changes from large glacier systems such as Antarctica and Greenland. For ground based gravimetry, the glacier's size makes no restrictions. In addition, ground based gravimeters are coupled to the Earth's surface and are

sensitive to both a change in gravitational potential and a height change of the instrument. In contrast, orbital gravimeters sense only changes in the Earth's gravitational potential.

Ground based gravimetry is not a well established method used to study glaciers, but some work exists. Klingele and Kahle (1977) used ground based gravimetry as a technique for determining the thickness of the ice cap of the Gorner glacier in Switzerland. In Fukuda *et al.* (2003) and Fukuda *et al.* (2007), ground based gravimetry is described as a method to detect the ice sheet thinning rate of the Shirase Glacier drainage basin in Antarctica with a view to calibration and validation of GRACE data. They focus mainly on fieldwork procedures and present preliminary results.

Ground based gravimetric measurements are sensitive to both changes in height, there is a strong gravitational gradient at the Earths surface, and to nearby changes in mass. As such it can be used as an alternative method to observe height changes on glaciers but also to observe mass changes which are not connected to height changes, such as changes in internal density due to the effect of refreezing of meltwater.

As already mentioned, Fukuda *et al.* (2003) proposed ground based gravimetry as a method to calibrate and validate satellite data from GRACE. Ground based gravimetry can also be useful for validation of data from GOCE (Gravity Field and Steady-State Ocean Circulation Explorer). GOCE is expected to be launched during 2008. The main goal of the mission is to observe gravity anomalies with an accuracy of 1 mgal at a spatial resolution of 70 km or better (Seeber, 2003). However, at present, GOCE is only expected to provide one or two gravity fields. In order to derive mass changes, a follow on gravity satellite mission is required.

The aim of this study is to evaluate the use of gravimetric measurements for determining the local mass balance of glaciers. As such we describe a simple gravitational model of a glacier and its surface mass balance and review the propagation of measurement errors through this model. To gain practical experience in carrying out the required gravimetric and field measurements in order to implement this model, a field experiment was carried out on Hardangerjøkulen in Norway during the spring and autumn of 2007. The results are compared to GNSS (Global Navigation Satellite Systems) measurements, carried out as part of the study, and to annual mass balance measurements made by the Norwegian Water Resources and Energy Directorate (NVE). The results are further discussed in relation to the estimated error, the practical application of the method and to future methodological and accuracy requirements for the use of gravimetric measurements to determine glacier mass balance. It is found that the gravitational measurements are dominated by the vertical gradient of gravity, rather than the

actual change in mass of the glacier.

7.2 Gravimetric methods and glacier model

The problem of determining mass changes from gravity observations is, in geodesy, a classical inverse problem, i.e. there exists an infinite number of mass distributions which make the same gravitational signal. The crux of the problem is that the gravitational attraction from a mass is determined by both the size of the mass and the distance to the mass, e.g. a small mass close to the observer makes the same gravitational attraction as a more distant larger mass. This makes it difficult to use gravity observations to distinguish between different sources of gravity change on a glacier. In order to distinguish the different gravitational sources, additional observations are necessary. In the model presented below, snow probe measurements are included to isolate the mass change of the snow pack. The need for solving the inverse problem for gravity observations is only relevant for ground based gravimetry close to the gravitational masses. From space, all glacial mass changes are of virtually the same distance.

In order to observe mass changes with a gravimeter, the gravity in a study point should be observed at least twice. It is the observed gravity *difference* which is related to mass changes, not the individual single gravity observations.

Basic gravitational modeling

A layer of ice or snow could be modeled as a circular cylinder with defined thickness, radius and density. The attraction of such a layer in a study point is found in e.g. Hofmann-Wellenhof and Moritz (2005). Simplified formulas are achieved by modeling the layer as a Bouguer plate which is a circular cylinder with infinite radius. For an observation point located on or above the Bouguer plate, the gravitational attraction is calculated by Eq. (7.1).

$$A_B = 2\pi\, G\, \rho\, b \tag{7.1}$$

Here $G = 6.6742 \cdot 10^{-11}\,\mathrm{m^3\,kg^{-1}\,s^{-2}}$ is the gravitational constant, ρ is the cylinder's density and b is the cylinder's thickness.

The attraction from masses located on the sides of the observation point attenuates quite quickly, which is why the Bouguer plate approximation can be readily applied. Figure 7.1 illustrates this, e.g. the contribution from the mass within 100 m makes 98 % of the attraction from a Bouguer plate with thickness 3 m. This illustrates two aspects. Firstly, the major part of observed gravity change can be attributed to local mass changes. Secondly, the use of a Bouguer plate and Eq. (7.1) in preference to a cylinder with a defined radius is a good approximation. A numerical example also illustrates this. The attraction at an

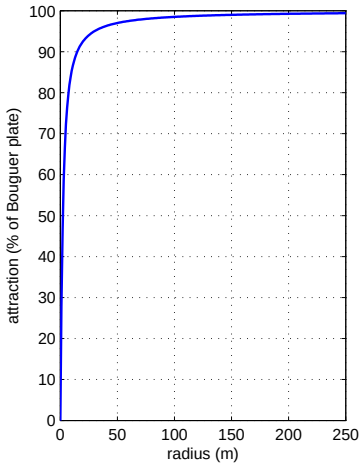

Figure 7.1: The relative error in using the Bouguer plate approximation as a function of cylinder radius. The major part of the attraction from a Bouguer plate is formed by masses close to the observation point, e.g. 98 % is formed by masses within 100 m from the observation point. A snow layer of density $600\,\mathrm{kg\,m^{-3}}$ and depth 3 m was assumed.

observational point localized 4 m above the ground of a cylinder with thickness 1 m, radius 200 m, and density $900\,\mathrm{kg\,m^{-3}}$ is 37.08 µgal. If we replace the cylinder with a Bouguer plate, Eq. (7.1) yields an attraction of 37.74 µgal. The error using approximate formulas is 1.8 % of the total gravitational effect. In the present analysis, we model the glacier with Bouguer plates and benefit from the simplified formulas.

Gravity changes on a glacier include the effect of any height change the instrument may experience. If the vertical gradient of gravity ($\partial g/\partial H$) and the height change (Δh) are known quantities, the gravitational effect ($\Delta g_{\mathrm{free\ air}}$) is found by Eq. (7.2).

$$\Delta g_{\mathrm{free\ air}} = \frac{\partial g}{\partial H}\Delta h \tag{7.2}$$

The gradient should be observed locally at the study site by successive measurements of gravity over a representative vertical distance of known length. Typical values are about $300\,\mathrm{\mu gal\,m^{-1}}$. In the present analysis, we use a sign convention that implies positive height changes corresponding to height reductions. Equation (7.2) means that gravity increases towards the Earth's center.

Modeling gravity change on a glacier

We model the glacier as a homogenous layer of ice with density ρ_{ice} covered by a homogenous top layer of snow with density ρ_{snow}. The model presented allows both layers to change between two periods of observation. By combining gravity observations and snow probe measurements, the presented model resolves both the total height change of the glacier surface and the isolated gravitational effect of a change in the thickness of the snow and ice.

Mass changes can be determined in two ways. Firstly, by multiplying the calculated height changes with the corresponding densities or, when an alternative measurement of the height change is available (e.g. GNSS), by the actual change in the gravitational mass.

The gravity change between two separate periods is the combined gravitational effect of accumulation/ablation of snow (Δg_{snow}) and ice (Δg_{ice}), and the height change of the observation point ($\Delta g_{\text{free air}}$).

$$\Delta g = g_{t2} - g_{t1} = \Delta g_{\text{free air}} + \Delta g_{\text{snow}} + \Delta g_{\text{ice}} \tag{7.3}$$

The effect of ($\Delta g_{\text{free air}}$) in Eq. (7.3) is estimated by Eq. (7.2). Gravity changes due to melted or accumulated snow and ice are determined by the two last terms.

$$\begin{aligned} \Delta g_{\text{snow}} &= -2\pi\, G\, \rho_{\text{snow}}(h_1 - h_2) \\ &= -2\pi\, G\, \rho_{\text{snow}} \Delta h_{\text{snow}} \end{aligned} \tag{7.4}$$

$$\begin{aligned} \Delta g_{\text{ice}} &= -2\pi\, G\, \rho_{\text{ice}} \Delta h_{\text{ice}} \\ &= -2\pi\, G\, \rho_{\text{ice}} (\Delta h - \Delta h_{snow}) \end{aligned} \tag{7.5}$$

Here Δh is the total height change of the observation point, and h_1 and h_2 are the snow layer's depth, found by snow probe measurements, at the first and the last observation, respectively. They are combined into Δh_{snow} which is the depth change of the snow layer. The change of the ice thickness is represented by Δh_{ice}. The minus signs are added because of the chosen sign convention, i.e. a positive height change implies ablation and a corresponding gravitational reduction. When all terms are combined, Eq. (7.3) can be used to solve the total height change of the glacier's surface:

$$\Delta h = \frac{\Delta g - 2\pi\, G\, \Delta h_{snow}(\rho_{\text{ice}} - \rho_{\text{snow}})}{\frac{\partial g}{\partial h} - 2\pi\, G\, \rho_{\text{ice}}} \tag{7.6}$$

The change in the ice thickness Δh_{ice} is found by subtracting the change in the snow layer's depth from the total height change using

$$\Delta h_{\text{ice}} = \Delta h - \Delta h_{\text{snow}} \tag{7.7}$$

The estimated height changes can then be used to determine mass changes per square meter if the snow and ice densities are known. Equation (7.8) to (7.10) give the mass changes due to accumulation/ablation of snow, ice and the total mass change, respectively.

$$\Delta m_{\text{snow}} = \Delta h_{\text{snow}} \cdot \rho_{\text{snow}} \tag{7.8}$$

$$\Delta m_{\text{ice}} = \Delta h_{\text{ice}} \cdot \rho_{\text{ice}} \tag{7.9}$$

$$\Delta m = \Delta h_{\text{snow}} \cdot \rho_{\text{snow}} + \Delta h_{\text{ice}} \cdot \rho_{\text{ice}} \tag{7.10}$$

The error propagation through the model is presented in Eq. (7.13) to (7.18) in the Appendix (of this chapter).

7.3 Fieldwork and results

Experience in operating a ground based gravimeter on a glacier was gathered during two field campaigns carried out at Hardangerjøkulen, Norway. Hardangerjøkulen is a mountainous glacier covering an area of 73 km^2. It is situated at 60° 32' N, 7°22' E and reaches an elevation of 1860 m above sea level, see Fig. 7.2. The winter mass balance was observed on the 3rd of May 2007 and the summer mass balance on the 3rd of October 2007. Both field campaigns involved gravimetry and snow probe measurements at a collocated study site in the glacier's accumulation area. GNSS observations were also carried out for the vertical positioning of the measurements, in order to validate and assess the results. Measurements were carried out at only one study point.

Gravity observations

The gravity observations were collected with a LaCoste & Romberg Model G relative gravimeter (instrument G-761). A relative gravimeter observes spatial or temporal gravity differences with respect to an arbitrary reference. In order to find absolute gravity differences from May to October, it was important to use the same reference for both campaigns. With the same reference, absolute gravity change between different periods was found by differencing the spatial gravity differences.

The gravity change from May to October at the glacier was determined as follows; at each site, the gravimeter was allowed to settle for some minutes before gravity was observed and recorded for about 15 minutes with a sampling interval of 10 seconds. The observations were corrected for Earth tides by the software provided by the instrument manufacturer. Final gravity differences of -21547 µgal and -20386 µgal between the reference and the study site were observed in May and October, respectively. The difference between these two spatial gravity differences gives an absolute gravity change of 1161 µgal at the study site from

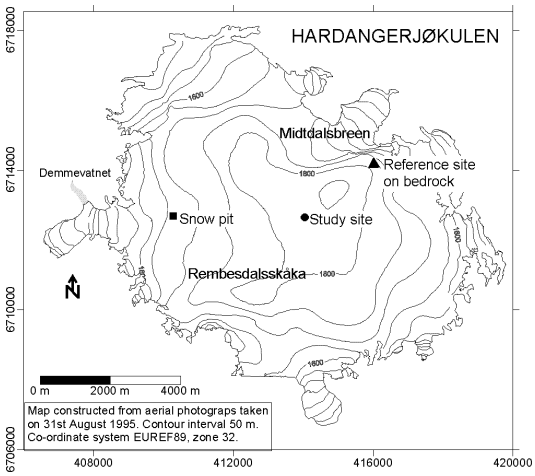

Figure 7.2: Map of Hardangerjøkulen with the study site, the reference site and the snow pit for density measurements.

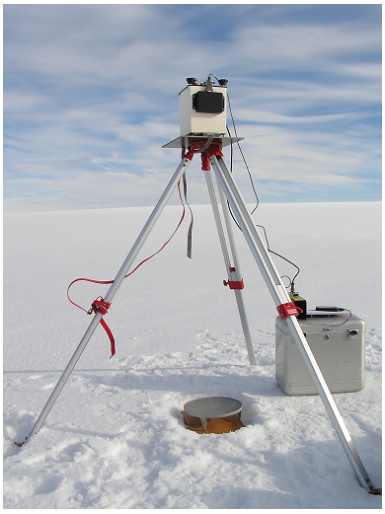

Figure 7.3: The picture shows the gravimeter in the upper position of a gravity gradient survey. For gravity gradient observations, the instrument is moved in turns between upper and lower positions on the baseplate at the glacier's surface. For mass change observations, the gravimeter is placed on its baseplate at the glacier's surface.

May to October. For the May observations only one gravity measurement was obtained on the glacier, for October two measurements were made. A handheld GPS receiver was used in October to relocate the horizontal position of the May measurements on the glacier.

Most spring gravimeters have a sensitivity of 1 µgal and an accuracy in the field which depends on the size of the gravity difference, weather conditions, field procedures, and the stability of the platform where the observations are done. Hazel (1989) has investigated the effect of noise, field procedures, and instrumental effects on LaCoste & Romberg gravimeters. Hazel quantifies the total error for one single gravity difference measurement to be at a maximum approximately 33 µgal and at a minimum approximately 10 µgal. The two gravity measurements on the glacier for October differ by 22 µgal. This is within the range suggested by Hazel, and we adopt it as the uncertainty of the gravity measurements of the present analysis.

The uncertainty of the absolute gravity change (dg) is found by calculating the square root of the sum of each individual gravity difference's squared error (dg_1 and dg_2).

$$dg = \sqrt{dg_1^2 + dg_2^2} \tag{7.11}$$

For our gravity measurements, this yields an absolute gravity difference with an error of 31 µgal. This error substituted into Eq. (7.13) results in an uncertainty of 0.11 m for the total/ice height change.

The vertical gradient of gravity

The vertical gradient of gravity was observed at the glacier study site in October only. The gravity change over a vertical distance of 1.20 m was observed five times successively and the gradient was found by dividing the gravity change with the distance. Mean vertical gravity gradient was calculated to be 312 ± 8 µgal m^{-1} and was, in the model calculations, assumed to be constant from May to October. The tripod was placed directly on snow. We experienced no problems with the tripod sinking into the snow during the measurements.

The uncertainty on the end result due to gravity gradient measurement errors depends on the total height change of the glacier surface. Equation (7.14) shows that the uncertainty may grow considerably for large height changes. Hence it is important to use accurate gradients. The gradient was observed with a standard deviation of 8 µgal m^{-1} under calm weather conditions. Substitution into Eq. (7.14) yields an uncertainty of 0.12 m.

Probing and density observations

Traditional probe observations were carried out. The depth of the snow pack in May was found to be 6.65 m. In October the snow pack was probed to be 4.05 m of which 0.75 m was formed by fresh snow.

The accuracy of the snow probe measurements is difficult to quantify. Each single reading is accurate to a few centimeters. Still, the depth of the snow pack may vary considerably over short distances. Here we estimate the error to be 0.20 m. From Eq. (7.15) this results in a total height change uncertainty of only 0.01 m. This is a very small error when determining the change in height and indicates how insensitive the gravitational model and measurements are to uncertainties in the actual change of mass. The probing error propagates directly to the estimated ice thickness change, i.e. by Eq. (7.16) a probing error of 0.20 m results in a ice thickness uncertainty of 0.19 m.

The mean density through the snow pack was measured in a snow pit marked on the map in Fig. 7.2. It was determined to be $540\,\mathrm{kg\,m^{-3}}$ and $580\,\mathrm{kg\,m^{-3}}$ in May an October, respectively. All density measurements were provided by NVE (H. Elvehøy, personal communication, 2007). Equation (7.6) includes only one term which represents the snow layer's density. The effects of depth dependent snow density or a density change between the observation periods are not included. Thus, the mean density of the two epochs was calculated to $560\,\mathrm{kg\,m^{-3}}$ and used in Eq. (7.6).

Equation (7.17) shows that the density error theoretically leads to a small height change uncertainty, e.g. a density error of $50\,\mathrm{kg\,m^{-3}}$ results in a height change uncertainty of 0.02 m for a height change of ∼3.00 m. The density of ice is easier to quantify. Usually a density of $917\,\mathrm{kg\,m^{-3}}$ is adopted and is assumed to be constant. In this analysis, we adopt an ice density error of $20\,\mathrm{kg\,m^{-3}}$ which results in a height change uncertainty of 0.002 m.

In principle it is possible to include more layers with different densities in the model. It is necessary to extract the thickness of each layer, e.g. from a snow core sample. For the measurements on Hardangerjøkulen, the effect of including more layers change the end result by only 5 to 10 cm and is consequently omitted from the calculations. Notice that it is of vital importance to use accurate densities when mass change is calculated from the height changes. In such calculations, the uncertainty of the mass change is proportional to the height change.

GNSS observations

GPS and GLONASS data were collected with a Topcon Legacy GNSS receiver. The raw GNSS observations were processed with TerraPos which represents a state-of-the-art solution to Precise Point Positioning (PPP) (Kjørsvik *et al.*, 2008).

Table 7.1: Summary of the observations

	May	**October**	**Change**
Ellipsoidal GNSS height	1874.39 m	1871.38 m	3.00 m
Gravity difference	-21547 µgal	-20397 µgal	1150 µgal
		-20375 µgal	1172 µgal
Depth of snow	6.65 m	4.05 m	2.60 m
Density snow	540 kg m^{-3}	580 kg m^{-3}	40 kg m^{-3}
Gradient	N/A	312 µgal m^{-1}	N/A
Fresh snow	0	0.75 m	0.75 m

Table 7.2: Measurement errors and their impact on the total change in height

Source of error	**Size of error**	dh	dh_{ice}
Gravity change	31 µgal	0.11 m	0.11 m
Gradient	8 µgal m^{-1}	0.12 m	0.12 m
Probing	0.20 m	0.01 m	0.19 m
Density snow	50 kg	0.02 m	0.02 m
Density ice	20 kg	0.002 m	0.002 m
Total error		0.22 m	0.29 m

Precise satellite ephemerides, satellite clock corrections and Earth orientation parameters were downloaded from Center for Orbit Determination in Europe (CODE). From the GNSS observations, the glacier surface was found to be lowered by 3.00 m during the summer. Unfortunately, because of instrumental failure, the duration of the GNSS campaign in October was limited to less than three hours. Hence it follows a considerable degradation of the height estimate's accuracy. Following Terratec (2007), the accuracy is expected to be about 0.20 m. Final gravity, GNSS, probes and density observations are tabulated in Table 7.1.

Calculated height change from May to October using the gravimetric measurements

Gravity observations, snow probing measurements, and the mean of the density observations were inserted into Eq. (7.6) to calculate the total height change at the observation point. The total height change was calculated to 4.10 m and the ice height change was found to be 1.50 m by Eq. (7.7). This differs significantly

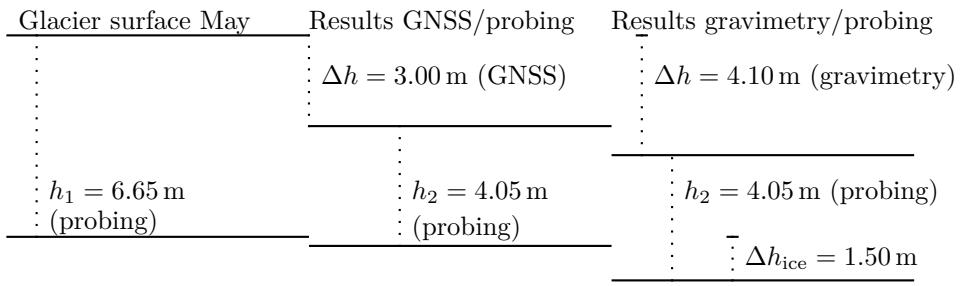

Figure 7.4: Schematic drawing of the results and the modeled upper part of the glacier. h_1 and h_2 are the depths of the snow layer measured in May and October, respectively. Δh_{GNSS} and Δh are the height change of the glacier's surface observed with GNSS and estimated from gravity observations. Δh_{ice} is the change in the ice layer's thickness.

from the GNSS height change measurements of 3.0 m. From Eq. (7.10), the corresponding total mass change was calculated to $2803\,\mathrm{kg\,m^{-2}}$ or 2.80 m in equivalent water thickness. The results are schematically illustrated in Fig. 7.4.

It is fair to assume that all estimated uncertainties in Table 7.2 are independent. Hence, the total uncertainty (dh_{total}) is the calculated square root of the sum of each individual squared uncertainty.

$$dh_{\mathrm{total}} = \sqrt{dh_g^2 + dh_\gamma^2 + dh_{h_{\mathrm{snow}}}^2 + dh_{\rho_{\mathrm{snow}}}^2 + dh_{\rho_{\mathrm{ice}}}^2} \tag{7.12}$$

For this analysis, the total uncertainty in the estimated change of height and ice thickness is found to be 0.22 m and 0.29 m, respectively. The contribution from each individual error is summarized in Table 7.2.

The total uncertainty depends on the size of the height change. Especially, for small height changes, the estimated ice thickness change is more sensitive to observational errors compared to the total height change. This is explained by the direct propagation of probing errors to the estimated ice thickness change.

7.4 Discussion

The uncertainty of the glacier's height change was estimated to 0.22 m. Compared to the height change calculated from conventional methods like probing and GNSS, the uncertainty forms ∼10 % of the total height change. This illustrates the potential accuracy of the presented methodology with present instrumentation. However, the total height change estimated from gravity observations differs by 1.10 m in comparison to the GNSS observations. Based on the error estimates,

the deviations are larger than expected. The deviation between the gravimetrically determined and the observed GNSS height change indicates the existence of gross errors in either the measurements or the assumptions used in the calculation. The most likely error of this type comes from the methodology employed in the field work.

Gravity was observed only once in May and is consequently not possible to verify. Gross errors may occur in gravity observations. During the May field work, repeated gravity observations between markers localized on bedrock revealed unprovoked jumps of more than 200 µgal. At present, we are not able to explain the origin of these jumps. This indicates the importance of carrying out field work in such a way that gross errors are detected when operating a spring gravimeter. Unfortunately, this general principle was not fulfilled during the May field campaign. Repetition of measurements, at both the glacier and the reference site, is a recommended methodology for future observational campaigns that will provide both verifiable measurements and uncertainty estimates.

It is important to ensure that gravity observations from different periods are carried out at the same horizontal position before mass changes are derived. This comes from ground based gravimeter's sensitivity to small scale gravity anomalies. The typical size of such anomalies on glaciers is at present a topic for further investigation. An alternative solution to this problem is found in Fukuda *et al.* (2007) who suggest observing gravity and GNSS positions in a grid covering an area of 40 m × 40 m. The grid observations are then used to predict, through interpolation, the gravity value of a virtual reference point. Accurate ties between the GNSS antenna phase center and the gravity observation platform should also be established with care.

A number of assumptions are made in the calculations that are also open to errors. The two most likely sources of error are the constancy of both the gravitational field at the reference point and the vertical gravitational gradient, which were assumed to experience no changes from May to August. It should be ensured that the reference point is connected to absolute gravity measurements.

In the present analysis, Eq. (7.6) was solved for the total height change. The estimated height changes were compared to GNSS height observations. It is possible to include the GNSS observations in the model and to solve for other parameters, e.g. the mean density of the snow layer. Still, it is necessary to include snow probing measurements to distinguish between depth changes of the snow pack and a change in the thickness of the ice. This approach was not tested in the present analysis due to the dominance of the vertical gravitational gradient in Eq. (7.3). With a 3 m vertical displacement of the glacier surface the contribution to the change of gravity due to the mass change is ∼7 % of the total,

or the equivalent of an estimated height change of ∼22 cm. This is close to the current estimated uncertainty which would have to be reduced significantly for any meaningful conclusions to be made concerning changes in density or pointing out the effect of superimposed ice. This could, to a large degree, be obtained if the 3D spatial location of the gravimetric measurements were coincident. This would demand, given the uncertainty in the gravitational gradient determined in this study, the positioning of the gravimeter to within a few centimeters of the previous measurement.

Traditional mass balance observations assume that all meltwater from the snow layer is completely removed from the glacier. The calculations made here do not take into account the possibility of superimposed ice. Superimposed ice is formed by refreezing of meltwater when the meltwater encounters a cold surface such as ice or firn (Wright *et al.*, 2005). This results in mass losses that are less than the apparent observed mass loss when using stakes. The model presented in the present paper includes a change in the ice volume height. Such height changes could be the combined result of firn transformed into ice, glacial dynamics, and superimposed ice. The problem of using a gravimeter to quantify one of these components is an inverse problem impossible to solve by gravimetry alone. On the other hand, prediction of gravity change due to superimposed ice is a direct problem. In this way, ground based gravimetry is a potential method to validate independent observations or models of superimposed ice and ice dynamics. This kind of analysis requires high quality gravity observations and careful modeling and observation of the accumulation and ablation of snow. For most glaciers, the change in gravity due to superimposed ice only represents a few microgals from one year to another. Ground based gravimetry, therefore, is likely to be most useful for studying long term mass changes due to the effect of superimposed ice.

Finally, further improvement in the uncertainty of the measurements is also obtainable by utilizing more precise gravimeters, e.g. a Scintrex CG-5 (SCINTREX Limited) or an A10 absolute gravimeter. These new generation gravimeters allow observations with a field repeatability of 5 to 10 µgal, improving the accuracy of the measurements by a factor of 5.

7.5 Conclusion

We have discussed ground based gravimetry as an alternative method to observe mass changes on glaciers. A model was established and error propagation was assessed.

It was shown that the presented methodology is capable to resolve the height change within ∼10 % of the total height change observed by conventional methods. However, practical tests at Hardangerjøkulen demonstrated that carrying out

gravitational measurements on a glacier is a challenging task. The height change of the glacier surface was measured to be 4.10 m which differs by 1.10 m from the GNSS measurements. This difference is larger than expected and indicates the existence of gross errors in the gravity observations that is most likely the result of procedural and methodological errors in the measurements. Improved accuracy in the results is expected to be obtained through improved fieldwork procedures. Most important is repeated observations to identify gross errors in the measurements.

The current application using gravimetric measurements provides, in essence, an alternative method for determining the change in height of the surface of the glacier. This does not realize the full potential of the methodology and is chiefly due to the dominance of the vertical gravitational gradient in the gravitational budget. By measuring the change in gravity at coincident heights, the effect of the vertical gradient can be eliminated and a more accurate assessment of the change in mass can be derived.

Though there are a number of uncertainties presented in the current study, experience gained through this work will lead to a significant improvement in the methodology used for future applications of gravimetric measurements. The recommended improvements in methodology should, in combination with improved instrumentation, make it possible to realize the potential of ground based gravimetry for observing mass changes on glaciers.

Acknowledgements

The authors would like to thank NVE and Hallgeir Elvehøy for access to density and probing measurements and the map of Hardangerjøkulen. Statkraft is acknowledged for letting us take part in their fieldwork campaign in October 2007. It is a great pleasure to thank Dagny I. Lysaker and John Hulth for taking part in the May fieldwork campaign. The manuscript was substantially improved by comments from two anonymous reviewers.

Appendix: Error propagation

Formulas for calculating the *height change* uncertainties are listed below. They are all found by studying the absolute value of Eq. (7.6) and (7.7) differentiated with respect to the variable to be studied. All errors, except the snow probe measurement error, propagate with equal size to the estimated total height change and the ice thickness change. Hence, two equations are presented for the snow probe measurement error. Equation (7.15) should be used to calculate the uncertainty of the total height change and Eq. (7.16) (marked with an asterisk) for the uncertainty of the ice thickness change.

The *mass change* uncertainties due to gravity, gradient, and probing measurement errors are found by multiplying the height uncertainties with the densities. When it comes to the mass change uncertainty due to density measurements errors, the procedure is different. The uncertainties are found by multiplying the density error with the height change. Here, the second order effect resulting from height change uncertainties due to density errors is neglected.

In Eq. (7.13) to (7.18), dg, $d\gamma$, dh_{snow}, $d\rho_{\text{snow}}$ and $d\rho_{\text{ice}}$ are gravity error, gradient error, probing error, snow density error and ice density error, respectively. The corresponding uncertainties in the observed height change is denoted by dh_x where x represents the error.

- Gravity measurement error dg:

$$dh_{\text{g}} = \frac{dg}{\frac{\partial g}{\partial h} - 2\pi\, G\, \rho_{\text{ice}}} \tag{7.13}$$

- Gravity gradient measurement error $d\gamma$:

$$dh_{\gamma} = \left[\frac{\Delta g - 2\pi\, G\, \Delta h_{\text{snow}}(\rho_{\text{ice}} - \rho_{\text{snow}})}{(\frac{\partial g}{\partial h} - 2\pi\, G\, \rho_{\text{ice}})^2} \right] d\gamma \tag{7.14}$$

- Snow probe measurement error dh_{snow} and the corresponding uncertainty on the estimated total height change ($dh_{h_{\text{snow}}}$):

$$dh_{h_{\text{snow}}} = \left[-\frac{2\pi\, G(\rho_{\text{ice}} - \rho_{\text{snow}})}{\frac{\partial g}{\partial h} - 2\,\pi\, G\, \rho_{\text{ice}}} \right] dh_{\text{snow}} \tag{7.15}$$

- Snow probe measurement error dh_{snow} and the corresponding uncertainty on the estimated ice height change ($dh^*_{h_{\text{snow}}}$):

$$dh^*_{h_{\text{snow}}} = dh_{h_{\text{snow}}} + dh_{\text{snow}} \tag{7.16}$$

- Snow density measurement error $d\rho_{\text{snow}}$:

$$dh_{\rho_{\text{snow}}} = \left[\frac{2\pi\, G \Delta h_{\text{snow}}}{\frac{\partial g}{\partial h} - 2\pi\, G\, \rho_{\text{ice}}} \right] d\rho_{\text{snow}} \tag{7.17}$$

- Ice density measurement error:

$$dh_{\rho_{\text{ice}}} = \left[\frac{2\,\pi\, G \left(\Delta g - \Delta h_{\text{snow}} \cdot \frac{\partial g}{\partial h} \right)}{\left(\frac{\partial g}{\partial h} - 2\pi\, G\, \rho_{\text{ice}} \right)^2} \right] d\rho_{\text{ice}} \tag{7.18}$$

Appendix A

Gravimeters and gravity observations

In geodesy, the acceleration of a free falling object leads to knowledge of the Earth system. The acceleration results from a fundamental force of nature - gravity. From gravity, it is possible to calculate the figure and size of the Earth. The gravity field of the Earth varies dynamically with time due to geophysical processes. Some processes are periodic, such as the Earth tides and ocean tide loading. Others have a quasi periodic pattern, e.g. the gravity signal due to the seasonal cycle of hydrology. In addition, secular changes occur from post glacial rebound, melting glaciers, and sea level change. Table A.1 provides an overview of some sources of gravity change. It is seen that several processes generate signals of magnitude 1 to 10 µgal. Consequently, the gravity observations must be correspondingly accurate.

During the last 50 years, ground based gravimeters have evolved into high precision instruments. Modern instruments measure absolute gravity with an accuracy of 1 to 2 µgal and detect temporal gravity differences of 0.1 µgal. This is sufficient to observe most of the phenomena listed in Table A.1. Lately, the introduction of space born gravimeters like CHAMP (Reigber *et al.*, 1999), GRACE (Tapley *et al.*, 2004) and GOCE (Johannessen *et al.*, 2003) has made it possible to observe gravity and gravity changes at regional and global scales. Hence, gravimeters are today important tools for monitoring global change, see e.g. Luthcke *et al.* (2008); Velicogna and Wahr (2006a).

The SI unit of gravitation and gravity is m s^{-2}. The unit *gal*, after Galileo Galilei, is often used in geodesy. A gravity change of one gal is a large quantity. Hence, the milligal (mgal) and microgal (µgal) are introduced as appropriate units.

$$1\,\text{gal} = 10^{-2}\,\text{m s}^{-2}$$
$$1\,\text{mgal} = 10^{-5}\,\text{m s}^{-2}$$
$$1\,\text{µgal} = 10^{-8}\,\text{m s}^{-2}$$

Spring gravimeters

The principle of spring gravimeters is to counterbalance the torque from gravity by a torque exerted by a spring system. A gravimeter with a linear and vertical

Table A.1: The magnitude of some gravitational signals. The values are collected from investigations in the present thesis, from Wenzel (1997), and Haagmans *et al.* (2006).

10 m s^{-2}	Gravitation of the Earth
10^{-2} m s^{-2}	The Earth flattening and rotation
10^{-3} m s^{-2}	Mountains and ocean trenches
10^{-4} m s^{-2}	Internal mass distribution of the Earth
10^{-5} m s^{-2}	Large reservoirs
	Gravity anomalies due to e.g. a salt dome
10^{-6} m s^{-2}	Tidal acceleration from the Sun and the Moon
	Distant Earthquakes
10^{-7} m s^{-2}	Changes in the Earth cryosphere
	Hydrological changes
	Ocean tide loading at coastal stations
10^{-8} m s^{-2}	Ocean tide loading far from the coast
	Nearby large buildings
	Annual post glacial rebound
	Polar tides
	Atmospheric loading
10^{-11} - 10^{-20} m s^{-2}	Tidal accelerations from the planets on the Earth

spring system utilizes Hooke's law: *Strain is proportional to stress* (Cutnell and Johnson, 1997). For such spring systems, the force balance is

$$mg - k(l - l_0) = 0 \Rightarrow g = \frac{k(l - l_0)}{m}, \tag{A.1}$$

where m is the test-mass, k is the spring constant, and l and l_0 are the length of the strained and the unstrained spring, respectively. For a general spring system, like the one shown in the left part of Fig. A.1, the balance of torques is more complicated (Torge, 2001):

$$m\,g\,a\sin(\alpha + \delta) - k\,b\,d\frac{l - l_0}{l}\sin\alpha = 0 \tag{A.2}$$

The quantities in Eq. (A.2) are all identified in Fig. A.1. By arranging the spring similarly to left part of Fig. A.1, the sensitivity of the gravimeter can be increased by a factor of 2000 compared to a linear system (Torge, 2001). The increased sensitivity arises because the lever arm of the spring decreases when the test mass is displaced downwards as gravity increases. This is also seen in right part of Fig. A.1. The spring's angle of attack (angle a, b, and c) decreases for increasing gravity (g_a, g_b and g_c). For a given change in gravity, the test mass is displaced by a longer distance with this spring system compared to a linear spring system.

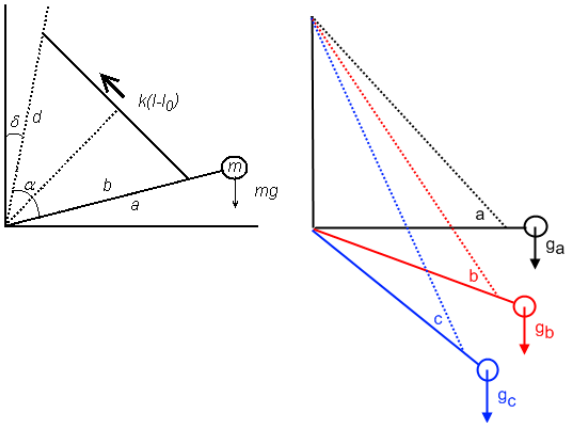

Figure A.1: General lever spring balance used in e.g. the LaCoste & Romberg spring gravimeter. To the right, it is shown how the lever arm of the spring decreases when the test mass is displaced downwards due to increased gravity.

This is the principle behind the widely used LaCoste & Romberg relative spring gravimeter shown in Fig. A.2.

Spring gravimeters are used to observe spatial and temporal gravity differences. In **paper F** it was discussed how absolute gravity change on a glacier is measured by repeated relative gravity measurements between a study point on the glacier and a reference point on bedrock which was assumed to experience only minor gravity changes.

Vertical gravity gradients are often observed by spring gravimeters. The gradients are observed by measuring the gravity difference between two positions vertically separated by a known distance. From the measurements, the gradient is estimated by dividing the gravity difference by the vertical distance. A numerical example from Ålesund, Norway, is shown in Table A.2. Normally, a standard deviation of $\sim$0.05 µgal cm^{-1} is obtainable by measuring the gravity difference 5 to 10 times. Figure A.3 shows a gradient survey on snow on the top of Hardangerjøkulen, Norway.

The vertical gravity gradient is used in the equation of motion to process absolute gravity observations. The absolute gravity observations in **paper A, B, D**, and **E** rely on gradients observed by a LaCoste & Romberg spring gravimeter. In **paper F**, the gradient of gravity was vital for calculating the effect of the height change of the glacier surface due to melting of snow. The gradient is also necessary to transfer a gravity value from the reference height of the absolute gravimeter

Figure A.2: LaCoste & Romberg relative spring gravimeter of the G-type with the ALIOD100 upgrade. (Photo: Kristian Breili)

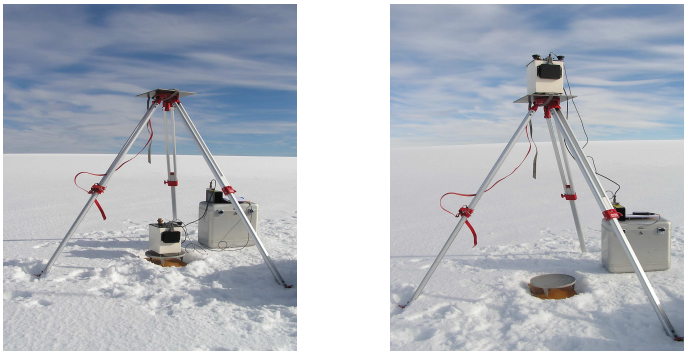

Figure A.3: Gravity gradient observations with a LaCoste & Romberg relative spring gravimeter on top of Hardangerjøkulen, Norway. Left panel: The gravimeter in its lower position. Right panel: The gravimeter in its upper position on top of the tripod. The vertical distance is measured between the upper and lower position. (Photo: Kristian Breili)

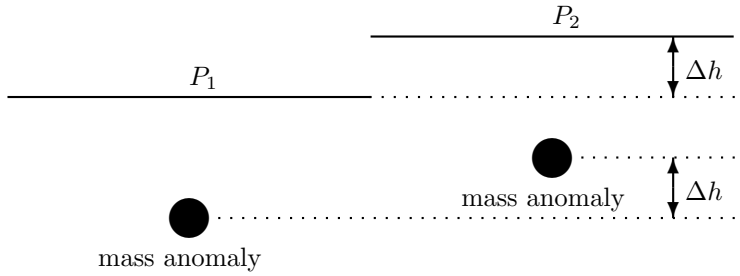

Figure A.4: Position P_1 is displaced by a vertical distance Δh to position P_2 due to e.g. OTL and Earth tides. Also the mass anomaly is displaced by a similar distance. In P_1, gravity is $g_1 = g_{E,1} + g_{MA,1}$, where $g_{E,1}$ and $g_{MA,1}$ are the gravity force from the Earth and the gravity force from the mass anomaly, respectively. In P_2 the gravity force is $g_2 = g_{E,2} + g_{MA,2}$. $g_{E,2}$ is the gravity force from the Earth in point P_2 and is calculated by $g_{E,2} = g_{E,1} + \frac{\partial g}{\partial h} \cdot \Delta h$ where $\frac{\partial g}{\partial h}$ is the normal gravity gradient of the Earth (-0.3086 µgal mm^{-1}). $g_{MA,2}$ is the gravity force due to the mass anomaly in position P_2. $g_{MA,2}$ equals $g_{MA,1}$ because the distance to the mass anomaly has not changed from position P_1 to P_2. The gravity difference from P_1 to P_2 is $\Delta g = g_2 - g_1 = \frac{\partial g}{\partial h} \cdot \Delta h$. Hence, the difference depends only on the normal gradient of gravity.

to another height, e.g. down to the height of the floor (see also Appendix B). On the other hand, the observed local gradient should not be used to calculate the gravitational effect due to vertical displacements resulting from e.g. OTL (cf. Eq. (1.11)), and Earth tides. For such height changes, the normal gradient (-0.3086 µgal mm^{-1}) is used because the local gradients are influenced by mass anomalies such as armored concrete, caves, and basements in the vicinity of the gravimeter. When the crust of the Earth deforms, the position of the gravimeter in the gravity field of the nearby mass anomaly does not change. This is illustrated in Fig. A.4

Free fall instruments

The principle of free fall instruments is to observe a body accelerating towards the Earth. From the observations, absolute gravity can be calculated by the equation of motion:

$$z(t) = z_0 + \dot{z}_0\, t + \frac{1}{2}\ddot{z}\, t^2 \tag{A.3}$$

In Eq. (A.3), $z(t)$ is the position of the falling body at epoch t, z_0 and $\dot{z}_0$ are the position and the velocity of the body at epoch $t = 0$, and $\ddot{z}$ is the acceleration of the body assumed to be constant with time. The acceleration $\ddot{z}$ of the body

Table A.2: Gravity gradient observations at Ålesund, Norway. The observations were collected with a LaCoste & Romberg relative gravimeter.

g (lower) (µgal)	**g(upper)** (µgal)	Δg (µgal)	Δh (cm)
6852	6437	-415	143.3
6845	6420	-425	143.5
6831	6415	-416	143.6
6833	6417	-416	143.6
6832	6419	-413	143.6
6831	6421	-410	143.6
Mean:		-416	143.5
$\Delta g/\Delta h$		-2.89 µgal cm^{-1}	
Standard deviation:		0.04 µgal cm^{-1}	

equals gravity.

$$\ddot{z} = \frac{d^2 z}{dt^2} = g \tag{A.4}$$

In general, z_0 and $\dot{z}_0$ are unknown quantities. With three distance-time observations, Eq. (A.3) can be solved for g (Torge, 2001).

$$g = 2\frac{(z_3 - z_1)(t_2 - t_1) - (z_2 - z_1)(t_3 - t_1)}{(t_3 - t_1)(t_2 - t_1)(t_3 - t_2)} \tag{A.5}$$

With more observations, Eq. (A.3) is solved by least squares adjustment.

In a non-homogeneous gravity-field, the gravity is not constant. If linearity is assumed, the gravity then follows Eq. (A.6).

$$\ddot{z} = g_0 + \frac{\partial g}{\partial z}(z - z_0) \tag{A.6}$$

Here $\partial g/\partial z$ is the vertical gradient of gravity, z is the distance from the reference height z_0, and g_0 is the gravity at the reference height. Equation (A.6) has the general solution

$$z(t) = z_0 + \frac{g_0}{\frac{\partial g}{\partial z}}\left[\cosh(\sqrt{\frac{\partial g}{\partial z}}t) - 1\right] + \frac{\dot{z}_0}{\sqrt{\frac{\partial g}{\partial z}}}\sinh(\sqrt{\frac{\partial g}{\partial z}}t). \tag{A.7}$$

The final free-fall equation for a non-homogenous gravity field is obtained by series expansion of $\sinh(\sqrt{\frac{\partial g}{\partial z}}t)$ and $\cosh(\sqrt{\frac{\partial g}{\partial z}}t)$ (see e.g. page 118 in Rottman (1995))

and elimination of higher order terms.

$$z(t) = z_0 + \dot{z}_0 \left(t + \frac{\partial g}{\partial z} \cdot \frac{t^3}{6} \right) + \frac{1}{2} g_0 \left(t^2 + \frac{\partial g}{\partial z} \cdot \frac{t^4}{12} \right)$$
$$= z_0 + \dot{z}_0 t + \frac{1}{2} g_0 t^2 + \frac{\partial g}{\partial z} \cdot \frac{\dot{z}_0 \, t^3}{6} + \frac{\partial g}{\partial z} \cdot \frac{g_0 \, t^4}{24} \tag{A.8}$$

Equation (A.8) has two more terms compared to Eq. (A.3), i.e. the gradient affects both the velocity and the acceleration terms. Time-distance pairs observed by a free fall instrument can be inserted into Eq. (A.8) and $\dot{z}_0$ and g_0 can be estimated by least squares adjustment.

The FG5 absolute gravimeter

The FG5 absolute gravimeter (Niebauer *et al.*, 1995) is a free fall instrument. It has an accuracy of 1 to 2 µgal and is a portable instrument. The FG5 has five main components, i.e. the dropping chamber, the interferometer, the superspring, the rubidium oscillator, and the system controller. The instrument is shown in the left part of Fig. A.5.

The free-fall experiments take place in the dropping chamber where the test mass is falling approximately 20 cm. For each drop, a cart brings the test mass to its initial position where the cart is triggered to accelerate downwards slightly faster than gravity. This brings the test mass into free fall. At the end of the drop, the cart decelerates and catches the test mass gently. It is important to eliminate or strongly reduce the air-drag on the test mass. Hence, the pressure inside the dropping chamber is reduced to 10^{-4} Pa $\approx 10^{-10}$ atm. In addition, the cart housing the test mass is designed as a drag-free chamber co-falling with the test mass. The relative velocity between the chamber and the test mass is close to zero.

The measuring system of the FG5 consists of a Mach-Zender in-line interferometer supplied with an iodine stabilized laser. The laser beam is guided to the interferometer by a fiber optics cable. In the interferometer the beam splits into a *reference beam* and a *test beam*. From the beam splitter, the test beam and the reference beam travel along different paths before they are reconstructed. The test beam is reflected up into the dropping chamber where it meets the test mass. The test mass is designed as a corner cube reflecting the test beam back through the interferometer, down to the superspring, and back to the interferometer for reconstruction with the reference beam. The path of the reference beam is simpler; it travels through the interferometer box directly to the photo detector where it is reconstructed with the test beam. See the right part of Fig. A.5 for a schematic drawing of the beam path. While the length of the path traveled by the reference beam is constant, the path of the test beam changes continuously through one

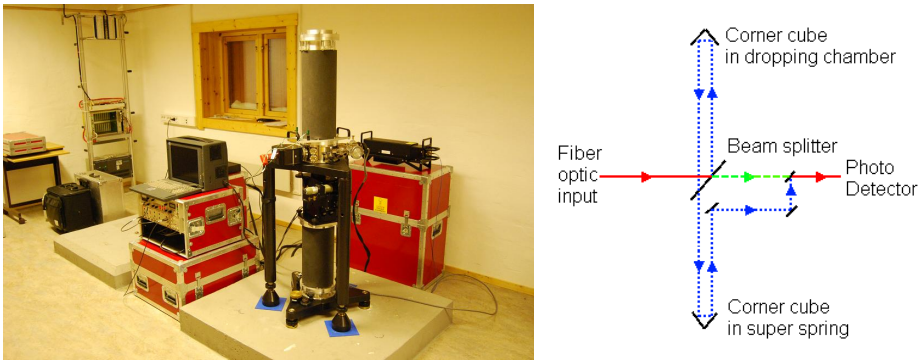

Figure A.5: Left panel: The FG5-226 absolute gravimeter (Photo: Kristian Breili). Right panel: Schematic drawing of the beam path/interferometer. The blue dotted line and the green dashed line represent the test beam and the reference beam, respectively.

drop due to the motion of the corner cube. This makes the test beam and the reference beam to produce fringes when the two beams are reconstructed. One single drop results in approximately 700000 fringes. The fringes are counted and timed by a rubidium oscillator creating time-distance pairs. Typically, 700 of the time-distance pairs are inserted into Eq. (A.8) to calculate gravity.

The superspring provides an inertial reference frame and compensates small vertical motions of the first beam splitter. By this the beam path is isolated from ground motions. The superspring is formed by a mainspring of length 20 cm controlled by an electronic feedback system. The resulting spring system has a natural period of 30-60 seconds, equivalent to a spring of length 200-900 m. A corner cube retroreflector is found at the end of the main spring. The retroreflector is the lower one illustrated in the right part of Fig. A.5.

The electronics of the FG5 includes a computer, the laser controller, the superspring controller, the drop controller, the power supply, and a 10 MHz rubidium oscillator. The computer is an ordinary PC supplied with a Time Interval Analyzer card. The computer is running the g-software which controls the observing procedure, visualizes and stores the gravity measurements, and processes the raw gravity observations into final gravity values.

The system controller, housing the drop controller and the superspring controller, is the link between the computer and the mechanical parts of the instrument. It also houses a meteorological package which includes a temperature sensor and an atmospheric pressure sensor observing the local barometric pressure. The meteorological observations are stored together with the gravity observations.

The pressure observations are used to calculate the gravitational effect of varying atmospheric pressure.

For real applications, gravity is determined from a large number of drops covering intervals of some hours to several days. Final gravity observations are obtained by correcting the raw gravity measurements for Earth tides, ocean tide loading, varying atmospheric pressure and polar motion. Scatter due to semi-diurnal signals are eliminated, or at least strongly reduced, by averaging gravity observations collected throughout an integer multiple of 12 h. Following this procedure, a gravity value with a corresponding standard deviation of 1-2 µgal is obtainable at appropriate locations.

Appendix B

Gravity corrections

The absolute gravity observations used in the present thesis were applied to a series of corrections. The corrections are necessary to obtain nominal gravity values. That means gravity values valid beyond the current observation epoch. In this section, the gravity corrections used by the g-software supplied with the FG5 instrument are discussed, i.e. corrections for varying atmospheric pressure (δg_{atm}), ocean tide loading (δg_{OTL}), Earth tides ($\delta g_{\text{Earth tide}}$), polar motion ($\delta g_{\text{pole}}$) and datum height ($\delta g_{\text{datum height}}$). The nominal gravity value (g) is obtained by adding the corrections to observed gravity (g_{obs}):

$$g = g_{\text{obs}} + \delta g_{\text{atm}} + \delta g_{\text{OTL}} + \delta g_{\text{pole}} + \delta g_{\text{Earth tide}} + \delta g_{\text{datum height}} \tag{B.1}$$

Figure B.2 and B.3 illustrate the effect of the atmospheric loading correction, the OTL correction, and the Earth tide correction at the inland station Trysil and at the coastal station Andøya, respectively.

Atmospheric pressure correction

The atmospheric pressure corrections were calculated from locally observed atmospheric pressure (P).

$$\delta g_{\text{atm}} = A \cdot (P - P_n) \tag{B.2}$$

In Eq. (B.2), A is the barometric admittance factor, and P_n is the nominal atmospheric pressure at the gravity station calculated by the g-software. Usually, the barometric admittance factor is set equal to $0.3\,\mu\text{gal hPa}^{-1}$. From panel B in Fig. B.2 and B.3 the atmospheric pressure correction appears as insignificant. However, this correction may be several microgals between different observation campaigns. This is illustrated in Fig. B.1 which shows the atmospheric pressure correction at Trysil throughout 2008. The time series was calculated by inserting atmospheric pressure observations provided by the Norwegian Meteorological Institute into Eq. (B.2). The time series ranges nearly 20 µgal. This clearly illustrates the importance of the atmospheric pressure correction when long time series of gravity are analyzed.

The method used by the g-software to calculate the atmospheric pressure correction relies on only locally observed atmospheric pressure. Refined methods

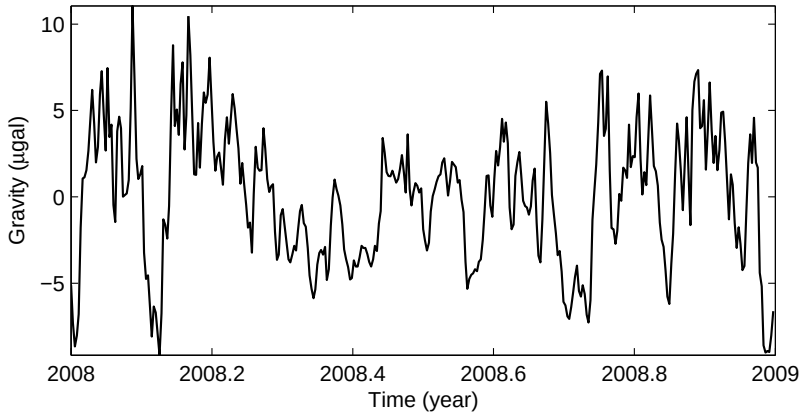

Figure B.1: The atmospheric pressure correction at Trysil in 2008. The time series was calculated by Eq. B.2. Barometric pressure observations were provided by the Norwegian Meteorological Institute.

take regional and global effects into account as well. This can be ensured by adding a term in Eq. (B.2) which includes the difference between local pressure change and the average pressure variation within a larger region (van Dam and Wahr, 1987). Another method is to convolve an atmospheric load model with a Green's function (Boy *et al.*, 2002; Neumeyer *et al.*, 2004), cf. Sect. 1.2.

Ocean tide loading correction

The ocean tide loading corrections were calculated from site specific amplitudes and phases provided by the g-software. The g-software uses the method of Farrell (1972) to calculate the coefficients, i.e. a global ocean tide model is convolved by a Green's function. For gravity stations close to the coast, the amplitude of the OTL signal may reach a magnitude of more than ten microgals. Consequently, the OTL corrections are especially vital in coastal regions. Panel C of Fig. B.2 and B.3 illustrates the OTL difference between an inland and a coastal station.

Earth tide correction

The Earth tide correction is the largest of the corrections applied by the g-software. For the gravity time series in panel D of Fig. B.2 and B.3, the Earth tide signal ranges 160 µgal and 100 µgal, respectively. For the presented gravity observations, the ETGTAB model was used. The ETGTAB model combines the tidal potential of Tamura (1987) with an Earth model of Dehant *et al.* (1999).

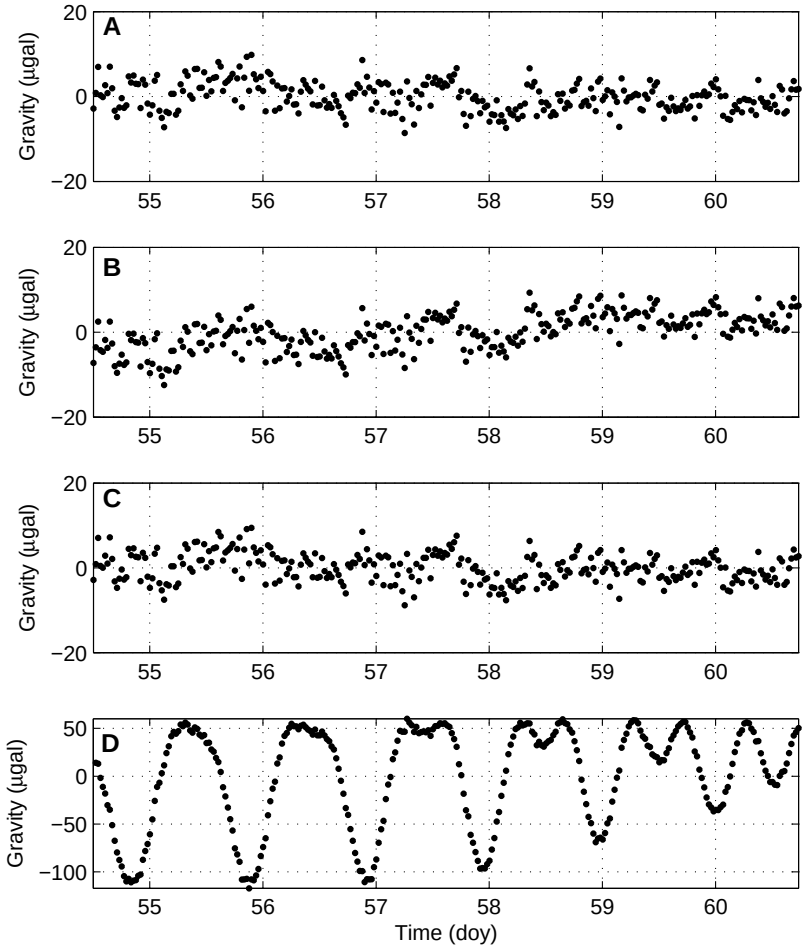

Figure B.2: Panel A: Gravity time series from Trysil, Norway, 240 km from the coast. The raw gravity observations are corrected for varying atmospheric pressure, ocean tide loading and Earth tides. Panel B: Similar to A, but the series is not corrected for varying atmospheric pressure. Panel C: Similar to A, but the series is not corrected for ocean tide loading. Panel D: Similar to A, but the series is not corrected for Earth tides.

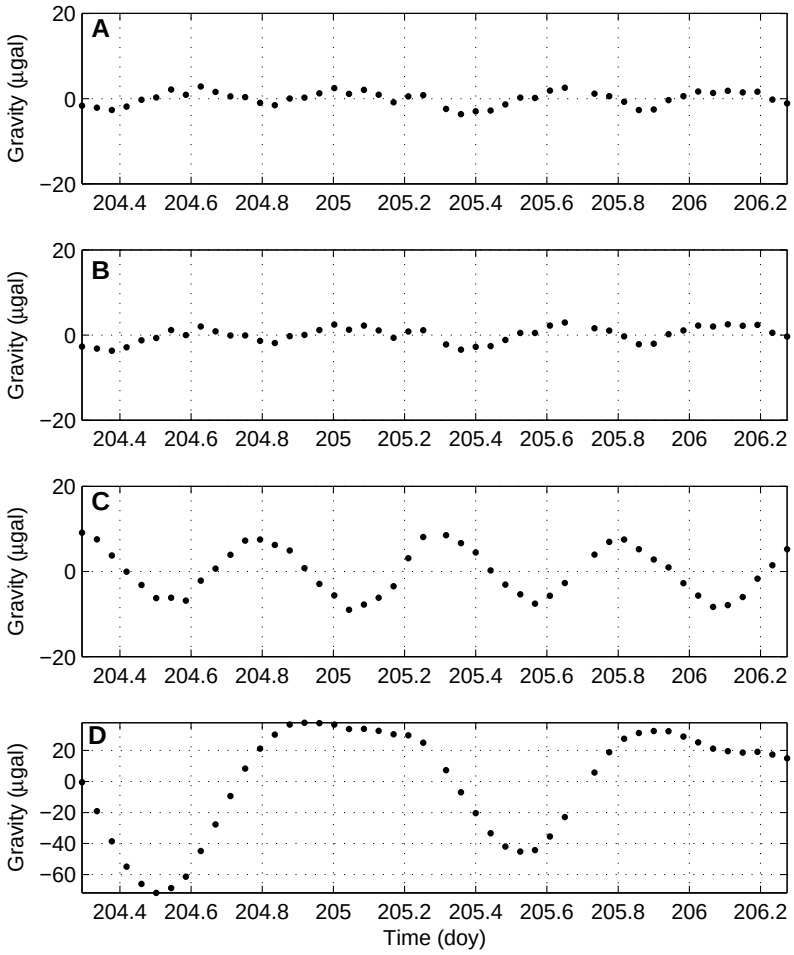

Figure B.3: Similar to Fig. B.2, but for the coastal station Andøya, Norway, located 1.3 km from the sea.

Polar motion correction

The gravitational effect of polar motion is a change in the centrifugal potential of the Earth. It results from changes in the distance between the observation point and the rotational axis of the Earth due to polar motion. The polar motion corrections can be calculated by

$$\delta g_{\text{polar}} = -\delta_{\text{pole}} \omega^2 R \sin 2\varphi (x_p \cos\lambda - y_p \sin\lambda), \tag{B.3}$$

where λ and φ are geodetic longitude (east of Greenwich) and latitude of the observation point, ω is the rotational velocity of the Earth, R is the radius of the Earth, x_p, y_p are the coordinates of the instantaneous pole with respect to the IERS reference pole in radians, and δ_{pole} represents the elasticity of the Earth (Torge, 2001). In the IAGBN: Absolute Observations Data Processing Standards, δ_{pole} is specified to $1.164 \cdot 10^8$ (for δg_{polar} in microgals). Predicted and final polar coordinates are available as bulletins from IERS (`http://www.iers.org`).

The upper panel of Fig. B.4 shows the polar motion correction throughout 2008. The correction reaches a significant magnitude when intervals covering months or years are studied. In 2008, the polar motion effect varied by nearly 7 µgal. On the other hand, polar motion has a slow changing effect on gravity. This is illustrated in lower panel of Fig. B.4. This figure shows the differential polar motion correction, i.e. how much the polar motion correction changes from one day to another. The magnitude of the gravity change within one day reaches at maximum 0.06 µgal in 2008. The modest daily changes justify polar motion corrections calculated as constants for gravity campaigns covering an interval of some days. In Fig B.2 and B.3, the correction is consequently not illustrated.

Reference height correction

Local gradients are used to transfer the processed gravity value to a datum height (reference height) defined in the g-software. The datum height is defined with respect to e.g. a benchmark, and does not coincide with a fixed point on the FG5. For typical gravity platforms, a datum height of 1.20 m coincides approximately with the mid point of the dropping chamber. By processing gravity for this height, the influence of any error in the locally observed gravity gradient is minimized. The error due to a gradient error is significantly larger when gravity is reduced to e.g. the height of the benchmark.

Figure B.5 shows the difference between gravity values processed with locally observed gradients and the normal gradient of -3.086 µgal cm^{-1} at 16 stations in Norway. The error calculated at Trysil stands out. The outlier results from two facts; (1) Compared to the other stations, the instrument height in Trysil is ∼2 cm shorter than the mean of the other stations; and (2) the difference between

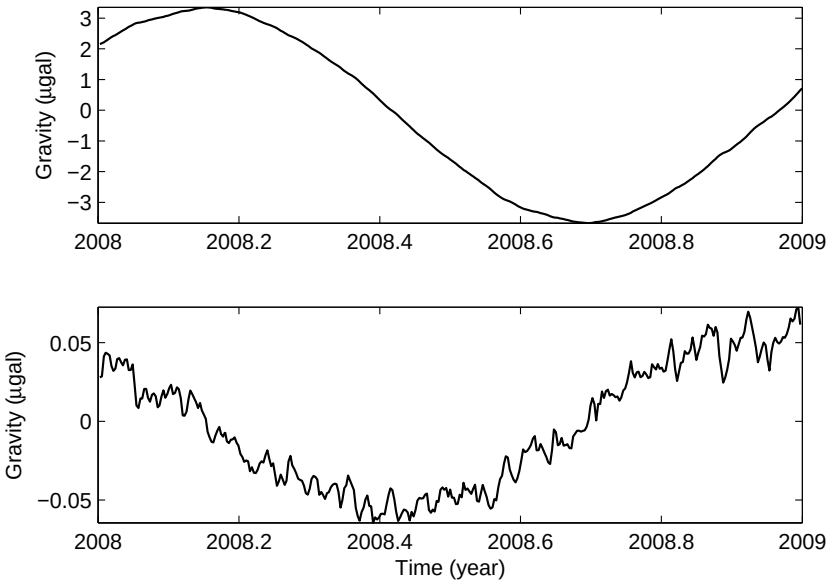

Figure B.4: Upper panel: The polar motion correction at Trysil in 2008. Lower panel: The differential polar motion correction, i.e. the change in the polar motion correction from one day to another. The time series were calculated by Eq. B.3. Daily coordinates of the instantaneous pole were provided by IERS.

the local gradient and the normal gradient is relatively large (-0.89 µgal cm^{-1}). This in combination makes the Trysil value extraordinary. It illustrates that the instrument height is significant when calculating the influence of a given gradient error.

Without the Trysil value, a gradient error of 1 µgal cm^{-1} results on average in a gravity error of ∼0.6 µgal for instrument heights of ∼12.5 cm.

Calibration of the rubidium oscillator

The rubidium oscillator is used to time and count the fringes generated by the interferometer. The frequency of the oscillator is close to 10 Mhz. A 1 mHz (millihertz) error causes a 0.2 µgal error (Francis and van Dam, 2006). Hence, the frequency of the oscillator should be routinely calibrated, e.g. by the phase difference method. The phase difference method is based on the observation of the time (ΔT) taken by the gravimeter's oscillator to shift by one complete cycle compared to a reference oscillator with frequency f_0. From ΔT, the frequency of

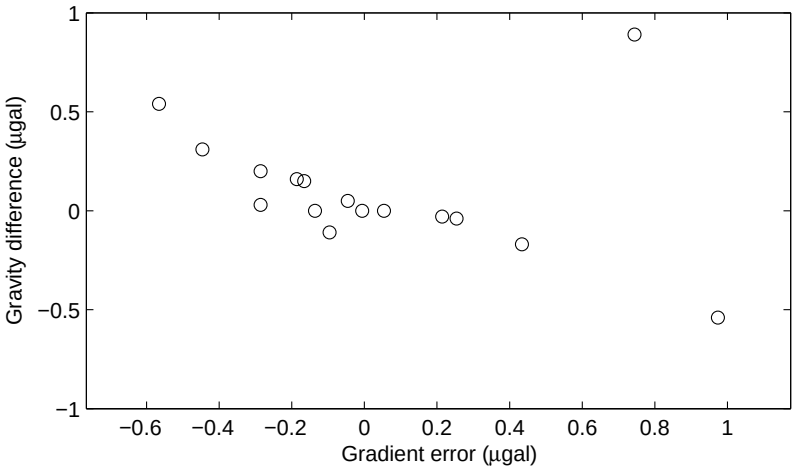

Figure B.5: The difference between gravity processed with local gravity gradients and normal gradients at 16 Norwegian stations. The outlying value in the upper right part of the figure is calculated for Trysil.

the gravimeter's oscillator (f_{FG5}) is calculated:

$$f_{FG5} = f_0 \pm \frac{1}{\Delta T} \tag{B.4}$$

The sign of the correction term ($1/\Delta T$) is positive if the oscillator of the gravimeter runs faster than the reference oscillator and negative if the oscillator of the gravimeter runs slower.

We used a GPS controlled rubidium frequency reference from Meinberg Funkuhr to calibrate the FG5-226. This reference oscillator uses the time from the GPS system to calibrate its own rubidium oscillator. By this, a 10 Mhz reference signal with an Allan variance of $\sigma^2(\tau) = 2 \cdot 10^{-12}$ over a time interval of $\tau = 100$ sec is generated (Meinberg, 2004). The Allan variance can be interpreted as the best guess of the drift from the nominal frequency over a time interval equal to τ. We adopt this value as the uncertainty of the reference frequency.

Equation (B.5) shows how errors due to f_0 and ΔT propagate through Eq. (B.4)

$$\sigma_f = \sqrt{\sigma^2(\tau) + \frac{\sigma^2_{\Delta T}}{\Delta T^4}} \tag{B.5}$$

Here, σ_f is the uncertainty of the calibrated frequency and $\sigma_{\Delta T}$ is the uncertainty of ΔT. For the oscillator of the FG5, ΔT was typically measured to approximately 200 sec. The uncertainty of this measurement was estimated to $\sigma_{\Delta T} = 2$ sec. This yields a calibrated frequency with an uncertainty $\sigma_f = 5 \cdot 10^{-5}$ Hz which

corresponds to a gravity change of 0.01 µgal, i.e. within the noise level of the FG5. Equation (B.5) also shows that the second term due to ΔT dominates (it is approximately 1000 times larger) compared to the term due to the uncertainty of the reference frequency. See e.g. Allan *et al.* (1997) for a nice description of the Allan variance and timekeeping in general.

Table B.1 shows calibrated frequencies of the FG5-226. The oscillator was changed in May 2007. According to the table, the frequency of the new oscillator was not stable during the first months of operation. With time it stabilized at a frequency of approximately 9999999.995 Hz. The table also shows the bias which arises if the nominal frequency of 10 MHz is used instead of the calibrated frequencies. For the FG5-226, the potential error reaches nearly 1 µgal in 2008 and 2009.

Table B.1: Calibrated frequencies of the rubidium oscillator of the FG5-226 absolute gravimeter and biases resulting from using a nominal frequency of 10 MHz instead of the calibrated frequency. The frequencies listed below the midline are for the new oscillator installed in May 2007.

Date of calibration	**Frequency (Hz)**	**Bias (µgal)**
2004	10000000.0018	-0.4
11 October 2005	10000000.0024	-0.5
6 October 2006	10000000.0024	-0.5
31 May 2007	10000000.0004	-0.1
8 July 2007	10000000.0011	-0.2
11 July 2007	10000000.0004	-0.1
15 July 2007	10000000.0015	-0.3
1 August 2007	9999999.9991	0.2
16 August 2007	9999999.9989	0.2
6 September 2007	9999999.9955	0.9
7 November 2007	9999999.9971	0.6
8 December 2007	9999999.9970	0.6
13 February 2008	9999999.9967	0.7
13 March 2008	9999999.9962	0.8
23 May 2008	9999999.9961	0.8
12 June 2008	9999999.9959	0.8
8 July 2008	9999999.9958	0.8
11 July 2008	9999999.9958	0.8
19 August 2008	9999999.9956	0.9
29 August 2008	9999999.9954	0.9
25 September 2008	9999999.9956	0.9
14 November 2008	9999999.9958	0.9
12 June 2009	9999999.9950	0.9

Appendix C

Amplitudes and phases for fast and easy OTL computations

The OTL effect in an arbitrary point at the surface of the Earth can be calculated by Eq. (2.20). This equation shows that the total load effect at a point is the sum of the effects from all individual ocean cells. Equation (2.20) involves substantial calculations and implementation of a complex set of formulas. For practical applications the effect is usually calculated from preprocessed site-specific amplitudes and phases representing the main OTL constituents. Such parameters are provided by e.g. the OTL service at `http://www.oso.chalmers.se/~loading/` and the g-software. The OTL effect (I_i) for an arbitrary epoch i can be calculated from the site specific amplitudes and phases by (McCarthy and Petit (2009)).

$$I_i = \sum_k^K f_k A_k \cos(\chi_{k,i} + u_k - \phi_k) \tag{C.1}$$

Here, A_k, ϕ_k are site-specific amplitude and Greenwich phase lag for tidal constituent k. The astronomical argument $\chi_{k,i}$ can be calculated by the ARG.f subroutine provided by the IERS. Formulas for nodal modulation phase u_k and amplitude f_k corrections are found in Schüler (2001). These corrections compensate for periodic variation in the orbital inclination of the Moon. For the solar constituents (S2, P1, and Ssa), the nodal modulation amplitude and phase corrections are set equal to one and zero, respectively. Equation C.1 was used in **paper A, B, C**, and **D** to calculate the effect of OTL.

The site specific amplitudes and phases in Eq. (C.1) can be calculated from Eq. (2.20) by expanding the ocean tide model convolved by the Green's function. For each grid point, the ocean tide model defines a set of amplitudes and phases of a finite number of tidal constituents. The total tidal height (H) for a cell with midpoint (λ_j, φ_j), is a superpositioning of K individual tidal constituents (H_k):

$$H(t_i, \lambda_j, \varphi_j) = \sum_k^K H_k(t_i, \lambda_j, \varphi_j) \tag{C.2}$$

The time dependent variation of the tidal height due to constituent k may be interpreted as a harmonic oscillation with constant amplitude $D_{k,j}$ and phase $\phi_{k,j}$.

$$H_k(t_i, \lambda_j, \varphi_j) = D_{k,j} \cos(\chi_{k,i} - \phi_{k,j})$$
$$= D_{k,j} \cos(\chi_{k,i}) \cos(\phi_{k,j}) + D_{k,j} \sin(\chi_{k,i}) \sin(\phi_{k,j}) \tag{C.3}$$

Notice the use of indices, i.e. k denotes constituent, i the epoch and j a cell in the ocean tide model.

Similarly to Eq. (2.20), the OTL effect of one particular tidal constituents at an observation point (λ, ϕ) is given by

$$I_k(t_i, \lambda, \varphi) = \rho \sum_j G(\alpha_j) H_k(t_i, \lambda_j, \varphi_j) dS_j. \tag{C.4}$$

Equation (C.4) is expanded by substituting Eq. (C.3) for the ocean tide model:

$$I_k(t_i, \lambda, \varphi) = \rho \sum_j G(\alpha_j) \left[D_{k,j} \cos(\chi_{k,i}) \cos(\phi_{k,j}) + D_{k,j} \sin(\chi_{k,i}) \sin(\phi_{k,j}) \right] dS_j$$
$$= \rho \cos(\chi_{k,i}) \sum_j G(\alpha_j) D_{k,j} \cos(\phi_{k,j}) dS_j + \rho \sin(\chi_{k,i}) \sum_j G(\alpha_j) D_{k,j} \sin(\phi_{k,j}) dS_j$$
$$= c_k \cos(\chi_{k,i}) + s_k \sin(\chi_{k,i}) \tag{C.5}$$

In Eq. (C.5) the time independent terms are gathered in the coefficients $c_k = \rho \sum_j G(\alpha_j) D_{k,j} \cos(\phi_{k,j}) dS_j$ and $s_k = \rho \sum_j G(\alpha_j) D_{k,j} \sin(\phi_{k,j}) dS_j$.

Alternatively, the OTL effect due to tidal constituent k can be written as a harmonic oscillation of constant amplitude (A_k) and phase (ϕ_k)

$$I_k(t_i, \lambda, \varphi) = A_k \cos(\chi_{k,i} - \phi_k)$$
$$= A_k \cos(\phi_k) \cos(\chi_{k,i}) + A_k \sin(\phi_k) \sin(\chi_{k,i}) \tag{C.6}$$

Equation (C.5) and (C.6) express the same signal and are consequently equal. This results in the following relations:

$$A_k \cos(\phi_k) = c_k \tag{C.7}$$
$$A_k \sin(\phi_k) = s_k \tag{C.8}$$

The amplitude and phase of OTL constituent k are calculated by Eq. (C.9) and (C.10) while c_k and s_k are calculated from the amplitudes and phases of the ocean tide model.

$$A_k = \sqrt{c_k^2 + s_k^2} \tag{C.9}$$
$$\phi_k = \arctan \frac{s_k}{c_k} \tag{C.10}$$

Equation (C.10) is ambiguous because the inverse tangent-function (arctan) returns ϕ_k on the interval $[-\pi/2, \pi/2]$. The phase angle of the OTL constituent is found by evaluating the sign fo the arguments s_k and c_k and choosing the right quadrant.

Appendix D

Estimating amplitudes and phases of OTL constituents

Least squares adjustment is a fundamental method to estimate parameters from observations. The method is based on the minimization of the sum of squared residuals. In this section it is determined how OTL constituents of known periods are estimated from a series of observations. OTL constituents are special signals because their frequencies are known and they are usually defined by the astronomical argument and the Greenwich phase lag. The method described below was used to estimate OTL constituents from GPS height time series in **paper C**.

The time series of observations is modeled as a superpositioning of K trigonometric functions with known frequencies ω_k, and unknown site specific amplitudes (A_k) and phases (ϕ'_k).

$$\tilde{z}_i = \sum_{k=1}^{K} A_k \cos(\omega_k t_i - \phi'_k) \tag{D.1}$$

In Eq. (D.1), $\tilde{z}_i$ is the modeled observation at epoch t_i.

For tidal analysis, the trigonometric functions represent tidal constituents. The tidal constituents may be interpreted as the signal of fictitious gravitational objects circulating the Earth with a known period. The astronomical angular argument $\chi_k(t_i)$ describes the angular position of the object in its orbit. Inserted into Eq. (D.1), it replaces the frequency, time and phase terms. The signal is tailored to an arbitrary location at the Earth by including a site specific phase angle ϕ_k.

$$\tilde{z}_i = \sum_{k=1}^{K} A_k \cos(\chi_k(t_i) - \phi_k) \tag{D.2}$$

A refined model is obtained by including nodal modulation phase u_k and amplitude f_k corrections. These quantities are known parameters and can be calculated from formulas found in e.g. Schüler (2001).

$$\tilde{z}_i = \sum_{k=1}^{K} A_k \cdot f_k \cos(\chi_k(t_i) + u_k - \phi_k) \tag{D.3}$$

To fit real observations, other parameters should also be included, i.e. parameters to model shifts, trends and offsets in the data. For simplicity, Eq. (D.3) is here

adopted as the final model used to estimate tidal constituents.

Equation (D.3) must be linearized before it is used in a least squares adjustment. Linearization is obtained by utilizing the well known trigonometric identity $\cos(\alpha - \beta) = \cos(\alpha)\cos(\beta) + \sin(\alpha)\sin(\beta)$.

$$\begin{aligned}\tilde{z}_i &= \sum_{k=1}^{K} [A_k\, k_k \cos(\chi_k(t_i) + u_k)\cos(\phi_k) + A_k\, f_k \sin(\chi_k(t_i) + u_k)\sin(\phi_k)] \\ &= \sum_{k=1}^{K} [a_k\, k_k \cos(\chi_k(t_i) + u_k) + b_k\, f_k \sin(\chi_k(t_i) + u_k)] \end{aligned} \tag{D.4}$$

In Eq. (D.4) $a_k = A_k \cos(\phi_k)$ and $b_k = A_k \sin(\phi_k)$ are the quantities estimated by least squares adjustment. From the estimated parameters a_k and b_k, the amplitude and phase of the tidal constituents are calculated by Eq. (D.5) and (D.6), respectively.

$$A_k = \sqrt{a_k^2 + b_k^2} \tag{D.5}$$

$$\tan \phi_k = \frac{b_k}{a_k} \tag{D.6}$$

The Rayleigh criterion is used as a guide to evaluate which tidal constituents are possible to estimate by least square adjustment from a time series of observations. From the Rayleigh criterion, the span of data records necessary to separate two signals with periods T_1 and T_2, must be (cf. Foreman (1977)).

$$\geq \frac{T_1 \cdot T_2}{|T_1 - T_2|}. \tag{D.7}$$

In Table D.1 the length of data records necessary to separate the eleven main tidal constituent (see Table D.2) is tabulated. However, there exist many more constituents, so called satellite constituents. The Rayleigh criterion illustrates the weak point of tidal analysis based on least squares adjustment. To distinguish the satellite constituents, time series covering up to 19 years are necessary before stable solutions are obtained (Agnew, 2007).

Table D.1: Interval (days) of data records necessary to separate the eleven main tidal periods according to the Rayleigh criterion.

	M2	**S2**	**N2**	**K2**	**K1**	**O1**	**P1**	**Q1**	**MF**	**MM**
S2	14.8									
N2	27.3	9.6								
K2	13.8	199.5	9.2							
K1	1.1	1.0	1.1	1.0						
O1	1.0	0.9	1.0	0.9	13.6					
P1	1.1	1.0	1.1	1.0	171.4	14.8				
Q1	1.0	0.9	1.0	0.9	9.1	27.5	9.6			
MF	0.5	0.5	0.5	0.5	1.1	1.2	1.1	1.2		
MM	0.5	0.5	0.5	0.5	1.0	1.1	1.0	1.2	27.1	
SSA	0.5	0.5	0.5	0.5	1.0	1.1	1.0	1.1	14.8	32.4

Table D.2: Periods of the eleven main tidal constituents (Torge, 2001)

M2	12.42 h
S2	12.00 h
N2	12.66 h
K2	11.97 h
K1	23.93 h
O1	25.82 h
P1	24.07 h
Q1	26.87 h
MF	13.66 d
MM	27.55 d
SSA	182.62 d

References

Abe, M., Takemoto, S., Fukuda, Y., Higashi, T., Imanishi, Y., Iwano, S., Ogasawara, S., Kobayashi, Y., Dwipa, S. and Kusuma, D. S. (2006). Hydrological effects on the superconducting gravimeter observation in Bandung. *Journal of Geodynamics*, **41**, pp. 288–295.

Agnew, D. C. (2005). *SPOTL: Some Programs for Ocean-Tide Loading*. Institute of Geophysics and Planetary Physics, Scripps Institution of Oceanography, University of California. Last visited 2009.07.01.
`http://www.igpp.ucsd.edu/~agnew/spotldocs.pdf`

Agnew, D. C. (2007). Earth Tides. In T. Herring and G. Schubert (editors), *Geodesy*, volume 3 of *Treatise on Geophysics*, pp. 163–195. Elsevier. ISBN 978-0-444-53460-6.

Allan, D. W., Ashby, N. and Clifford, C. H. (1997). Hewlett-Packard Application Note 1289: The Science of Timekeeping.

Allinson, C. R., Clarke, P. J., Edwards, S. J. and King, M. A. (2004). Stability of direct GPS estimates of ocean tide loading. *Geophysical Research Letters*, **31**. L15603.

Andersen, O., Egbert, G., Erofeeva, S. and Ray, R. (2006). Non-linear tides in shallow water regions from multi-mission satellite altimetry & the Andersen 06 Global Ocean Tide Model. In *AGU WPGM meeting, Beijing, China*.

Baker, T. F. and Bos, M. S. (2003). Validating Earth and ocean tide models using tidal gravity measurements. *Geophysical Journal International*, **152**, pp. 468–485.

Baker, T. F., Curtis, D. J. and Dodson, A. H. (1996). A New Test of Earth Tide Models in Central Europe. *Geophysical Research Letters*, **23**(24), pp. 3559–3562.

Boehm, J., Niell, A. E., Tregoning, P. and Schuh, H. (2006a). Global Mapping Function (GMF): A new empirical mapping function based on numerical weather model data. *Geophysical Research Letters*, **33**. L07304.

Boehm, J., Werl, B. and Schuh, H. (2006b). Troposphere mapping functions for GPS and very long baseline interferometry from European Centre for Medium-Range Weather Forecasts operational analysis data. *Journal of Geophysical Research*, **111**. B02406.

Bos, M., Baker, T., Røthing, K. and Plag, H.-P. (2002). Testing ocean tide models in the Nordic seas with tidal gravity observations. *Geophysical Journal International*, **150**, pp. 687–694.

Bower, D. R. and Courtier, N. (1998). Precipitation effects on gravity measurements at the Canadian Absolute Gravity Site. *Physics of the Earth and Planetary Interiors*, **106**, pp. 353–369.

Boy, J.-P., Gegout, P. and Hinderer, J. (2002). Reduction of surface gravity data from global atmospheric pressure loading. *Geophysical Journal International*, **149**, pp. 534–545.

Boy, J.-P. and Hinderer, J. (2006). Study of the seasonal gravity signal in superconducting gravimeter data. *Journal of Geodynamics*, **41**, pp. 227–233.

Boy, J.-P. and Lyard, F. (2008). High-frequency non-tidal ocean loading effects on surface gravity measurements. *Geophysical Journal International*, **175**, pp. 35–45.

Breili, K. and Pettersen, B. R. (2009). Effects of surface snow cover on gravimetric observations. *Journal of Geodynamics*, **48**, pp. 16–22.

Breili, K. and Rolstad, C. (2009). Ground-based gravimetry for measuring small spatial-scale mass changes on glaciers. *Annals of Glaciology*, **50**, pp. 141–147.

van Camp, M., Vanclooster, M., Crommen, O., Petermans, T., Verbeeck, K., Meurers, B., van Dam, T. and Dassargues, A. (2006). Hydrological investigations at the Membach station, Belgium, and application to correct long periodic gravity variations. *Journal of Geophysical Research*, **111**. B10403.

van Camp, M., Williams, S. D. P. and Francis, O. (2005). Uncertainty of absolute gravity measurements. *Journal of Geophysical Research*, **110**. B05406.

Cazenave, A. and Nerem, R. S. (2004). Present-day sea level change: Observations and causes. *Review of Geophysics*, **42**.

Crossley, D., Hinderer, J. and Boy, J. P. (2005). Time variation of the European gravity field from superconducting gravimeters. *Geophysical Journal International*, **161**, pp. 257–264.

Cutnell, J. D. and Johnson, K. W. (1997). *Physics*. John Wiley & Sons, Inc., 4 edition. ISBN 0-471-15519-5.

Dach, R., Hugentobler, U., Fridez, P. and Meindl, M. (2007). *Bernese GPS Software Version 5.0*. Astronomical Institute, University of Bern.

van Dam, T., Wahr, J., Milley, P. C. D., Shmakin, A. B., Blewitt, G., Lavallée, D. and Larson, K. M. (2001). Crustal displacements due to continental water loading. *Geophysical Research Letters*, **28**(4), pp. 651–654.

van Dam, T. M., Blewitt, G. and Heflin, M. B. (1994). Atmospheric pressure loading effects on Global Positioning System coordinate determinations. *Journal of Geophysical Research*, **99**(B12), pp. 23939–23950.

van Dam, T. M. and Wahr, J. M. (1987). Displacements of the Earth's Surface Due to Atmospheric Loading: Effects on Gravity and Baseline Measurements. *Journal of Geophysical Research*, **92**(B2), pp. 1281–1286.

Dehant, V., Defraigne, P. and Wahr, J. M. (1999). Tides for an Earth in a non-hydrostatic equilibrium. *Journal of Geophysical Research*, **104**(B1), pp. 1035–1058.

Dittfeld, H. J., Engen, B., Jentzsch, G., Madsen, F., Knudsen, P., Ramatschi, M., Røthing, K. and Schwintzer, P. (1997). Tidal gravity measurements within the MOTIVE project. *Marées Terrestres, Bulletin d'Informations*, **127**, pp. 9843–9850.

Dragert, H., James, T. S. and Lambert, A. (2000). Ocean Loading Corrections for Continuous GPS: A Case Study at the Canadian Coastal Site Holberg. *Geophysical Research Letters*, **27**, pp. 2045–2048.

Dziewonski, A. D. and Anderson, D. L. (1981). Preliminary reference earth model. *Physics of the Earth, Planetary Interiors*, **25**, pp. 297–356.

Eanes, R. J. and Shuler, A. (1999). An improved global ocean tide model from TOPEX/Poseidon altimetry: CSR4.0. In *EGS 24th General Assembly, Hague, Netherlands*.

Egbert, G. and Erofeeva, L. (2002). Efficient inverse modeling of barotropic ocean tides. *Journal of Atmospheric and Oceanic Technology*, **19**, pp. 183–204.

Engeset, R., Tveito, O. E., Alfnes, E., Mengistu, Z., Udnæs, H. C., Isaksen, K. and Førland, E. J. (2004). Snow map system for Norway. In *XXIII Nordic Hydrological Conference, 8-12 Aug. 2004. Tallinn, Estonia, NHP report 48(1)*, pp. 112–121.

Farrell, W. E. (1972). Deformation of the Earth by Surface Loads. *Reviews of Geophysics and Space Physics*, **10**, pp. 761–797.

Foreman, M. G. G. (1977). *Manual for tidal heights analysis and prediction.* Institute of Ocean Sciences, Pacific Marine Science Report 77-10.

Francis, O. and van Dam, T. (2006). Analysis of results of the International Comparison of Absolute Gravimeters in Walferdange (Luxembourg) of November 2003. *Cahiers du Centre Européen de Géodynamique et de Séismologie*, **26**, pp. 1–23.

Francis, O. and Mazzega, P. (1990). Global charts of ocean tide loading effects. *Journal of Geophysical Research*, **95**, pp. 11411–11424.

Francis, O. and Melchior, P. (1996). Tidal loading in south western Europa: a test area. *Geophysical Research Letters*, **23**(17), pp. 2251–2254.

Fukuda, Y., Hiraoka, Y. and Doi, K. (2007). An Experiment of Precise Gravity Measurements on Ice Sheet, Antarctica. In P. Tregoning and C. Rizos (editors), *Dynamic Planet. Monitoring and Understanding a Dynamic Planet with Geodetic and Oceanographic Tools*, volume 130 of *International Association of Geodesy Symposia*, pp. 88–93.

Fukuda, Y., Shibuya, K., Doi, K. and Aoki, S. (2003). A Challenge to the Detection of Regional to Local Scale Ice Sheet Movements in Antarctica by the Combination of In-situ Gravity Measurements and Gravity Satellite Data. In I. N. Tziavos (editor), *Gravity and Geoid 2002, 3rd Meeting of the International Gravity and Geoid Commission (IGGC)*, pp. 243–248.

Goad, C. C. (1980). Gravimetric Tidal Loading Computed From Integrated Green's Functions. *Journal of Geophysical Research*, **85**(B5), pp. 2679–2683.

Haagmans, R., Floberghagen, R., Pieper, B. and Drinkwater, M. (2006). *GOCE ESA's gravity mission.* ESA Publications Division. Edited by Honora, R., Rast, M. and Battrick, B. ISBN 92-9092-663-5.

Harnisch, G. and Harnisch, M. (2006). Hydrological influences in long gravimetric data series. *Journal of Geodynamics*, **41**, pp. 276–287.

Hazel, R. (1989). A Contribution to Precision Microgravity Data Analysis Using Lacoste and Romberg Gravity Meters. *Geophysical Journal International*, **97**(2), pp. 311–322.

Heiskanen, W. A. and Moritz, H. (1967). *Physical Geodesy.* Reprint University of Graz, Austria, reprint edition.

Hinderer, J., Andersen, O., Lemoine, F., Crossley, D. and Boy, J. P. (2006). Seasonal changes in the European gravity field from GRACE: A comparison with superconducting gravimeters and hydrology model predictions. *Journal of Geodynamics*, **41**, pp. 59–68.

Hinderer, J., Crossley, D. and Warburton, R. J. (2007). Gravimetric Methods - Superconducting Gravity Meters. In T. Herring and G. Schubert (editors), *Geodesy*, volume 3 of *Treatise on Geophysics*, pp. 65–122. Elsevier. ISBN 978-0-444-53460-6.

Hoffmann-Wellenhof, B., Lichtenegger, H. and Collins, J. (2001). *GPS Theory and Practice.* SpringerWienNewYork, 5 edition. ISBN 3-211-83534-2.

Hofmann-Wellenhof, B. and Moritz, H. (2005). *Physical Geodesy.* SpringerWienNewYork, 1 edition. ISBN 3-211-23584-1.

Hokkanen, T., Korhonen, K. and Virtanen, H. (2006). Hydrogeological effects on superconducting gravimeter measurements at Metsähovi in Finland. *Journal of Environmental and Engineering Geophysics*, **11**(4), pp. 261–267.

Humphreys, T. E., Kelley, M. C., Huber, N. and Kintner Jr., P. M. (2005). The semidiurnal variation in GPS-derived zenith neutral delay. *Geophysical Research Letters*, **32**. L24801.

Imanishi, Y., Kokubo, K. and Tatehata, H. (2006). Effect of underground water on gravity observation at Matsushiro, Japan. *Journal of Geodynamics*, **41**, pp. 221–226.

Jentzsch, G. (1997). Earth Tides and Ocean Tidal Loading. In H. Wilhelm, W. Zürn and H. G. Wenzel (editors), *Tidal Phenomena*, volume 66 of *Lecture Notes in Earth Sciences*, pp. 145–171. Springer Verlag Berlin Heidelberg.

Jentzsch, G., Knudsen, P. and Ramatschi, M. (2000). Ocean Tidal Loading Affecting Precise Geodetic Observations on Greenland: Error Account and Surface Deformations by Tidal Gravity Measurements. *Physics and Chemistry of the Earth A*, **25**(4), pp. 401–407.

Johannessen, J. A., Balmino, G., Le Provost, C., Rummel, R., Sabadini, R., Sünkel, H., Tscherning, C. C., Visser, P., Woodworth, P., Hughes, C. W., Legrand, P., Sneeuw, N., Perosanz, F., Aguirre-Martinez, M., Rebhan, H. and Drinkwater, M. R. (2003). The European gravity field and steady-state ocean circulation explorer satellite mission: Its impact on geophysics. *Surveys in Geophysics*, **24**, pp. 339–386.

Johansson, J. M., Davis, J. L., Scherneck, H. G., Milne, G. A., Vermeer, M., Mitrovica, J. X., Bennett, R. A., Jonsson, B., Elgered, G., Elósegui, P., Koivula, H., Poutanen, M., Rönnäng, B. O. and Shapiro, I. I. (2002). Continuos GPS measurements of postglacial adjustment in Fennoscandia 1. Geodetic results. *Journal of Geophysical Research*, **107**(B8). 2157, doi:10.1029/2001JB000400.

Khan, S. A. (2005). *Surface deformations analyzed using GPS time series*. Ph.D. thesis, Danish National Space Center.

Khan, S. A. and Scherneck, H.-G. (2003). The M_2 ocean tide loading wave in Alaska: Vertical and horizontal displacements, modelled and observed. *Journal of Geodesy*, **77**, pp. 117–127.

Khan, S. A., Wahr, J., Leuliette, E., van Dam, T., Larson, K. M. and Francis, O. (2008). Geodetic measurements of postglacial adjustment in Greenland. *Journal of Geophysical Research*, **113**. B02402.

Khan, S. A., Wahr, J., Stearns, L. A., Hamilton, G. S., van Dam, T., Larson, K. M. and Francis, O. (2007). Elastic uplift in southeast Greenland due to rapid ice mass loss. *Geophysical Research Letters*, **34**. L21701.

King, M. A., Penna, N. T. and Clarke, P. J. (2005). Validation of ocean tide models around Antarctica using onshore GPS and gravity data. *Journal of Geophysical Research*, **110**. B08401.

Kjørsvik, N. S., Øvstedal, O. and Gjevestad, J. G. O. (2008). Kinematic Precise Point Positioning During Marginal Satellite Availability. In *Observing our Changing Earth. Proceedings of the 2007 IAG General Assembly, Perugia, Italy, July 2-13, 2007*, volume 133 of *International Association of Geodesy Symposia*, pp. 691–699.

Klingele, E. and Kahle, H. G. (1977). Gravity profiling as a technique for determining the thickness of glacier ice. *Pure and Applied Geophysics*, **115**(4), pp. 989–998.

Kouba, J. (2009). *A guide to using International GNSS Service (IGS) products*. Technical report, IGS Central Bureau. Last visited 2010.01.29. `http://www.igs.org/components/usage.html`

Lambeck, K. (1988). *Geophysical Geodesy. The Slow Deformations of the Earth*. Oxford University Press, New York, 1 edition. ISBN 0-19-854438-3.

Lambeck, K., Smither, C. and Johnston, P. (1998). Sea-level change, glaciel rebound and mantle viscosity for northern Europe. *Geophysical Journal International*, **134**, pp. 102–144.

Lambert, A., Courtier, N. and James, T. S. (2006). Long-term monitoring by absolute gravimetry: Tides to postglacial rebound. *Journal of Geodynamics*, **41**, pp. 307–317.

Larson, K. and van Dam, T. (2000). Measuring Postglacial Rebound with GPS and Absolute Gravity. *Geophysical Research Letters*, **27**(23), pp. 3925–3928.

Le Provost, C., Lyard, F., Molines, J. M., Genco, M. L. and Rabilloud, F. (1998). A hydrodynamic ocean tide model improved by assimilating a satellite altimeter-derived data set. *Journal of Geophysical Reserach*, **103(C3)**, pp. 5513–5529.

Leick, A. (2004). *GPS satellite surveying*. John Wiley & Sons, Inc., 3 edition. ISBN 0-471-05930-7.

Letellier, T. (2004). *Etude des ondes de mare sur les plateux continentaux*. Ph.D. thesis, Université de Toulouse III, France.

Llubes, M., Florsch, N., Hinderer, J., Longuevergne, L. and Amalvict, M. (2004). Local hydrology, the Global Geodynamics Project and CHAMP/GRACE perspective: some case studies. *Journal of Geodynamics*, **38**, pp. 355–374.

Luthcke, S. B., Arendt, A. A., Rowlands, D. D., McCarthy, J. J. and Larsen, C. F. (2008). Recent glacier mass changes in the Gulf of Alaska region from GRACE mascon solutions. *Journal of Glaciology*, **54(188)**, pp. 767–777.

Lyard, F., Lefevre, F., Letellier, T. and Francis, O. (2006). Modelling the global ocean tides: modern insights from FES2004. *Ocean Dynamics*, **56**, pp. 394–451.

Lysaker, D. I., Breili, K. and Pettersen, B. R. (2008). The gravitational effect of ocean tide loading at high latitude coastal stations in Norway. *Journal of Geodesy*, **82**, pp. 569–583.

Matsumoto, K., Takanezawa, T. and Ooe, M. (2000). Ocean Tide Models Developed by Assimilating TOPEX/POSEIDON Altimeter Data into Hydrodynamical Model: A Global Model and a Regional Model around Japan. *Journal of Oceanography*, **56**, pp. 567–581.

Matsumoto, K., Takanezawa, T. and Ooe, M. (2006). NAO.99b tidal prediction system. Last visited 2009.07.01.
`http://www.miz.nao.ac.jp/staffs/nao99/index_En.html`

McCarthy, D. D. and Petit, G. (2003). *IERS Technical Note 32, IERS Conventions 2003*. Technical report, International Earth Rotation and Reference Systems Service (IERS).

McCarthy, D. D. and Petit, G. (2009). *IERS Technical Note 32, IERS Conventions 2003 - Update*. Technical report, International Earth Rotation and Reference Systems Service (IERS). Last visited 2009.09.17. `http://tai.bipm.org/iers/convupdt/convupdt.html`

Meinberg, W. (2004). *Technische Daten Inbetriebnahme GPS-receiver Rubidium Portable*. Meinberg Funkuhren GmbH & Co., Lange Wand 9, D - 31812 Bad Pyrmont.

Melachroinos, S. A., Biancale, R., Llubes, M., Perosanz, F., Lyard, F., Vergnolle, M., Bouin, M. N., Masson, F., Nicolas, J., Morel, L. and Durand, S. (2007). Ocean tide loading (OTL) displacements from global and local grids: comparisons to GPS estimates over the shelf of Brittany, France. *Journal of Geodesy*, **82**, pp. 357–371.

Meurers, B., van Camp, M. and Petermans, T. (2007). Correcting superconducting gravity time-series using rainfall modelling at the Vienna and Membach stations and application to Earth tide analysis. *Journal of Geodesy*, **81**(11), pp. 703–712.

Micro-g Solutions Inc. (2005). *g Users Manual v5.0*. Erie, Colorado, USA.

Milne, G. A., Davis, J. L., Mitrovica, J. X., Scherneck, H. G., Johansson, J. M., Vermeer, M. and Koivula, H. (2001). Space-Geodetic Constraints on Glacial Isostatic Adjustment in Fennoscandia. *Science*, **291**, pp. 2381–2385.

Misra, P. and Enge, P. (2006). *Global Positioning System: Signals, Measurements, and Performance*. Ganga-Jamuna Press, 2 edition.

Montgomery, D. C., Peck, E. A. and Vining, G. G. (2001). *Introduction to Linear Regression Analysis*. John Wiley and Sons, Inc, 3 edition.

Morelli, C., Gantar, C., Honkasalo, T., McConnell, R. K., Tanner, J. G., Szabo, B., Uotila, U. and Whalen, C. T. (1971). The International Gravity Standardization NET 1971 (I.G.S.N. 71). *International Union of Geodesy and Geophysics (International Association of Geodesy), Publication Special*, **4**.

Murray, T. (2006). Greenland's ice on the scales. *Nature*, **443**, pp. 277–278.

NASA (1976). U.S. Standard Atmosphere (NASA-TM-X-74335). National Aeronautics and Space Administration, U.S. Government Printing Office, Washington, D.C.

Neumeyer, J., Barthelmes, F., Dierks, O., Flechtner, F., Harnisch, M., Harnisch, G., Hinderer, J., Imanishi, Y., Kroner, M., Meurers, B., Petrovic, S., Reigber,

C., Schmidt, R., Schwintzer, P., Sun, H. P. and Virtanen, H. (2006). Combination of temporal gravity variations resulting from superconducting gravimeter (SG) recordings, GRACE satellite observations and global hydrology models. *Journal of Geodesy*, **79**, pp. 573–585.

Neumeyer, J., Hagedoorn, J., Leitloff, J. and Schmidt, T. (2004). Gravity reduction with three-dimensional atmospheric pressure data for precise ground gravity measurements. *Journal of Geodynamics*, **38**, pp. 437–450.

Neumeyer, J., del Pino, J., Dierks, O., Sun, H. P. and Pflug, H. (2005). Improvement of ocean loading correction on gravity data with additional tide gauge measurements. *Journal of Geodynamics*, **40**, pp. 104–111.

Niebauer, T. M., Sasagawa, G. S., Faller, J. E., Hilt, R. and Klopping, F. (1995). A new generation of absolute gravimeters. *Metrologia*, **32**, pp. 159–180.

Niell, A. E. (1996). Global mapping functions for the atmosphere delay at radio wavelengths. *Journal of Geophysical Research*, **101**(B2), pp. 3227–3246.

Pagiatakis, S. D. (1990). The response of a realistic earth to ocean tide loading. *Geophysical Journal International*, **103**, pp. 541–560.

Penna, N. T., Bos, M. S., Baker, T. F. and Scherneck, H. G. (2008). Assessing the accuracy of predicted ocean tide loading displacement values. *Journal of Geodesy*, **82**(12), pp. 893–907.

Petrov, L. and Ma, C. (2003). Study of harmonic site position variations determined by very long baseline interferometry. *Journal of Geophysical Research*, **108**(B4). 2190, doi:10.1029/2002JB001801.

Pettersen, B. R., Bilker-Koivula, M., Breili, K., Engfeldt, A., Falk, R., Gitlein, O., Gjevestad, J. G. O., Hoppe, W., Lysaker, D. I., Mäkinen, J., Omang, O. C. D., Reinhold, A. and Timmen, L. (2009). An accuracy assessment of absolute gravimetric observations in Fennoscandia. *Submitted Nordic Journal of Surveying and Real Estate Recearch*.

Pugh, D. (2004). *Changing Sea Levels*. Cambridge University Press. ISBN 0-521-53218-3.

Ray, R. D. (1999). *NASA/TM-209478: A Global Ocean Tide Model From TOPEX/POSEIDON Altimetry: GOT99.2*. Technical report, NASA.

Reigber, C., Schwintzer, P. and Lühr, H. (1999). The CHAMP geopotential mission. *Bollettino di Geofisica Teorica e Applicata*, **40**, pp. 285–289.

Roland, E. (1998). Absolutt tyngdemåling i Fennoskandia og Svalbard. Internal project report, Geodetic Institute, Norwegian Mapping Authority.

Rolstad, C., Haug, T. and Denby, B. (2009). Spatially integrated geodetic glacier mass balance and its uncertainty based on geostatistical analysis: application to the western Svartisen ice cap, Norway. *Journal of Glaciology*, **55**(192), pp. 666–680.

Rottman, K. (1995). *Matematisk Formelsamling, norsk utgave*. Bracan Forlag, 2 edition. ISBN 82-7822-005-0.

Saastamoinen, J. (1973). Contribution to the theory of atmospheric refraction. *Bulletin Géodésique*, **107**, pp. 13–34.

Sato, T., Boy, J. P., Tamura, Y., Matsumoto, K., Asari, K., Plag, H. P. and Francis, O. (2006a). Gravity tide and seasonal gravity variation at Ny-Ålesund, Svalbard in Arctic. *Journal of Geodynamics*, **41**, pp. 234–241.

Sato, T., Fukuda, Y., Aoyama, Y., McQueen, H., Shibuya, K., Tamura, Y., Asari, K. and Ooe, M. (2001). On the observed annual gravity variation and the effect of sea surface height variations. *Physics of the Earth and Planetary Interiors*, **123**, pp. 45–63.

Sato, T., Okuno, J., Hinderer, J., MacMillan, D. S., Plag, H. P., Francis, O., Falk, R. and Fukuda, Y. (2006b). A geophysical interpretation of the secular displacement and gravity rates observed at Ny-Ålesund, Svalbard in the Arctic - effects of post-glacial rebound and present-day ice melting. *Geophysical Journal International*, **165**, pp. 729–743.

Savcenko, R. and Bosch, W. (2008). *EOT08a - empirical ocean tide model from multi-mission satellite altimetry*. Deutsches Geodätisches Forschungsinstitut (DGFI), München, 2. Report No. 81.

Scargle, D. J. (1982). Studies in astronomical time series analysis. II. Statistical aspects of spectral analysis of unevenly spaced data. *The Astrophysical Journal*, **263**, pp. 835–853.

Scherneck, H. G. (1991). A parameterized solid earth tide model and ocean tide loading effects for global geodetic baseline measurements. *Geophysical Journal International*, **106**, pp. 677–694.

Scherneck, H. G. and Bos, M. (2009). The ocean tide loading provider. Last visited 2009.07.01.
`http://www.oso.chalmers.se/~loading`

Schüler, T. (2001). *On Ground-Based GPS Tropospheric Delay Estimation*. Ph.D. thesis, University of Armed Forces, München, Germany.

Schwiderski, E. (1980). On charting global ocean tides. *Reviews of Geophysics and Space Physics*, **18**(1), pp. 243–268.

SCINTREX Limited (2006). *CG-5, Scintrex Autograv System. Operation Manual*. Concord, Ontario, Canada.

Seeber, G. (2003). *Satellite Geodesy, 2nd completely revised and extended edition*. Walter de Gruyter, 2 edition. ISBN 3-11-017549-5.

Sovers, O. J. (1994). Vertical ocean loading amplitudes from VLBI measurements. *Geophysical Research Letters*, **21**(5), pp. 357–360.

Steffen, H., Gitlein, O., Denker, H., Müller, J. and Timmen, L. (2009). Present rate of uplift in Fennoscandia from GRACE and absolute gravimetry. *Tectonophysics*, **474**, pp. 69–77.

Tamura, Y. (1987). A Harmonic Development of the Tide-Generating Potential. *Marées Terrestres Bulletin D'Informations*, **99**, pp. 6813–6855.

Tapley, B. D., Bettadpur, S., Watkins, M. and Reigber, C. (2004). The Gravity Recovery and Climate Experiment: Mission Overview and Early Results. *Geophysical Research Letters*, **31**. L09607, doi:10.1029/2004GL019920.

Teferle, F. N., Bingley, R. M., Orliac, E. J., Williams, S. D. P., Woodworth, P. L., McLaughlin, D., Baker, T. F., Shennan, I., Milne, G. A., Bradley, S. L. and Hansen, D. N. (2009). Crustal motions in Great Britain: evidence from continuous GPS, absolute gravity and Holocene sea level data. *Geophysical Journal International*, **178**, pp. 23–46.

Terratec (2007). *TERRAPOS User's Manual. Version 1.2*.

Timofeev, V. Y., van Ruymbeke, M., Woppelmann, G., Everaerts, M., Zapreeva, E., Gornov, P. Y. and Ducarme, B. (2006). Tidal gravity observations in Eastern Siberia and along the Atlantic coast of France. *Journal of Geodynamics*, **41**, pp. 30–38.

Torge, W. (2001). *Geodesy*. Walter de Gruyter, 3 edition. ISBN 3-11-017072-8.

Turcotte, D. L. and Schubert, G. (2002). *Geodynamics*. Cambridge University Press, 2 edition. ISBN 0-521-66624-4.

Urschl, C., Dach, R., Hugentobler, U., Schaer, S. and Beutler, G. (2005). Validating ocean tide loading models using GPS. *Journal of Geodesy*, **78**, pp. 616–625.

Velicogna, I. and Wahr, J. (2006a). Acceleration of Greenland ice mass loss in spring 2004. *Nature*, **443**(7109), pp. 329–331.

Velicogna, I. and Wahr, J. (2006b). Measurement of Time-Variable Gravity Show Mass Loss in Antarctica. *Science*, **311**(5768), pp. 1754–1756.

Vestøl, O. (2006). Determination of postglacial land uplift in Fennoscandia from leveling, tide-gauges and continuous GPS stations using least squares collocation. *Journal of Geodesy*, **80**, pp. 248–258.

Vey, S., Calais, E., Llubes, M., Florsch, N., Woppelmann, G., Hinderer, J., Amalvict, M., Lalancette, M. F., Simon, B., Duquenne, F. and Haase, J. S. (2002). GPS measurements of ocean loading and its impact on zenith tropospheric delay estimates: a case study in Brittany, France. *Journal of Geodesy*, **76**, pp. 419–427.

Virtanen, H. (2006). *Studies of Earth dynamics with the superconducting gravimeter*. Ph.D. thesis, University of Helsinki, Finland.

Wahr, J., DaZhong, H. and Trupin, A. (1995). Predictions of Vertical Uplift Caused by Changing Polar Ice Volumes on a Viscoelastic Earth. *Geophysical Research Letters*, **22**(8), pp. 977–980.

Wang, R. (1997). Tidal response of the solid Earth. In H. Wilhelm, W. Zürn and H. G. Wenzel (editors), *Tidal Phenomena*, volume 66 of *Lecture Notes in Earth Sciences*, pp. 27–56. Springer Verlag Berlin Heidelberg.

Weisstein, E. (2007). Wolfram MathWorld. Last visited 2009.07.01.
`http://mathworld.wolfram.com/`

Wenzel, H. G. (1997). Tide-Generating Potential for the Earth. In H. Wilhelm, W. Zürn and H. G. Wenzel (editors), *Tidal Phenomena*, volume 66 of *Lecture Notes in Earth Sciences*, pp. 9–25. Springer Verlag Berlin Heidelberg.

Wessel, P. and Smith, W. H. F. (1996). A Global Self-consistent, Hierarchical, High-resolution Shoreline Database. *Journal of Geophysical Research*, **101**(B4), pp. 8741–8743. Last visited 2009.07.01.
`http://www.ngdc.noaa.gov/mgg/shorelines/data/gshhs/`

Wikipedia (2009). Last visited 2009.09.11.
`http://no.wikipedia.org/wiki/Langnestunnelen`

Wright, A., Wadham, J., Siegert, M., Luckman, A. and Kohler, J. (2005). Modelling the impact of superimposed ice on the mass balance of an Arctic glacier under scenarios of future climate change. *Annals of Glaciology*, **42**, pp. 277–283.

Yuan, L. G., Ding, X. L., Zhong, P., Chen, W. and Huang, D. F. (2008). Estimates of ocean tide loading displacements and its impact on position time series in Hong Kong using a dense continuous GPS network. *Journal of Geodesy*. doi:10.1007/s00190-009-0319-0.